DISSERTAÇÃO DE MESTRADO ACADÊMICO

Integration and Design of a Reconfigurable Reflectarray antenna with an RF LoRa-based system for IoT multi-protocol applications

Daniel Carvalho de Sousa

Brasília, dezembro de 2022

UNIVERSIDADE DE BRASÍLIA

FACULDADE DE TECNOLOGIA

UNIVERSIDADE DE BRASÍLIA
Faculdade de Tecnologia

DISSERTAÇÃO DE MESTRADO ACADÊMICO

Integration and Design of a Reconfigurable Reflectarray antenna with an RF LoRa-based system for IoT multi-protocol applications

Daniel Carvalho de Sousa

Dissertação de Mestrado Acadêmico submetida ao Departamento de Engenharia Elétrica como requisito parcial para obtenção do grau de Mestre em Engenharia Elétrica

Banca Examinadora

Prof. Sébastien R.M.J. Rondineau, Ph.D, FT/UnB _____
Orientador

Prof. Daniel Costa Araujo, Ph.D, FT/UnB _____
Examinador Interno

Dr. Bayanmunkh Enkhbayar _____
Examinador externo

Prof. Daniel O. de Carvalho, Ph.D, FT/UnB _____
Examinador interno (Suplente)

FICHA CATALOGRÁFICA

SOUSA, DANIEL CARVALHO
Integration and Design of a Reconfigurable Reflectarray antenna with an RF LoRa-based systemfor IoT multi-protocol applications [Distrito Federal] 2022.
xvi, 84 p., 210 x 297 mm (ENE/FT/UnB, Mestre, Engenharia Elétrica, 2022).
Dissertação de Mestrado Acadêmico - Universidade de Brasília, Faculdade de Tecnologia.
Departamento de Engenharia Elétrica

1. Reflectarray	2. Beamforming
3. IoT	4. Lora
I. ENE/FT/UnB	II. Título (série)

BIBLIOGRAPHIC REFERENCES

SOUSA, D.C. (2022). *Integration and Design of a Reconfigurable Reflectarray antenna with an RF LoRa-based systemfor IoT multi-protocol applications*. Dissertação de Mestrado Acadêmico, Publicação PPGEE.DM-801/22, Departamento de Engenharia Elétrica, Universidade de Brasília, Brasília, DF, 84 p.

CESSÃO DE DIREITOS

AUTOR: Daniel Carvalho de Sousa
TÍTULO: Integration and Design of a Reconfigurable Reflectarray antenna with an RF LoRa-based systemfor IoT multi-protocol applications.
GRAU: Mestre em Engenharia Elétrica ANO: 2022

Daniel Carvalho de Sousa
Depto. de Engenharia Elétrica (ENE) - FT
Universidade de Brasília (UnB)
Campus Darcy Ribeiro
CEP 70919-970 - Brasília - DF - Brasil

DEDICATÓRIA

Primeiramente, dedico este trabalho a Deus, de onde vêm a minha motivação e esperança, que por meio da fé, me fortifica e me traz não só o propósito para a vida, mas também trás a paz em momentos de angústia. À minha querida família, que tanto me ajudou em todos os momentos dessa jornada, dedico o resultado do esforço realizado ao longo deste percurso. Também dedico esse trabalho aos engenheiros e companheiros de curso, tanto os que me ajudaram nessa caminhada, quanto os que ainda haverão de ler essa dissertação.

RESUMO

O presente trabalho consiste no desenvolvimento de uma antena do tipo Reflectarray ativa reconfigurável. O elemento ativo utilizado nessa antena é o diodo PIN, utilizado para o controle da distribuição de fase do elemento irradiante, que consiste de uma estrutura planar retangular do tipo microfita.

A antena foi desenvolvida para aplicações de comunicação via satélite operando na banda Ku, devido à sua versatilidade, uma vez que permite o apontamento digital, otimização e conformação de feixe, por meio de diversas técnicas de *beamforming* (formação de feixe). A técnica de otimização convexa é discutida e implementada para o ajuste de fase e otimização de lóbulos secundários. Essa antena pode ser utilizada tanto em satélites de baixa órbita, quanto em estações rádio-base.

Devido às características da topologia apresentada, se faz necessário não só o desenvolvimento de circuitos de controle microcontrolados, mas também o projeto das fontes de alimentação eficientes. Nesse sentido, uma nova abordagem para o circuito de controle é apresentada, que foi validada por meio de um protótipo funcional.

Fazendo-se uso da possibilidade de transmissão de dados em longas distâncias, por meio dos satélites de baixa órbita, um sistema baseado no protocolo de transmissão LoRaWAN. Esse sistema foi projetado visando maximizar o alcance da comunicação entre dois dispositivos LoRa.

ABSTRACT

The present work consists of the development of an active reconfigurable Reflectarray antenna. The active element used in the antenna is the PIN diode, which controls the phase distribution of the antenna. The radiating element is based on a flat rectangular microstrip structure.

This antenna was developed for satellite communications operating in the Ku band. Its versatility allows for digital beam-scanning, optimization and beamforming, through various techniques, such as the convex optimization technique, which is applied for phase-optimization and sidelobe minimization. This antenna can be used either in low-orbit satellites or base stations.

Due to this topology characteristics, the design of the efficient cell control circuit, and efficient power supply are desirable. In this sense, a new approach to the control circuit is shown, which was validated through a functional prototype.

Due to the possibility of transmitting data over long distances, through low-orbit satellites, a system based on the LoRaWAN protocol was designed. This system aims to maximize the communication range between two LoRa devices.

SUMMARY

LIST OF FIGURES

LIST OF TABLES

LIST OF SYMBOLS

Latin Symbols

$\mathbf{E}$	Electric Field	[V/m]
$\mathbf{H}$	Magnetic Field	[A/m]
F_θ	Theta-component of the Spherical Radiation Vector	[A.m]
F_ϕ	Phi-component of the Spherical Radiation Vector	[A.m]
$\mathcal{P}$	Poynting vector	$[W/m^2]$
$D(\theta, \phi)$	Directivity gain	
P_{rad}	Radiated power	[W]
P_{in}	Input power	[W]
$\vec{r}_{mn}$	Element position vector	[m]
$\vec{r}_f$	Feed antenna position vector	[m]
$\hat{u}_b$	unitary beam direction	
$g_n(\theta, \phi)$	Normalized gain	
$\boldsymbol{g}(\theta, \phi)$	Fourier transform of the Magnetic Aperture Field	
$\boldsymbol{f}(\theta, \phi)$	Fourier transform of the Electric Aperture Field	
$\boldsymbol{F}(\theta, \phi)$	Radiation Vector (Electric Component)	[A.m]
$\boldsymbol{F}_m(\theta, \phi)$	Radiation Vector (Magnetic Component)	[V.m]
G	Green's function	
G_h	Horn Antenna Gain	
U	Radiation intensity	[W/sr]
e_{cd}	Conduction and dielectric efficiency	
$\mathbf{J_{ms}}$	Aperture magnetic current density	$[V/m^2]$
$\mathbf{E}_a$	Equivalent aperture electric field	[V/m]
$\mathbf{H}_a$	Equivalent aperture magnetic field	[A/m]
J_s	Electrical surface current	$[A/m^2]$
F_0	Fresnel diffraction integral of first type	
F_1	Fresnel diffraction integral of the second type	
i_n	Current excitation on the n-th element	[A]
$A_{uc}(\theta, \phi)$	Unit-cell radiation pattern	
F_s	Field Sampled by the Reflectarray	[A.m]
F_F	Radiation Pattern generated by the feed antenna	
R_i	Phase delay on the i-th element	[rad]
x_m	x-position of the m-th element of the array	[m]
y_n	y-position of the n-th element of the array	[m]
x_{feed}	x-coordinate of the feed antenna	[m]
y_{feed}	y-coordinate of the feed antenna	[m]
$C(V)$	Total varactor capacitance	[F]
C_0	Varactor diode capacitance at 0V bias	[F]
C_j	Junction Capacitance	[F]
Φ_D	Diode contact potential	[V]
C_{case}	Case/Package capacitance	[F]
L_{lead}	Lead inductance	[H]
R_S	Diode series resistance	[Ω]

G_V	Junction Conductance	[S]
L	PIN Diode series inductance	[H]
C_T	PIN Diode parallel capacitance	[F]
R_P	Diode parallel resistance	[Ω]
$Z(j\omega)$	Impedance, frequency-dependent	[Ω]
$\mathbf{I}$	Electric Current	[A]
J_y	Surface current density at y-direction	[A/m]
A_y	Potential vector at y-direction	[T.m]
N	Number of elements of the array in each direction	
$f_0(x)$	Objective function	
$f_i(x)$	Constraints function	
X_{max}	maximum limit of the search region	
X_{min}	minimum limit of the search region	
$\boldsymbol{E_r}$	Reflected Electric field	[V/m]
$\boldsymbol{E_i}$	Incident Electric field	[V/m]

Greek Symbols

η	Medium intrinsic wave impedance	[Ω]
η_{ap}	Aperture efficiency	
η_{ill}	Illumination efficiency	
η_s	Spillover efficiency	
η_p	phase error efficiency	
η_r	reflection loss efficiency	
∇	Differential operator	$[m^{-1}]$
∇^2	Laplacian operator	$[m^{-2}]$
Γ	Reflection Coefficient	
Ω	Solid Angle	[sr]
Φ_R	Required phase distribution	[rad]
Γ	Varactor diodes' junction factor	
μ	medium permeability	[H/m]
ϵ	medium permittivity	[F/m]
δ	Dirac's Delta	
ε	Taylor approximation error function	

Subscripts

max	Maximum
0	Vacuum property
x	Component in x-direction
y	Component in y-direction
θ	Component in theta direction
ϕ	Component in phi direction
I	Isotropic
min	Minimum

Superscripts

$\hat{}$	Unitary vector
$\vec{}$	Vector
$\tilde{}$	Approximation

Acronyms

BJT	Bipolar Junction Transistor
BPF	Bandpass Filter
BW	Bandwidth
CPU	Central Processing Unit
CR	Code Rate
CSS	Chirp spread spectrum
CVO	Convex Optimization
CW	Continuous Waveform
DAC	Digital-to-analog converter
DC	Direct Current
DSSS	Direct Sense Spectrum Spread
EM	Electromagnetic
FEBI	Finite Element Boundary Integral
FEM	Finite Elements Methods
FET	Field-Effect Transistor
FF	Far Field
FNBW	First-Null Beam Width
FOTA	Firmware Over-The-Air
FPGA	Field-Programmable Gate Array
FSK	Frequency-shift keying
FSL	Free-space Loss
GNSS	Global Navigation Satellite System

GPIO	General Purpose Input/Output
HPBW	Half-Power Beam Width
IC	Integrated Circuit
IE	Integral Equation
IF	Intermediate Frequency
IL	Insertion Loss
IoT	Internet of Things
ISM	Industrial, Scientific, and Medical
LED	Light Emitting Diode
LEO	Low-Eart-Orbit
LNA	Low-Noise Amplifier
LNB	Low-Noise Block
MEMS	Micro-Electro-Mechanical Systems
MoM	Method of Moments
NB-IoT	Narrowband IoT
NF	Near Field
PA	Power Amplifier
PEC	Perfect Electric Conductor
PHY	Physical Layer
PIFA	Planar Inverter-F Antenna
PMC	Perfect Magnetic Conductor
PO	Physical Optics
PSO	Particle Swarm Optimization
PSRR	Power Supply Rejection Ratio
PSU	Power Supply Unit
PWM	Pulse Width Modulation
RA	Reflectarray
RF	Radio Frequency
RFID	Radio Frequency Identification
RFO	Radio Frequency Output
RGB	Red, Green, Blue
RL	Return Loss
RLB	Reflectarray-Located Blockage
RX	Receiver
SF	Spreading Factor
SNR	Signal-to-noise ratio
TE	Transversal Electric
TM	Transversal Magnetic
TEM	Transversal Electromagnetic
UC	Unit-cell
UHF	Ultra-High Frequency
VD	Varactor Diode
VSAT	Very-Small-Aperture Terminal
WGA	Waveguide Approach

1 INTRODUCTION

1.1 CONTEXT

The Internet of Things (IoT) concept can be defined as the name given to the set of electrical or electronic devices that are interconnected through the internet, with different functionalities and different processing capabilities, gathering data, which are later converted into a form of "knowledge" in the network [3], [4] e [5]. This concept is increasingly present in everyday life, such as live-in video streaming, augmented reality, autonomous cars, and smart environments [3].

Some argue that IoT aims to introduce the "plug-and-play" concept, aiming for ease of operation, remote access, and reconfigurability, [3]. Others define IoT's main objective as the possibility of interconnection between objects and individuals anywhere at any time or any moment, [5]. But whatever definition one uses, or the understanding of the subject, these objectives are being achieved little by little, as this technology advances.

However, it is worth noting that even though the concept of IoT has already been widely disseminated in recent years, there is still room for improvement, as it is still possible to encounter barriers and challenges for its full operation. One of the challenges is the large amount of devices and data processed. According to Cisco, it is estimated that by 2030, 500 billion devices will be connected to the internet and, according to current projections, this number tends to increase over time [4], which requires robust communication systems, with high data transmission capacity at low latency. In addition to this problem, there is a need for new technologies to ensure not only broadband connectivity, combined with interoperability but also the security, privacy, and reliability issues. Most of these requirements are already being met by several technologies and protocols recently developed, such as the 5G network and IPV6.

Nevertheless, the lack of IoT standardization keeps the challenge of interoperability as an open issue, which must be addressed through standardization – even if it is made generic, allowing the use of different protocols and architectures, who communicate with each other through a "common language" [6].

At this point, it is important to define the basic IoT system architecture, which basically consists of six main elements, namely, identification, sensors, actuators, communication, computation and semantics [7]. The identification block is responsible for addressing network devices, while the sensor block has the function of capturing, storing and transmitting data to a data warehouse. Services are responsible for the functional presentation of the IoT system, providing different classes of services to the user. The identification of an item, in the case of RFID, or the streaming of real-time temperature values, in the case of a sensor network, are some practical examples of the services already available. Semantics consists of the ability to extract knowledge from objects, that is, the efficient use of data from intelligent objects. Finally, the communication block, which

can also be considered part of the sensor, is responsible for connecting objects through different communication technologies and protocols, such as Bluetooth, ZigBee, LoRa, RFID, etc.

The present work will restrict the study to sensors and communication blocks, in order to study and propose a solution for the interoperability problem. The proposed approach of this work is to use a Reflectarray-type antenna to transmit data from sensors, through the LoRaWAN protocol. This generic architecture allows for distance maximization of a communication network, which can be used through different protocols without the need for translation between different standards, or protocols.

1.2 OBJECTIVES

The main objective of this work is to propose a reconfigurable Reflectarray-type antenna, integrated into an IoT system, whose function is to perform data exchange from sensors through a LoRa network. The main objective of this work is to propose a reconfigurable Reflectarray-type antenna, integrated into an IoT system, whose function is to perform data exchange from sensors through a LoRa network. The specific objectives are:

1. Design an active, reconfigurable and compact planar Reflectarray Antenna;
2. Develop a versatile control circuit aiming for beam pattern adjustments, allowing for the implementation of different Beamforming algorithms;
3. Propose a communication system based on LoRa capable of collecting data from sensors and transmitting data using the LoRaWAN® protocol;
4. Study and implementation of convex optimization algorithms for radiation pattern optimization;
5. Integration of the Reflectarray antenna to an Upconverter, whose function is to modulate and re-transmit LoRa signals in Ku band;

1.3 PUBLISHED PAPERS

1. "Design and Optimization of a Compact 10$\times$ 10 Ku-band Reflectarray Antenna", 7th Workshop on Communication Networks and Power Systems (WCNPS 2022).

1.4 DISSERTATION ORGANIZATION

This dissertation is organized as follows: the first chapter discussed the context in which the project is inserted, which is IoT. The second chapter discusses the theory revision of the funda-

mental concepts related to the project. In the third chapter, a comprehensive Reflectarray Antenna design is documented, starting from system requisites, up to EM simulations results. This chapter also includes implementations and discussions about two pattern optimization techniques, namely Convex Optimization and Particle Swarm Optimization. Chapter 4 focuses on the design of the RF board, which includes the Mixer definition, Low Noise Amplifier design, and Bandpass filter design. Finally, Chapter 5 summarizes and discusses the results achieved during the course of the project and concludes the dissertation, proposing future works.

2 FUNDAMENTAL CONCEPTS

2.1 LORA

There are several types of technology used nowadays for IoT applications, such as ZigBee, Bluetooth Low Energy, NB-IoT, and Wi-fi. Each of these technologies is better suitable for a specific set of IoT applications, even though LoRa has gained a lot of attention in many battery-operated embedded systems and its popularity has increased over the past 5 years [8]. In a general sense, LoRa can be defined as communication technology formed by the union of a proprietary specific modulation scheme at the physical layer (PHY) with LoRaWAN network protocol [9], as shown in Fig. 2.1. The advantages of this technology over the others lie in its good trade-off between range, high capacity of devices in the network, battery life, security, and interference immunity.

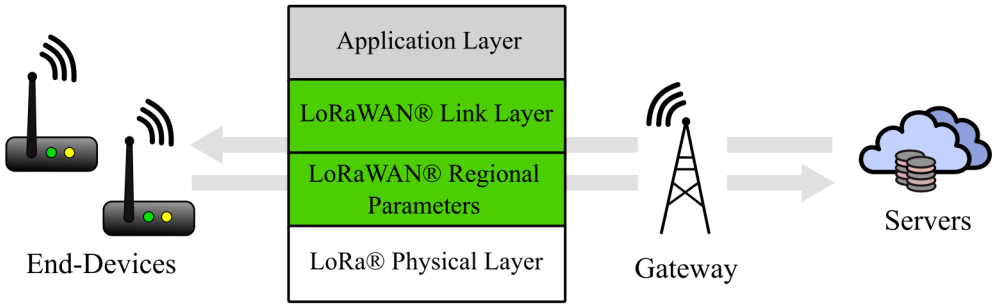

Figure 2.1: Simplified description of a LoRa system

2.1.1 LoRaWAN

LoRa Alliance [10] characterizes LoRaWAN (Long Range Wireless Network) as being a low-power, wide area networking protocol intended for bi-directional communication between battery-operated IoT devices with the internet. As previously mentioned, these IoT devices require bi-directional communication, end-to-end security, mobility, and localization services, and LoRa is in agreement with these requirements, aiming for interoperability between multiple manufacturers and serving as a good candidate for standardizing IoT devices.

LoRaWAN consists of an open standard defining the medium access and other higher layers of the communication stack and it was developed in the star-of-stars topology, where each Gateway communicates with end devices (sensors) which in turn connect to the external network/server. Due to the long-range capability, this technology allows long-range links, through which sensor devices communicate directly with the gateways, not requiring intermediary devices for this purpose. In addition to the previously mentioned bidirectional communication, it also supports

multi-cast addressing groups, which is the transmission of information to several recipients at once, which increases efficiency in using Spectrum during FOTA (Firmware Over-The-Air) and any other messages with high payload to multiple sensors.

End devices are classified into three different categories, which differ in terms of power consumption and latency. The lowest power consumption can be achieved with Class A devices, which are devices whereby the transmission link is followed by two downlink slots. The data transmission is initiated by the end device, in addition to a random time process called ALOHA Protocol, which avoids collision by randomly defining the transmission time slots.

Class B devices are capable of receiving multiple slots at scheduled times, not only after the End-device sends a message, which is done by time-synchronized beacons from the Gateway. Class C is the least in terms of power consumption as it allows nearly continuous receive windows, but features the best latency among all three classes. The differences between classes of end devices are better illustrated in Fig. 2.2

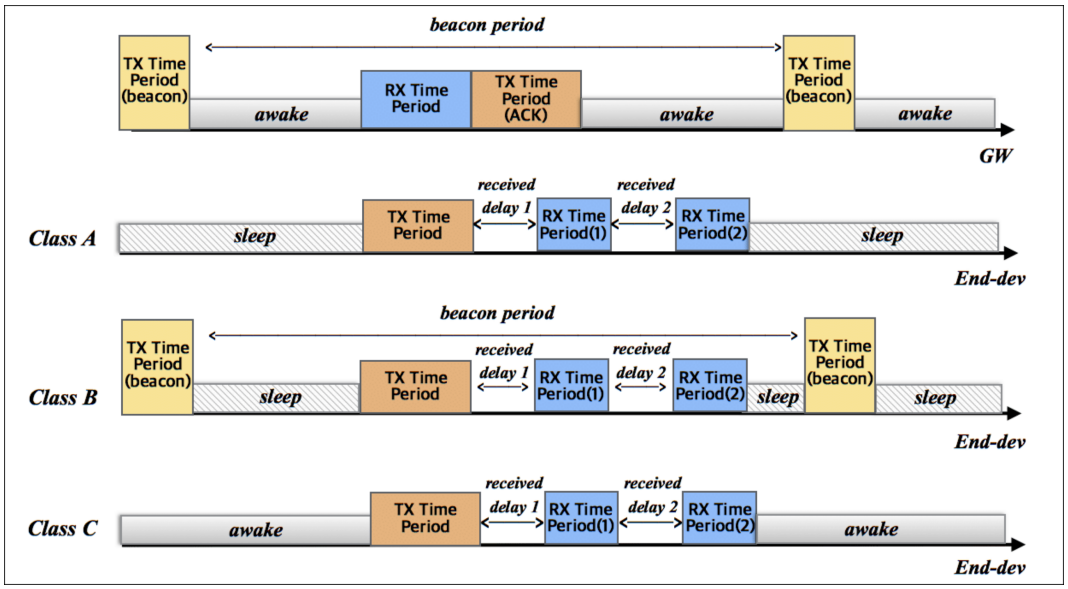

Figure 2.2: Comparison between each class of End device and the Gateway. [1]

2.1.2 LoRa PHY

LoRa PHY was developed by Semtech, and it is based on a chirp spread spectrum (CSS) modulation technique, which is achieved by multiplying (in the time domain) the base-band data signal with a frequency-modulated chirp signal, which is continuously varying in frequency. This technique ensures high channel capacity and higher range, due to the processing gain, which enables a receiver to correctly recover the data signal even when the SNR of the channel is a negative value.

The advantage of this technique over traditional coded spread-spectrum techniques, such as Direct Sense Spectrum Spread (DSSS), is that timing and frequency offsets between transmitters

and receivers are not a concern, which reduces the complexity of the receiver design [11]. This modulation technique results in a constant envelope, similar to FSK modulation, allowing for the use of a low-power high-efficient power amplifier (PA). LoRA PHY also implements an additional proprietary error correction code scheme, which includes data-whitening and interleaving [12], developed for sub-1 GHz ISM bands, which makes this protocol robust to interference.

2.2 ANTENNAS AND ARRAYS

2.2.1 Antennas

Antennas may be defined as reciprocal structures that sample a portion of electromagnetic waves present in the environment, which may carry various data/information, from wireless to wired signals [13], that is, the conversion from guided waves into free space waves, and vice-versa [14]. These devices are governed by Maxwell equations, which are well-known in the literature. Antennas are used not only for wireless communication but also for radars, imaging, and even for medical applications, to mention a few. Antennas can assume a large variety of shapes and characteristics, but this study will be restricted to Reflectarray Antennas, Patch Antennas, and Horn Antennas, as the first is suitable for Ku-band satellite communication antennas, which are generally implemented using horn feed antennas for its suitable gain and good radiation pattern characteristics, and Microstrip Patch Antennas, for its versatility and ease of construction.

2.2.2 Radiation Pattern and Gain

Antennas are often characterized by their gain, directivity, selectivity, and side-lobes suppression. These parameters can be extracted from the Radiation Pattern, which is a graphic representation of the radiation energy, generally given in its polar form, although 3D surface and rectangular representations are also used in some specific cases. The Radiation pattern can be obtained by computing the absolute value of the angular distribution of the radiated energy resulting from a current distribution placed far away from the observation point (far field region), so that the reactive fields do not interfere with the far fields, once its distance is much farther than the spatial extent of the current distribution [15], once the reactive field, associated with the imaginary part of the Poynting vector, is inversely proportional to the distance from the source [16]. For a dipole antenna, this means that

$$r \gg l \quad \text{and} \quad r \gg \frac{2l^2}{\lambda}, \tag{2.1}$$

where r is the distance from the antenna to the observation point and l is the length associated with the spatial current distribution extension, which in this case is the length of the dipole. The second term of Eq. (2.1) is referred to as the Fraunhofer distance. It is worth mentioning that the far-field distance depends on the antenna characteristics, even though Eq. (2.1) is widely accepted in most of the cases [13]. These assumptions simplify the problem of finding the radiation po-

tentials by using a second-order Taylor expansion, which in turn helps to find the radiation fields, by integrating the current densities over the volume containing the antenna current distribution, which results in the following sets of equations:

$$\begin{aligned} \mathbf{E} &= -jk\eta \frac{e^{-jkr}}{4\pi r}\left[\hat{\boldsymbol{\theta}} F_\theta + \hat{\boldsymbol{\phi}} F_\phi\right], \\ \mathbf{H} &= -jk \frac{e^{-jkr}}{4\pi r}\left[\hat{\boldsymbol{\phi}} F_\theta - \hat{\boldsymbol{\theta}} F_\phi\right], \end{aligned} \tag{2.2}$$

where η is the wave impedance, k is the wavenumber and r is the radial coordinate. For rectangular apertures, the surface current distributions are integrated over two dimensions in order to obtain equations similar to the aforementioned. In Eq. (2.2), $k = 2\pi/\lambda$. $\hat{\phi}$ and $\hat{\theta}$ refer to the normalized azimuthal and elevation angle direction, respectively. The radiation pattern is then extracted from the radiation flux, given by the time-averaged Poynting vector, defined as:

$$\mathcal{P} = \frac{1}{2}\operatorname{Re}\left(\mathbf{E} \times \boldsymbol{H}^*\right) = \hat{\mathbf{r}} \frac{\eta k^2}{32\pi^2 r^2}\left|F_\perp(\theta,\phi)\right|^2, \tag{2.3}$$

where $\hat{\mathbf{r}}$ is the unit vector pointed towards the radial coordinate. This equation can be written in the form

$$\left|F_\perp(\theta,\phi)\right|^2 = \left|F_\theta(\theta,\phi)\right|^2 + \left|F_\phi(\theta,\phi)\right|^2 \tag{2.4}$$

An example of a radiation pattern is shown in Fig. 2.3. In this figure, HPBW refers to Half-Power Beam Width, while FNBW refers to First-Null Beam Width, which indicates the angle sector relative to the first null of the radiation pattern. This figure also shows the side-lobe level and the back-side lobe level, which are often undesired and needs to be minimized. It is worth mentioning that the radiation pattern is often normalized, and its shape depends on the antenna size, polarization, and geometry.

The directivity gain of an antenna, often called directivity, is defined as the ratio of the radiation intensity in a given direction from the antenna and relates with the ability of an antenna to concentrate the radiated power in a given direction [17]. The radiation intensity, $U(\phi,\theta)$, can be obtained by deriving Eq. (2.3) with respect to the solid angle, and the directivity gain is achieved by normalizing this value with the isotropic result, which gives

$$D(\theta,\phi) = \frac{U(\theta,\phi)}{U_I} = \frac{U(\theta,\phi)}{P_{\text{rad}}/4\pi} = \frac{4\pi}{P_{\text{rad}}}\frac{d\mathcal{P}}{d\Omega}, \tag{2.5}$$

Where U_I refers to the isotropic radiation intensity and P_{rad}, the total radiated power, which is obtained by integrating the radiation intensity over all solid angles. If this radiated power includes the losses due to radiation efficiency or impedance mismatch, that is, if

$$P_{rad} = e_{cd}\left(1 - |\Gamma|^2\right) P_{in}, \tag{2.6}$$

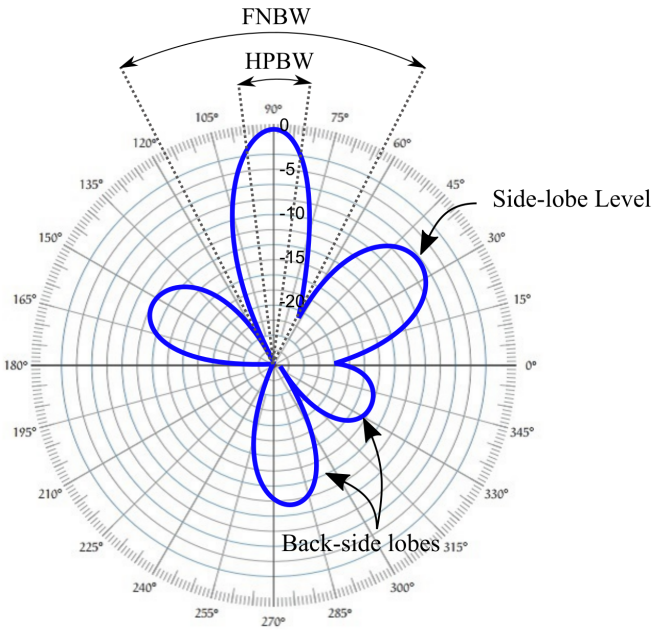

Figure 2.3: Generic radiation pattern of an antenna and its main characteristics

then, Eq. (2.5) can be generalized to the power gain definition, which is given by:

$$G(\theta, \phi) = e_{cd} D(\theta, \phi), \tag{2.7}$$

where P_{in} is the input power. It is worth mentioning that Eq. (2.5) is preferred for the computation of the radiation pattern graphs, instead of Eq. (2.4), since it includes more information about the antenna. The maximum value of Eq. (2.5) is defined as directivity, which is defined by:

$$D_{\max} = \frac{U_{\max}}{U_I}. \tag{2.8}$$

2.2.3 Patch Antennas

In the literature, numerous antenna topologies are used for the unit cell of a reflectarray. However, many of them are just variations of other topologies, performed through modifications or by the addition of parasitic elements designed to solve or mitigate limitations of a certain parameter of the topology on which it was based. It is possible to condense the antenna types used for UCs into three main categories: dipoles, loop, and patch antennas. This document will only cover the patch-type antenna study, as it will be the base for the proposed unit-cell topology.

The patch antennas, most often called "Microstrip Antennas" are one of the most traditional antenna types and are used for many applications, such as RFID, Cellular networks, GNSS receivers, reflectarrays, and phased arrays for Sattelite communication, among others. It was proposed back then in the 1950s and its original form consists of a rectangular patch printed on a thin grounded dielectric substrate [18]. This structure radiates from the fringing fields that are exposed above the substrate at the edges of the patch [15]. These antennas can be modeled by a

different approach, either by considering a lossy cavity [15] or by a loaded transmission line [19].

In the so-called cavity model, the patch is considered to be a resonant cavity. The dimensions of the cavity are approximately $\lambda/2$, depending on the substrate characteristics. With this approach, assuming a rectangular patch structure with $L \geq W$, the resulting resonant fields are given by:

$$\begin{aligned} E_z(x) &= -E_0 \sin\left(\frac{\pi x}{L}\right) \text{ for } -L/2 \leq x \leq L/2, \\ H_y(x) &= -H_0 \cos\left(\frac{\pi x}{L}\right) \text{ for } -W/2 \leq x \leq W/2. \end{aligned} \tag{2.9}$$

By considering an equivalent aperture field extending the patch element by a distance, in order to account for the fringing fields, $\mathbf{E}_a$, related with Eq. (2.9) by $\mathbf{E}_a = \hat{\mathbf{z}} E_z$, it is possible to find the aperture magnetic current, defined by $\mathbf{J_{ms}} = -2\hat{\mathbf{n}} \times \mathbf{E}_a$, from which is possible to obtain the radiation fields, as described in the previous section, which gives

$$F(\theta, \phi) = \cos(\pi v_x) \frac{\sin(\pi v_y)}{\pi v_y}, \tag{2.10}$$

where v_x and v_y are the normalized wavenumbers. The radiation pattern of the patch antenna can be extracted by the normalized gain equation below:

$$g_n(\theta, \phi) = (\cos^2\theta \sin^2\phi + \cos^2\phi)|F(\theta, \phi)|^2. \tag{2.11}$$

2.2.4 Horn Antennas

Horn antennas are derived from the traditional wave-guide antennas, which consists of a type of antenna in which the radiating fields are defined using an aperture, as is the case of slots, open-ended waveguides, reflector, and lens antennas [15]. There are three main types of rectangular horn antennas, H-plane sectoral, E-plane sectoral, and pyramidal horn, which are related to their shape. The former has its size "a" flared out, while in the second model, the size "b" flared. On the latest model, both sides are flared. This section covers only the pyramidal horn, as it was chosen for the reflect array feed antenna.

An aperture antenna can be characterized by applying the Huygens principle in order to obtain the equivalent surface current densities, necessary for the radiating fields obtention, which can be obtained by means of the so-called Kottler's formulas, which are defined by:

$$E = \frac{1}{j\omega\epsilon} \int_A \left[(J_s \cdot \nabla') \nabla' G + k^2 J_s G - j\omega\epsilon J_{ms} \times \nabla' G \right] dS', \tag{2.12}$$

$$H = \frac{1}{j\omega\mu} \int_A \left[(J_{ms} \cdot \nabla') \nabla' G + k^2 J_{ms} G + j\omega\mu J_s \times \nabla' G \right] dS', \tag{2.13}$$

where J_s is the electric surface current density, J_{ms} is defined as magnetic surface current density and G refers to the Green's function relative to the observation point distance (r), which in this case is associated with the far field distance. The radiation vectors of an aperture are obtained by

the spatial Fourier transform of the aperture fields [15], which can be described by:

$$\begin{aligned}\boldsymbol{f}(\theta,\phi) &= \int_A \boldsymbol{E}_a(\boldsymbol{r}')\, e^{j\boldsymbol{k}\cdot\boldsymbol{r}'} dx'dy' = \int_A \boldsymbol{E}_a(x',y')\, e^{jk_x x' + jk_y y'} dx'dy', \\ \boldsymbol{g}(\theta,\phi) &= \int_A \boldsymbol{H}_a(\boldsymbol{r}')\, e^{j\boldsymbol{k}\cdot\boldsymbol{r}'} dx'dy' = \int_A \boldsymbol{H}_a(x',y')\, e^{jk_x x' + jk_y y'} dx'dy',\end{aligned} \tag{2.14}$$

where $e^{j\mathbf{k}.\mathbf{r}'} = e^{jk_x x'} + e^{jk_y y'}$ describes the propagation constants on the aperture's field coordinate. $\boldsymbol{E}_a$ and $\boldsymbol{H}_a$ denote the electric and magnetic aperture fields on the aperture's field coordinate, respectively. By using Eq. (2.14), the radiation vectors can be defined as follows:

$$\begin{aligned}\boldsymbol{F}(\theta,\phi) &= \hat{\mathbf{z}} \times \boldsymbol{g}(\theta,\phi), \\ \boldsymbol{F}_m(\theta,\phi) &= -\hat{\mathbf{z}} \times \boldsymbol{f}(\theta,\phi).\end{aligned} \tag{2.15}$$

For the case of a horn antenna, the propagation of the TE_{10} (Transversal Electric) mode coincides with the tangential aperture fields. For the generic pyramidal horn antenna illustrated in Fig. 2.4, the aperture fields can be defined as

$$\begin{aligned}E_y(x,y) &= E_0 \cos\left(\frac{\pi x}{A}\right) e^{-jkx^2/2R_a} e^{-jky^2/2R_b} \\ H_x(x,y) &= -\frac{1}{\eta} E_0 \cos\left(\frac{\pi x}{A}\right) e^{-jkx^2/2R_a} e^{-jky^2/2R_b}.\end{aligned} \tag{2.16}$$

By replacing the relationships $\sigma_a^2 = A^2/2\lambda R_a$, $\sigma_b^2 = B^2/2\lambda R_b$, and $k = 2\pi/\lambda$, Eq. (2.16) can be rearranged to

$$\begin{aligned}E_y(x,y) &= E_0 \cos\left(\frac{\pi x}{A}\right) e^{-j(\pi/2)\sigma_a^2(2x/A)^2} e^{-j(\pi/2)\sigma_b^2(2y/B)^2} \\ H_x(x,y) &= -\frac{1}{\eta} E_0 \cos\left(\frac{\pi x}{A}\right) e^{-j(\pi/2)\sigma_a^2(2x/A)^2} e^{-j(\pi/2)\sigma_b^2(2y/B)^2}\end{aligned} \tag{2.17}$$

Using Eq. (2.17), one can achieve the radiating fields of the horn antenna by applying the spatial Fourier transform of the propagating mode of the electric field, which has only y-component, as the TEM_{10} condition was applied in this case. The result was evaluated by [15] in terms of the Fresnel diffraction integrals. which results in

$$\begin{aligned}E_\theta &= j\frac{e^{-jkr}}{\lambda r} E_0 \frac{AB}{4} \left(\frac{1+\cos\theta}{2}\right) \sin\phi F_1(v_x,\sigma_a) F_0(v_y,\sigma_b) \\ E_\phi &= j\frac{e^{-jkr}}{\lambda r} E_0 \frac{AB}{4} \left(\frac{1+\cos\theta}{2}\right) \cos\phi F_1(v_x,\sigma_a) F_0(v_y,\sigma_b)\end{aligned} \tag{2.18}$$

The gain of a horn antenna is obtained by the ratio between the radiated power in a given direction, with the same power irradiated by an isotropic antenna, as defined previously defined in Eq. (2.5). In this definition the radiation intensity can be obtained by the derivative of Eq.

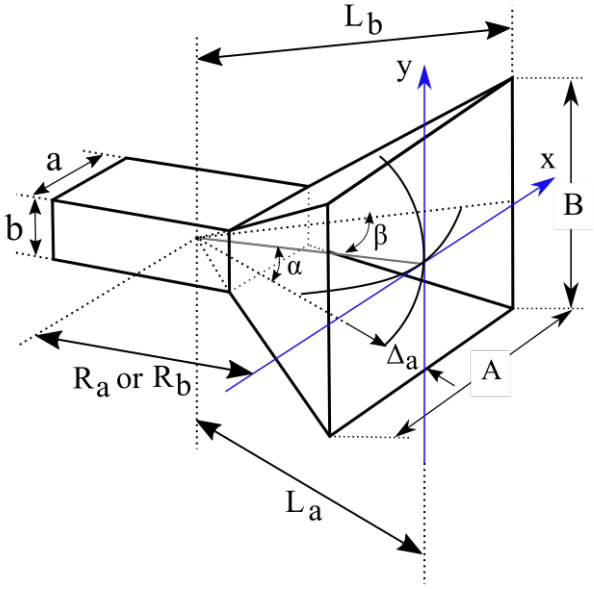

Figure 2.4: Generic horn antenna showing the coordinate system and the lengths considered in the equations.

(2.3), where the radiating fields defined in Eq. (2.18) are used in this case, resulting in

$$G_h = 4\pi \frac{U_{\max}}{P_{\text{rad}}} = \frac{4\pi}{\lambda^2}(AB)\frac{1}{8}\left|F_1\left(0,\sigma_a\right)F_0\left(0,\sigma_b\right)\right|^2 = e\frac{4\pi}{\lambda^2}AB, \tag{2.19}$$

where $U_{\max}$ is the maximum value of $U(\theta,\phi)$ and depends on the values chosen for σ_a and σ_b, which generally coincides with the forward direction, that is when $v_x = v_y = 0$. This happens when $\sigma_b < 1.54$. It is worth mentioning that the radiation pattern found in Eq. (2.18) is often approximated by the so-called $\cos^q$ pattern [2], [20], [21]. For an x-polarized Reflectarray (RA), the approximated field is given by

$$E_x(r,\theta,\phi) = A_0\left[\hat{\theta}\cos^{q_e}(\theta)\cos\phi - \hat{\phi}\cos^{q_h}(\theta)\sin\phi\right]\frac{e^{-jkr}}{r}, \tag{2.20}$$

while for a y-polarized field,

$$E_y(r,\theta,\phi) = A_0\left[\hat{\theta}\cos^{q_e}(\theta)\sin\phi + \hat{\phi}\cos^{q_h}(\theta)\cos\phi\right]\frac{e^{-jkr}}{r}, \tag{2.21}$$

in which A_0 is a complex constant and q_e, q_h are positively defined constants required to adjust the radiation pattern with the desired one. By using Eq. (2.8), it is possible to associate the maximum achievable gain that can be obtained from Eq. (2.20) and 2.21 for $\theta = 0$, which results in

$$D(\theta = 0) = \frac{2\left(2q_E+1\right)\left(2q_H+1\right)}{q_E+q_H+1}. \tag{2.22}$$

It is worth noting that D only depends on both q_e and q_h constants. For pyramidal horn antennas

it may be convenient to express $q_e = q_h = q$, this case is illustrated in Fig. 2.5, which shows the gain plot of Eq. (2.22) as a function of q.

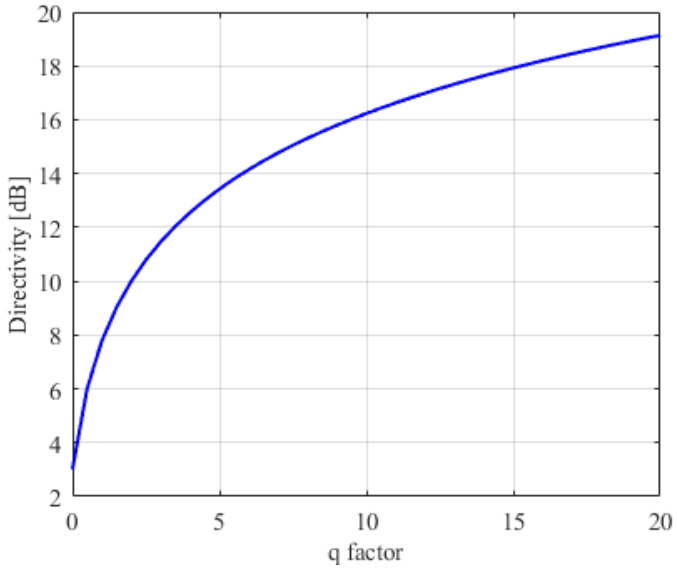

Figure 2.5: Directivity as function of q, where $q = q_e = q_h$ is the constant for a $\cos^q$ feed approximation.

2.2.5 Antenna Arrays

Single antennas are useful for many applications, playing an essential role in many communication fields, such as GNSS, Wi-fi, Bluetooth, and IoT-based networks, but in some cases, the need for highly directive antennas limits the effectiveness of these antennas, especially, but not limited to, long distances and radar applications [2], where highly directive antennas are needed. In order to increase the gain of the antennas, one can either enlarge the size of the antenna or assemble a set of radiating elements placed at some specific electrical and geometrical configuration, forming an antenna array [17].

According to [15], array of antennas is used to focus the radiated power towards a desired angular sector. The shape of unit cells, number of elements, geometrical arrangement, and excitation tapers will set the angular pattern that must be achieved. It means that in addition to higher gain, arrays also provide additional control of the radiation fields, enabling the use of many beamforming techniques such as multi-beam patterns, shaped beams, and adaptive radiation patterns, which makes this type of antenna an attractive solution for countless applications, replacing the traditional dish reflector antennas. There are several types of antenna arrays, phased arrays, including linear arrays and planar arrays, transmitarrays, and reflectarrays are some examples. The present study will be restricted to the study of the last, reflectarray.

The analysis of a planar array can be exemplified by the isotropic phased-array structure shown in Fig. 2.6. At first, a plane wave incident upon this array is considered, with an incident angle of θ_b relative to the array normal, inducing a current on the n-th element that assumes the form:

$$i_n = A\, e^{jnk_0 d \sin\theta_b}, \tag{2.23}$$

where A is a complex constant accounting for the magnitude and phase of the incident wave, k_0 is the wave number in a vacuum and d is the distance between two unit cells. Eq. (2.23) is also valid for the case of a reflectarray if the feed is placed at the far-field region. In this case, A also accounts for the feed pattern. In Fig. 2.6, it is possible to see that, because of the linearity of Maxwell´s equations, the total field will result from the sum of the contribution of each individual field, which results in the so-called array factor (if the constant A is normalized):

$$E_a(\theta, \phi) = A \cdot \sum_{n=1}^{N-1} = a_n e^{j(\Psi_n + nkd\sin\theta)}, \tag{2.24}$$

where a_n and Ψ_n refers to the amplitude and phase control over each excitation.

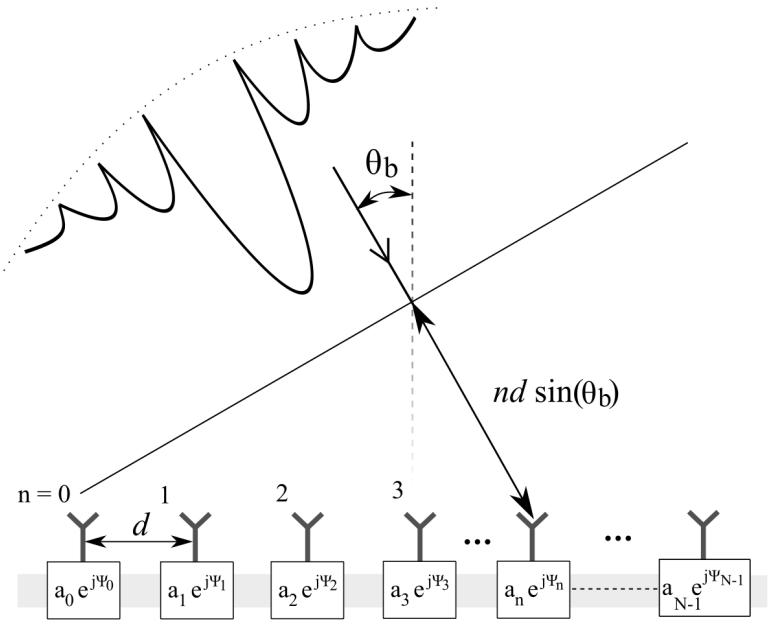

Figure 2.6: Generic isotropic phased array in receive mode.

2.3 REFLECTARRAY ANTENNAS

2.3.1 Description of a Reflectarray

Reflectarray antennas (RAs) can be defined as reflector antennas that aim to convert the spherical electromagnetic waves transmitted by a feed antenna to a planar wave during the reflection and re-transmission [2]. These antennas were created as alternatives to dish antennas, due to the need for high-gain and flexible, in terms of reconfigurability, and ease to manufacture antennas.

If compared with traditional phased-array antennas, RAs have the advantage of lower loss and lower production cost [2], [22], but its drawbacks are the feed blockage, which was already solved by the emergence of the so-called transmitarrays, and the narrow bandwidth. In contrast dish antennas, RAs have the advantages of relatively lower cost, larger beam scanning angles, and ease to manufacture [2]. However, it provides lower radiation efficiency, and high simulation/ development time.
It is worth mentioning that different radiating elements may be used for the reflecting surface other than microstrip patches. Structures such as dipoles [23], rings [24], and waveguides [22] are widely used as unit cells of the array. In fact, microstrip-based RAs gained attention only in the 1980s, even though RA papers started being published in the 1960s. These antennas are generally designed to achieve high gain and narrow beam-width, as for the ease of scalability of this kind of antenna [15], but it is also possible to find small-sized active RAs [25],[26],[27], [28].

An example of RA geometry is shown in Fig. 2.7. In this figure, θ_b and ϕ_b indicate the elevation and azimuth angle related to the beam steering direction. h is the height of the feed antenna and R_i refers to the distance between the Horn's phase center to each "i" element in the array. These quantities will be used later for the array analysis.

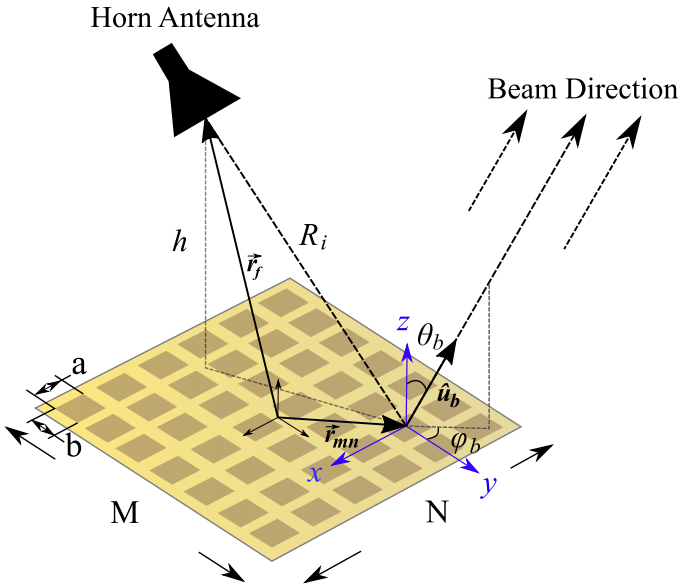

Figure 2.7: Generic illustration of a microstrip-based reflectarray geometry.

In order to start a RA geometry design, the first step is to know the desired gain and define the feed location. At this point, the polarization and unit cell design must be already defined. The gain of the reflectarray can be achieved by the normalized radiation pattern of the unit cell and by approximating the radiation pattern of the feed with the term $\cos\theta$, as like Eqs. 2.20 and 2.21, in which q is set to 1. For the generic rectangular geometry shown in Fig. 2.7, the estimated gain is achieved by the following relationship [29]:

$$G = \eta_{ap} \frac{4\pi}{\lambda_0^2} M.N.a.b.A_{uc}(\theta, \phi) \cos\theta, \tag{2.25}$$

where the product $a.b$ indicates the effective area of the unit cell, while $M.N$ indicates the number of elements in each principal planes of the array, that is, along x and y coordinates. The unit cell pattern is described as $A_{uc}(\theta, \phi)$, but can also be written as $A_{uc}(\hat{u})$, as $\hat{u}$ indicates the observation direction. The variable η_{ap} consists of the aperture efficiency, which includes the illumination (η_{ill}), spillover (η_{spl}) and phase error (η_{p}) efficiencies, but it could also include reflection loss (η_{r}), so that

$$\eta_{ap} = \eta_{\text{ill}} \eta_{\text{spl}} \eta_{\text{r}} \eta_{\text{p}}. \tag{2.26}$$

The phase error efficiency η_{p}, arises from phase errors introduced by divergences in the reflector's surface phase distribution. Although it is more pronounced in 1-bit elements, due to the phase discretization, it is also present in continuous phase distributions. In this case, it is caused either by the initial assumption of an infinite array or by edge diffraction [30], even tough it could also be caused due to high sensitivity on the elements used for the unit cell [31].

In most cases, Eq. (2.26) can be approximated by considering only η_{ill} and η_{spl}, since these quantities has more effect on η_{ap} [32]. If one considers a center-fed RA, the former can be defined as

$$\eta_{\text{ill}} = \frac{[((1 + \cos^{q+1}\theta_0)/(q+1)) + ((1 - cos^q\theta_0)/q]^2}{2\tan^2\theta_0[(1 - \cos^{2q+1}\theta_0)/(2q+1)]}, \tag{2.27}$$

In which θ_0 is half of the subtend angle (HPBW) and $q = q_e = q_h$ refers to the same constant related to the feed pattern approximation used in Fig. 2.5. By considering the same assumptions, the spillover efficiency is given as follows:

$$\eta_s = 1 - cos^{2q+1}\theta_0. \tag{2.28}$$

Eq. (2.25) can be solved either by iteration process, or by fixing one dimension as a constraint of the problem. After defining the array gain, the feed location can be obtained, which is mainly dependent on the aspect ratio (f/D), where D is the array diameter, for circular RA geometries, or the principal plane dimension for the case of rectangular structures. In general, the f/D ratio can be defined based on the HPBW of the feed antenna [33], by the relationship

$$f/D = \frac{1}{2\tan\theta_0}, \tag{2.29}$$

where $\theta_0 = \text{HPBW}/2$, or it can be alternatively chosen based on the aperture efficiency analysis, fixing specific design constraints such as the frequency of operation. Fig. 2.8, John Huang used Eq. (2.27) and (2.28) to illustrate how to chose f/D ratio based on the aperture efficiency by fixing the array size and feed pattern characteristics for a 32-GHz half-meter RA with 33.4° beamwidth feed pattern.

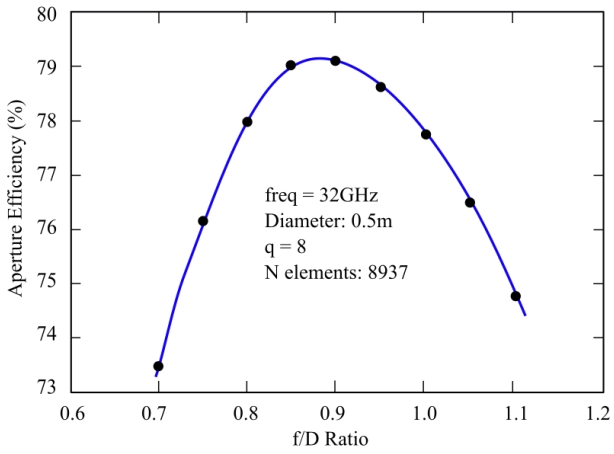

Figure 2.8: Aperture efficiency vs f/D ratio. Source: [2], adapted.

Although Eq. (2.25) can be used for first approximations, the fields calculation should consider the contribution of both the feed field pattern and elements radiation pattern, which differs from the classic phased array design. The strength of the field is also related to the distance R_i, due to the free-space loss. The sampled field can be defined by the following relationship

$$F_s = \frac{F(\vec{r}_{mn} \bullet \vec{r}_f) \cdot A_{uc}(\vec{r}_{mn} \bullet \hat{u}_b)}{FSL}, \tag{2.30}$$

where $FSL = (\lambda_0 R_i)/4\pi$ and refers to the free-space loss. $\vec{r}_{mn}$ is the position vector of the (m,n) element considering the general coordinate system shown in Fig. 2.7, which in this case was chosen to be at the center of the reflectarray $\vec{r}_f$ is the position vector of the feed antenna and $\hat{u}_b$ indicates the beam direction. F_F refers to the feed pattern, while A_{uc} refers to the unit cell pattern function. By using the bi-dimension array summation, it is possible to achieve the radiating fields

$$E(\hat{u}) = \sum_{m=1}^{M}\sum_{n=1}^{N} F_F\left(\vec{r}_{mn} \bullet \vec{r}_f\right) \cdot A\left(\vec{r}_{mn} \bullet \hat{u}_b\right) \cdot A\left(\hat{u} \bullet \hat{u}_b\right) \cdot e^{jk\left(\left|\vec{r}_{mn} - \vec{r}_f\right| + \vec{r}_{mn} \bullet \hat{u}\right) + j\Phi_R}, \tag{2.31}$$

where $\hat{u}$ defines the notation for the observation direction, which can be alternatively defined with the θ, ϕ, in the spherical coordinate system and Φ_R refers to the required compensating phase of the mnth element, which can be defined by

$$\Phi_R = k\left[R_i - \left(x_m \cos\varphi_b + y_n \sin\varphi_b\right)\sin\theta_b\right]. \tag{2.32}$$

In this equation, R_i refers to the phase delay on each element, which is also defined as

$$R_i = \sqrt{h^2 + (x_m - x_{\text{feed}})^2 + (y_n - y_{\text{feed}})^2}. \tag{2.33}$$

2.3.2 Passive Reflectarray Antennas

As usual in planar reflector antennas, RAs must also change the phase distribution of the reflector in order to compensate for the spatial arrangement arising from the planar structure. In microstrip passive RAs this is generally achieved by either mapping the reflected phase physically, by using an array of patch antennas with varying sizes, or by adding different sizes stubs to identical-sized patch cells, as shows Fig. 2.9 (a) and Fig. 2.9(b), [34], [2]. These methods also applies for circularly polarized antennas, where the radiating elements are rotated in order achieve circular polarization, as shows Fig. 2.9(c).

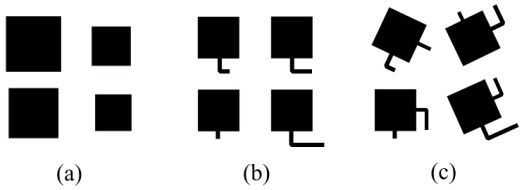

Figure 2.9: Passive RA elements, (a) patches with varying sizes, (b) identical patches with attached stubs, (c) rotated patches with stubs.

For microstrip RAs, rectangular patch antennas are also the most widely used configuration, which can be justified by its actractive radiation pattern characteristics, and low cross-polarization radiation [35], The design process of a rectangular patch antenna unit cell starts by first matching the patch antenna with a $50\,\Omega$ microstrip line, similar to the conventional microstrip antenna design. The size of the patch antenna is set in order to resonate with the center frequency. The feed port is replaced by a stub and the unit cell is analyzed by considering Full-wave analysis, in which the dimensions of the stub are mapped in terms of reflection phase. It is worth mentioning that the reflected magnitude is worse at the resonant frequency of the patch antenna, because at this frequency, a small portion of the field is scattered in the substrate as it interacts with the ground plane.

For the case of patches with different sizes, the design process is generally carried out by first choosing the initial patch dimensions so that it resonates at the center frequency of the specific application. After optimizing the geometry using full-wave analysis, the phase shift over frequency is obtained for different patch sizes. It is worth mentioning that in both cases, for patch sizes close to the center frequency, or small stubs sizes, the phase will drastically change with small size variations due to the resonance characteristic.

Although passive RA designs have gained their space in several space communication applications, where weight, size and power consumption are limiting factors, it does not allow beam scanning, unless mechanical structures are added to it. For that reason, Active RAs has gained space for its higher radiation efficiency and flexibility if compared with other beam-steering antennas.

2.3.3 Active Reflectarray Antennas

Recently, in order to achieve reconfigurable RA topologies, active components such as diodes, and transistors were introduced to these antennas, from which was possible to obtain beam steering capability, power combining techniques, and polarization flexibility, among others. This work will be focused in the beam scanning capability.

To achieve beam scanning capability, it is necessary to insert circuits that electronically controls the reflected phase in a range of at least $360\,^{\circ}$ [25]. There are several ways to achieve an electronic control over the phase distribution. In the literature, it is common to find articles that uses PIN diodes [26], [36] or Varactor diodes [37],[38], as switching devices to turn ON/OFF or gradually tune the reflection phase response, respectively. In the case of PIN diodes, the diode acts as a switch device. Fig. 2.10 shows how these two options are used in practice. For the Varactor diode, the phase reflection response is continuous over the bias voltage, while for the PIN diode operating as a switch, there are only two possible states for the reflection phase (Forward and reverse, or zero, bias conditions). It is worth mentioning that the reflection phase response is not linear in both cases, which leads to a bandwidth limitation, even though PIN diodes allows for slightly higher bandwidth, lower insertion loss, and simpler control circuits when compared to Varactor diodes [36], [28].

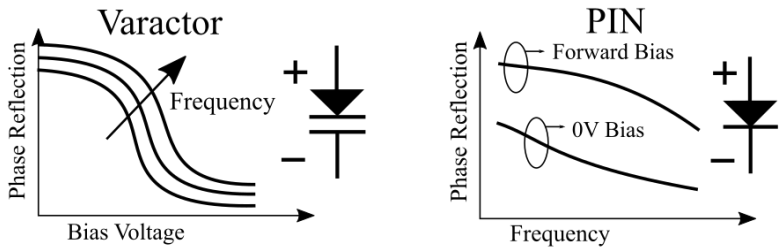

Figure 2.10: Illustration of a typical Varactor diode-based unit cell reflection phase response (a), and typical PIN diode-based unit cell reflection response.

It is also possible to tune the reflection phase by using micro-electro-mechanical systems (MEMS) structures [39] or taking advantage of the anisotropic property of dielectric substrates such as liquid crystals [40], although these topologies are less common and will be not covered by this dissertation.

In literature, there is also a predominance of rectangular patches for the radiating structure geometry, as is the case for passive RAs. This is exemplified by [41], that uses four rectangular patches in the unit cell. In this article, the radiating cell is composed by four square patch elements, in which two diagonal elements are connected with a PIN diode. When this diode is directly polarized, the reflected phase changes of $\pm\,90\,^{\circ}$ relative to the incident wave. Thus, the author shows that it is possible to perform a $180\,^{\circ}$ phase change, which is sufficient for a 1-bit binary case. This topology offers some interesting characteristics, such as the use of few active components per cell, simplicity of construction, low manufacturing cost and low reflection loss

($< 1\,\text{dB}$), in addition to having a wide bandwidth ($8.7\,\text{GHz}$ to $10.1\,\text{GHz}$). On the other hand, the disadvantage of this topology is the low radiation efficiency.

Another example of a topology based on rectangular patch elements is highlighted by [28]. This is similar to the previous topology in its principle of phase change, which is achieved by a PIN diode between two patch elements. However, in this article, the unit cell consists of a square patch element cut by a slit positioned in the middle of the patch. The interaction between the two rectangular metallic structures resulting from the cut, is done by the PIN diode. With this topology, it was possible to generate $180\,^\circ$ of phase change between the two states of the PIN diode. The advantages of this topology compared with the former is the even simpler construction and design. This design achieved a wide bandwidth ($4.5\,\text{GHz} - 5.5\,\text{GHz}$) and low reflection loss ($< 0.9\,\text{dB}$). The disadvantages are its low aperture efficiency, $15.26\,\%$, and a bulky control circuit.

To solve the problem of low aperture efficiency, [36] proposes an alternative approach, by placing the diode on the opposite side of the radiating patch. This reduces the effects of the diode on the current distribution of the radiating element. PIN diodes are also used in [27] with a slightly different behavior. In this case, the diode is placed at the edge of the patch. This way, when the diode is directly polarized, the patch antenna is shorted at this point, which changes the phase distribution of the unit cell, than changing the reflected phase. But this topology also suffers from low aperture efficiency.

As mentioned before, some effort were spent on increasing the radiation efficiency of RAs, minimizing design complexity, and reducing power consumption. However the problem of high side lobes level, which occurs specially in small size RA with binary structures, is not covered as much by previous works [42], [2]. This problem is caused mainly due to the phase errors introduced in the phase dicretization process and the lower sampling resolution in small size antennas, but it is also related to diffracted fields from the edges of the antenna array, specular reflected components due to the ground plane, and feed blockage effect. In fact, gain improvement by optimizing the reference phase of the binary threshold was addressed by [27] and [43], but distortions were observed in the main lobe after optimization. This work will focus on the design of a low-profile RA with optimized side-lobe suppression.

2.3.4 Blockage Effect

One of the disadvantages of reflector antennas, such as parabolic and planar RAs, stands for the feed blockage introduced by the feed antenna. This problem is more prominent in center-fed RAs and has been addressed by either using offset feed configuration or by placing the feed antenna on the opposite side of the array on the so-called Transmitarrays [44], [45]. This occurs because the feed antenna is generally positioned within the near-field radiation zone, on the same side of the radiation propagation [15], which can be observed by Eq. (2.1).

One way to account for this blockage effect is to consider a shadow produced on the reflector

by an infinite-located point, described as Reflectarray-Located Blockage (RLB) in [46]. By using this assumption, it is possible to approximate the blockage effect on the radiation pattern by nulling the fields in the elements/section covered by the shadow, which means consider that the fields reflected by the antenna structure are $180°$ out-of-phase. This is illustrated in Fig. 2.11.

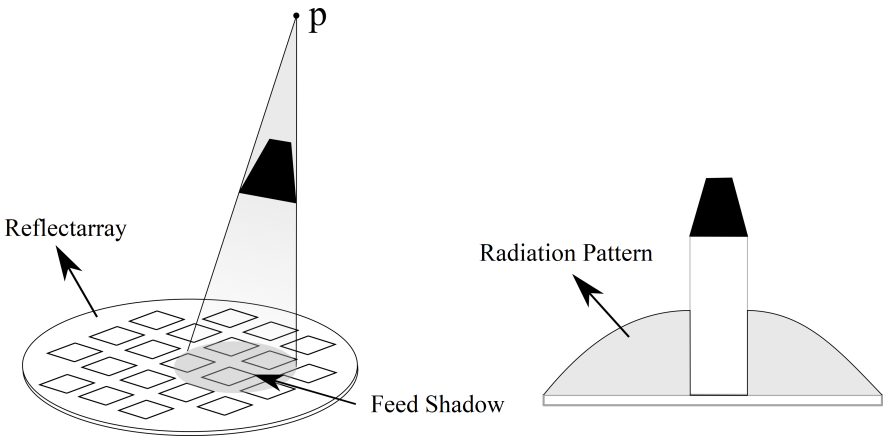

Figure 2.11: Reflector/reflectarray-located blockage effect computation by a horn antenna, due to a point "p" located at an infinite distance from the reflectarray, resulting in the figure in right, which illustrates the nulled fields within the shadow.

In order to implement this approach, the array factor described by Eq. (2.31) was used for a centered-fed 20×20 rectangular aperture with $5\lambda \times 5\lambda$ and 0.5λ spacing. Under these constraints, it is possible to achieve the shadow mask shown in Fig. 2.12. The far-field generated by nulling the fields highlighted as "feed projection" is shown in Fig. 2.13. In this figure, it is possible to see the difference between the initial radiation pattern (without considering feed blockage effects) and the field producced by the distribution shown in Fig. 2.12.

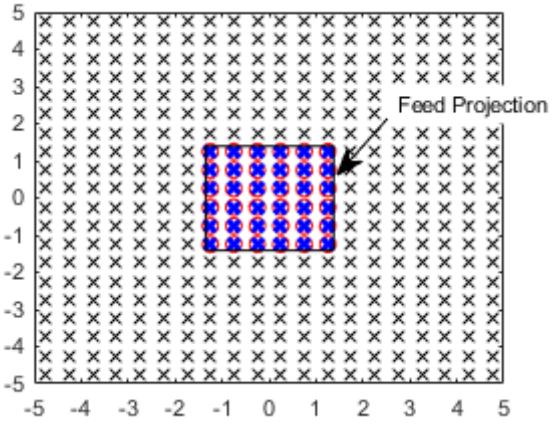

Figure 2.12: Top View of an array modeled with point antennas reflectarray with a rectangular-shaped feed antenna. The blue crosses illustrates the antennas in which the fields will be cancelled.

From Fig. 2.13, it is possible to observe a noticeable increase in the side-lobe levels, which is mainly due to the gain reduction, even tough its not shown in this figure once its normalized. But it is worth mentioning that side-lobe level increase are also reported in [47] as consequence of the blockage effect.

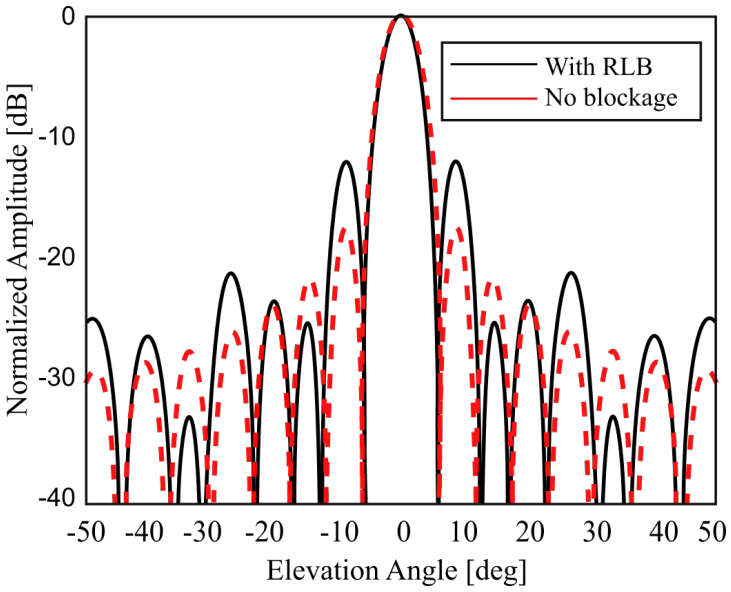

Figure 2.13: E-Plane Co-polarized normalized radiation pattern of a centered-fed 20×20 rectangular aperture with $5\lambda \times 5\lambda$ and 0.5λ spacing.

In order to increase the accuracy of the feed blockage effects under the RLB approach, one could implement the null-field hypothesis for each element, instead of the far-field generated by the array. In this case, each element radiation pattern is nulled in the feed direction (by each element). This approach is illustrated by Fig. 2.14.

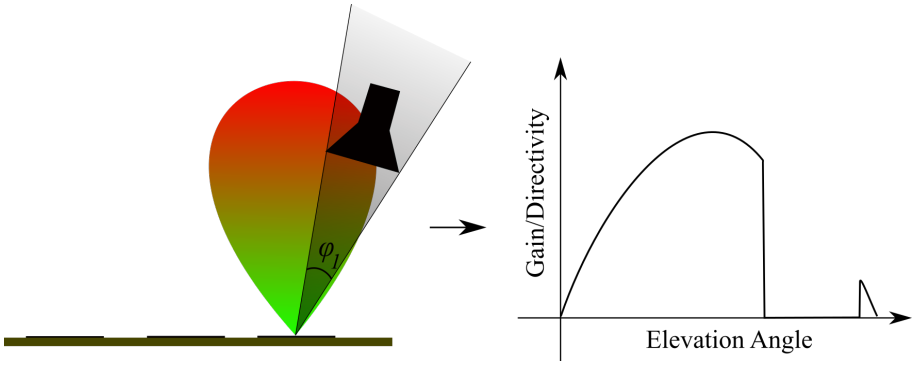

Figure 2.14: Feed blockage of a RA by considering the fields generated by each unit cellindividually. In this case, a typical rectangular patch antenna field is illustrated.

In this figure, φ_1 refers to angle sector related with the feed location. For the case of rectangular feed structures, the shadow can be computed by considering each corner separately, as shown in Fig 2.15 for a generic feed position. The shadow mask relative to each coordinate and the spherical coordinate transformation code used to implement this approach is detailed in Appendix I. Fig. 2.16 shows the result obtained by this approach, in which is more clear the increase of the side-lobe levels and the gain decrease.

It is worth mentioning that this method only gives a first-order estimation of the blockage effect, and its accuracy is limited to the main lobe level estimation [47]. More accurate models

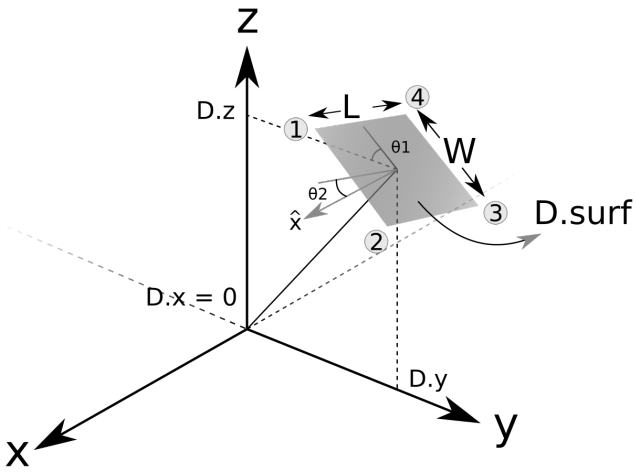

Figure 2.15: Coordinate system and variables used to compute the blockage effect locally to each unit cell individually.

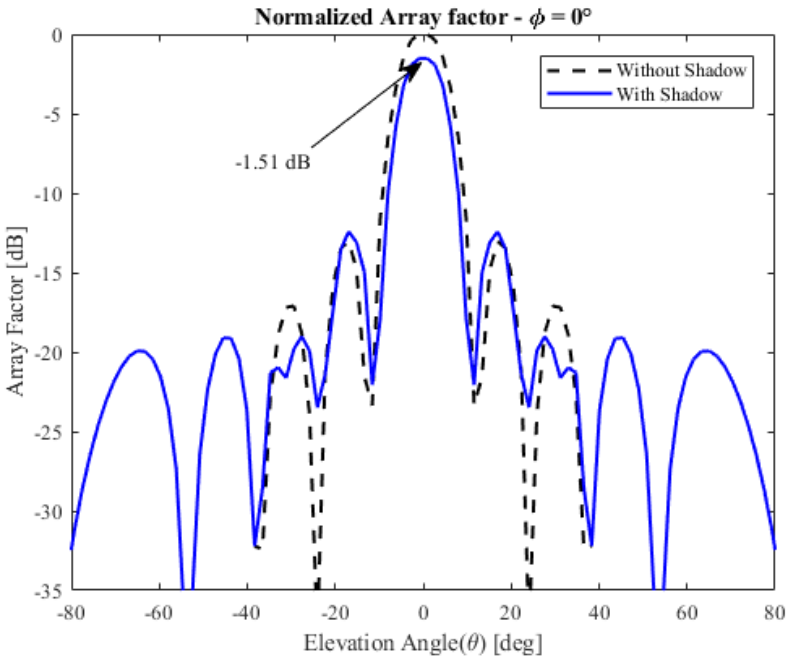

Figure 2.16: E-Plane radiation pattern comparison between ideal radiation pattern (without blockage effect) and the improved-RLB approach.

are also presented [46], but it was also addressed by [48] using hybrid PO/NF-FF method, which consists of near-field to far-field transformation combined with null-fill hypothesis to estimate the effect of complex structures on the far-field pattern and beam efficiency of reflector antennas.

2.4 DIODES

2.4.1 Varactor Diodes

Varactor diodes can be defined as a special kind of diode that enhances the junction capacitance property of PN junction when its reverse-polarized. Since the leakage current is very low under this condition, its basically a voltage-operated device [49]. Its construction is highlighted in Fig. 2.17, where dimensions of the contact area and the body are determined in order to minimize the parasitic resistance and to maximize the junction capacitance. This capacitance is non-linear and depends on both diode geometry and the fabrication process, specially regarding the doping characteristics near the junction, which is generally classified in three types, abrupt, hyper-abrupt and graded junctions. Its capacitance can be determined by

$$C(V) = \frac{C_0}{(V/\Phi_D + 1)^\gamma}, \tag{2.34}$$

where C_0 is the diode capacitance at 0V bias voltage and γ is the term associated with the junction characteristics. For abrupt junctions, $\gamma \approx 0.47$, while for graded junctions, $\gamma \approx 0.3$. For hyper-abrupt, $\gamma > 0.5$ [50]. Φ_D is defined as contact potential, which ranges from 0.5 to 1.0 V [51]. These diodes are generally specified to have a high Q-factor, for high-frequency operation and low leakage current, but it is also specified according to the desired value of gamma (γ), which affects the capacitance change curve behavior, as it will be described later.

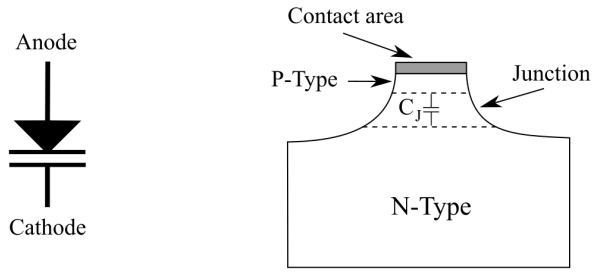

Figure 2.17: Illustration of a typical Varactor diode construction and its symbol.

The reverse operation of the Varactor diode can be modeled by the equivalent circuit displayed in Fig. 2.18. In this circuit, C_{case} and $G(V)$ can be neglected in high-Q devices, which is generally the case of Ku-band applications. Among the parasitic effects, the lead inductance and the series resistance are of the main concern, as it limits both the operation frequency and its figure of merit (Q-factor).

The main advantages of using VD's are the low current consumption and the possibility of generating continuous phase distributions, while the big disadvantage is the high reverse voltage generation needed to achieve a high dynamic range on capacitance value, which leads to bulky circuits (based on DAC's) needed to control each diode bias state.

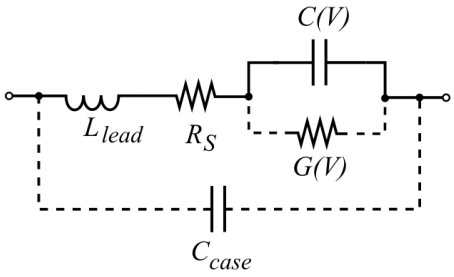

Figure 2.18: Equivalent RLC model for the Varactor diode operating in the reverse bias.

2.4.2 PIN Diodes

In contrast with Varactor diodes, PIN Diodes are current controlled devices that operates as a variable resistors at microwave frequencies [52]. These devices are widely used in RF electronics for many applications, such as power limiters, phase shifters, attenuators, modulators and RF switches, which is the case of study for this research.

A typical PIN diode construction is described in Fig. 2.19. It is made by a triple junction between n-doped, intrinsic, and p-doped semiconductors layers with epitaxial topology.

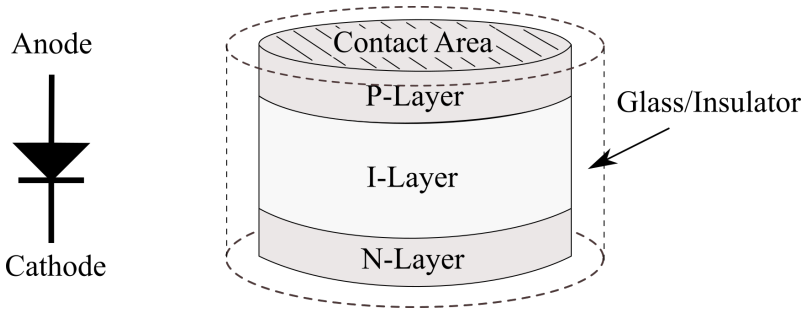

Figure 2.19: Illustration of the construction of a PIN.

The intrinsic layer is sandwiched between the two strongly-doped semiconductors and it works like a wide depletion layer, if compared with conventional rectifiers. At reverse bias, because of the absence of mobile carriers, an open circuit state is established, allowing for a good RF isolation. On the other hand, when the diode is forward biased, mobility carriers are injejcted in the I-region, so that as a variable current is generated. It is worth mentioning that the carrier life time is not critical for this type of diode, specially for RF applications.

PIN diodes RF characteristics are typically modeled by RLC circuits. These circuits may also include both parasitic effects and non-linear behavior [53], which leads to different topologies. A simple equivalent model is described in Fig. 2.20, with two different equivalent circuits accounting for the forward and reverse bias states.

Typical values for C_T ranges between $0.1 - 0.5\,\text{pF}$ for Ku-band applications. The parasitic inductance L depends on the package dimensions but it is usually less the $1\,\Omega$ [54]. It is worth mentioning that R_P can be neglected sometimes due to its very high value, on the order of tens of

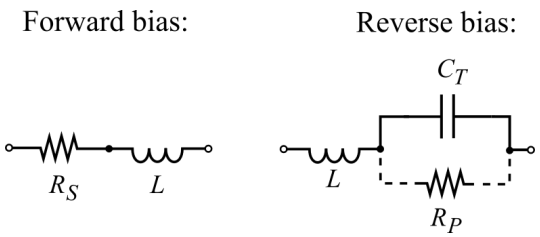

Figure 2.20: Equivalent model of the PIN Diode. R_S describes the forward bias resistance, where L is a fixed quantity related with the parasitic inductance, R_P is the parasitic resistance of the intrinsic layer and C_P summarizes the junction, package and intrinsic layer capacitance's.

kilo-ohms. Under this assumption, the equivalent impedance related with each state of PIN diode can be modeled by two equations:

$$Z(j\omega) = R_S + j\omega L, \tag{2.35}$$

$$Z(j\omega) = j\left(\frac{\omega L C_T - 1}{\omega C_T}\right). \tag{2.36}$$

Fig. 2.21 and 2.22 shows the impedance plot for the SMP1340 diode equivalent circuit, calculated from Fig. 2.35 and 2.36, respectively.

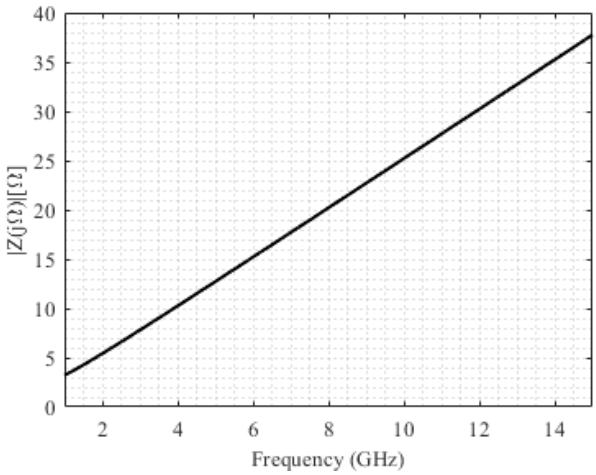

Figure 2.21: Module of the PIN Diode Forward bias impedance, based on SMP1340-007LF parameters: $R_S = 3\,\Omega$, $C_T = 0.03\,\text{pF}$, $R_P = \infty$ and $L_S = 0.4\Omega$.

In Fig. 2.21, it is possible to observe that for high frequencies, the parasitic inductance outweighs the series resistance, which leads to a predominantly imaginary positive impedance. If compared to Fig. 2.22, the impedance in the reverse bias mode is about 10 times greater, but still high enough to provide some isolation. By using the same parameters of SMP1340-007LF diode in a $Z_0 = 50\,\Omega$ system, the insertion loss is $0.27\,\text{dB}$, and the isolation is $13.2\,\text{dB}$ at $11.95\,\text{GHz}$, which were obtained by

$$\text{IL} = 20\log_{10}[1 + R_S/(2Z_0)], \tag{2.37}$$

$$\text{ISO} = 10\log_{10}[1 + 1/(2Z_0\omega C_T)^2]. \tag{2.38}$$

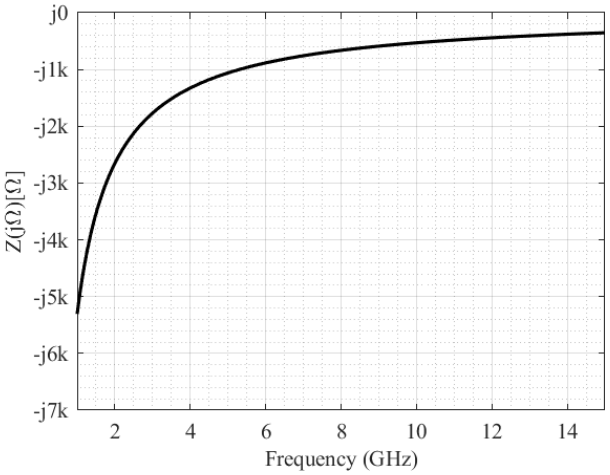

Figure 2.22: PIN Diode Reverse bias impedance, based on SMP1340-007LF diode. Where $R_S = 3\,\Omega$, $C_T = 0.03$ pF, $R_P = \infty$ and $L_S = 0.4\Omega$.

2.5 PATTERN OPTIMIZATION

2.5.1 Convex Optimization

Pattern optimization or pattern synthesis is often used in RA's and phased arrays to generate shaped beams, or steered beams [55], which is implemented in order to circumvent many adverse effects such as feed blockage, specular reflection due to the ground plane, phase errors, edge diffraction, coupling between adjacent elements, and other behaviors that are not easily predicted by analytic calculation or simulations such as the non-linear behavior of diodes, surface roughness, and the biasing circuit mismatch, lower gain, and high side-lobe levels. In Active RAs, the phase errors introduced in the phase discretization process and the lower sampling resolution are the characteristics that most influence the radiation pattern, specially in small-size antennas, even tough diffracted fields from the edges and specular reflection, and feed blockage effect, also becomes noticeable under this circumstances, leading as consequence, lower gain, higher side-lobe levels and field pattern distortions.

One way to overcome these undesired effects is to use convex optimization, which guarantees an optimal solution and generally achieve fast convergence time if compared with evolutionary algorithms. A generic convex optimization problem can be described as follows:

$$\text{minimize } f_0(x) \tag{2.39a}$$

$$\text{subject to } f_i(x) \leq b_i,\ i = 1, 2,\ ...,\ m, \tag{2.39b}$$

where $f_0(x)$ is the objective function, $f_i(x)$ are the constraints functions, and b_i are bounds of these constraints, and m is the number of constraints functions, or bounds [56]. These class of problem presumes both objective and constraints functions to be convex, which means to satisfy

$$f_i(\alpha x + \beta y) \leq \alpha f_i(x) + \beta f_i(y) \tag{2.40}$$

for all $x, y \in \mathbf{R}^n$ and all $\alpha \in \mathbf{R}$ with $\alpha + \beta = 1$, $\alpha \geq 0$ and $\beta \geq 0$ [56].

Unfortunately, for many RA synthesis problems, the objective functions are often nonconvex especially for phase-only optimization. Some ways to overcome this limitation are to linearize the problem by manipulating it algebraically [57], or by implementing the Semi Definite Relaxation technique [58].

The first technique consists of optimizing element locations. For the purpose of applying this algorithm for RA synthesis, let us first define the normalized far-field pattern radiated by the RA, for the continuous phase distribution, which can be obtained by simplifying Eq. (2.31), which leads to

$$f(\theta, \phi) = \frac{1}{N^2} \sum_{\mathrm{n,m}=1}^{N} i_{\mathrm{m,n}} e^{j(\Phi_R - k_0 R_{\mathrm{n,m}})} e^{jk_0(x_{\mathrm{n}} \cos u_x + y_{\mathrm{m}} \cos v_y)}, \tag{2.41}$$

in which N is the size of the array in each direction, x_{n} and y_{m} refers to the positions of the elements, $i_{m,n}$ incorporates the terms $F\left(\vec{r}_{mn} \bullet \vec{r}_f\right)$, $A_{uc}\left(\vec{r}_{mn} \bullet \hat{u}_b\right)$, and $A_{uc}\left(\hat{u} \bullet \hat{u}_b\right)$ in Eq. (2.31), and $k_0 = 2\pi/\lambda_0$. $\cos u_x$, $\cos v_y$ are the directional cosines, defined by

$$\cos u_x = \sin\theta \cos\phi, \quad \cos v_y = \sin\theta \sin\phi. \tag{2.42}$$

The iterative process consists of applying the linearization of the phase component around the current solution at iteration k by first defining

$$\Phi_R^k = \Phi_R^{k-1} + \varepsilon, \tag{2.43}$$

and applying the Taylor approximation $e^{j\varepsilon} = 1 + j\varepsilon$, which is valid if $|\varepsilon| \ll 1$. This way, the radiation field at iteration k is determined by

$$f_\varepsilon^k(\theta, \phi) = \frac{1}{N} \sum_{\mathrm{n,m}=1}^{N} (1 + j\varepsilon_{\mathrm{n,m}}) e^{j(\Phi_R^{k-1} - k_0 R_{\mathrm{n,m}})} \cdot e^{jk(x_{\mathrm{n}} \cos u_x + y_{\mathrm{m}} \cos v_y)}. \tag{2.44}$$

The optimization problem is then defined as follows:

$$\min_{\varepsilon} \rho, \quad \text{under} \begin{cases} \sup\limits_{(\theta,\phi) \in S} \left| f_\varepsilon^k(\theta, \phi) \right| \leq \rho \\ |\varepsilon_n| \leq \alpha \text{ and } |\varepsilon_n| \leq \alpha, \\ \qquad\qquad n = 1, \ \ldots, \ N \end{cases} \tag{2.45}$$

in which ε defines the accuracy of the solution with respect to the Taylor approximation, limiting the value of ε, and S define the complementary region of the main lobe.

2.5.2 Particle Swarm Optimization

The initial problem described above can be alternatively solved by using Particle Swarm Optimization (PSO), which consists of an algorithm inspired by social behavior of bird flocking or fish schooling. This algorithm is used many research fields, including electromagnetics and pattern synthesis of antenna arrays [55]. It is considered to be a versatile tool as it can be adjusted by only a few variables. Its formulation is given as follows

$$v_{ij}^{(k+1)} = wv_{ij}^{(k)} + c_1 U_{1j}\left(y_{ij}^{(k)} - x_{ij}^{(k)}\right) + c_2 U_{2j}\left(y_{sj}^{(ik} - x_{ij}^{(k)}\right), \tag{2.46}$$

$$x_{ij}^{k+1} = x_{ij}^{k} + v_{ij}^{k+1}, \tag{2.47}$$

in which the first term of Eq. (2.46) is the inertia of the current particle, associated with the velocity, v_{ij}. The second and third terms refer to the cognitive component and social components, respectively. y_i is the best individual position and y_s is the global best position among the swarm and the output is given by x_{ij}.

For this specific problem, the required phase distribution was modeled as x_{ij}, and the values of x were considered to be continuous. The optimization problem can be formulated by

$$\min_{x_{i,j}} \sup_{(\theta,\phi)\in S} \left|f^k(\theta,\phi)\right|, \quad \text{under} \begin{cases} x_{ij} < X_{max} \\ x_{ij} > X_{min} \\ v_{ij} > X_{min} \\ i = 1,\ \ldots,\ S \\ j = 1,\ \ldots,\ A, \end{cases} \tag{2.48}$$

in which X_{max} and X_{min} limit the search region, S refers to the number of particles of the swarm and N defines the array size.

2.6 SIMULATION TECHNIQUES

2.6.1 Waveguide Approach (WGA)

In order to obtain the reflection phase response of a unit cell, which is needed in order to map the phase distribution of the array, the reflection coefficient (Γ) must be known. This quantity is related with the ratio of the reflected and incident fields. In literature, a few methods are used in order to obtain this parameter, if one consider a plane wave propagating in the z-direction, the reflection coefficient of the electric field component can be written as [59]:

$$\Gamma = \frac{\boldsymbol{E_r}}{\boldsymbol{E_i}} = \frac{\hat{\boldsymbol{x}}\Gamma E_0 e^{+jk_0 z}}{\hat{\boldsymbol{x}} E_0 e^{-jk_0 z}} \tag{2.49}$$

It is worth noting that Γ is a complex quantity, which accounts for both magnitude and phase

response of the reflecting surface. For the WGA case, the fundamental TEM mode is propagated through a wave-guide structure closed by a pair of perfect electric conductor (PEC) and perfect magnetic conductor (PMC) walls, as shown in Fig. 2.23.

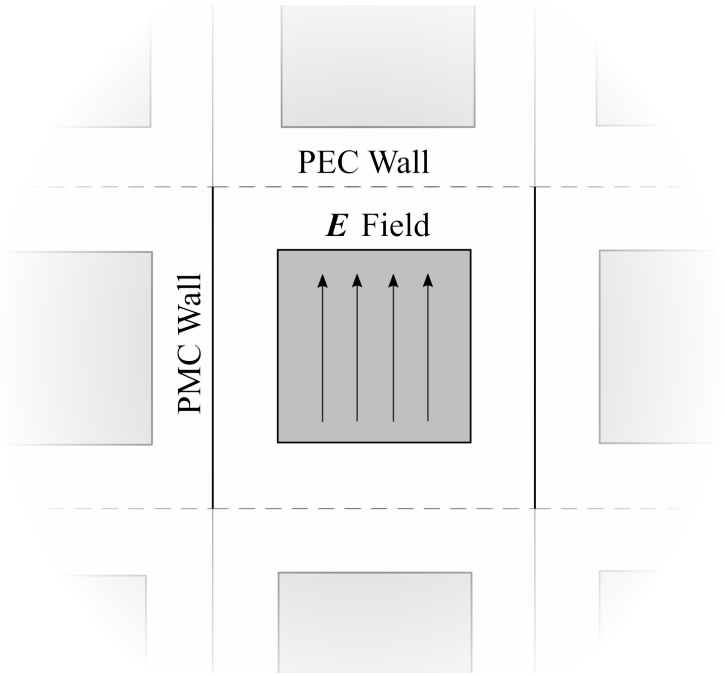

Figure 2.23: Wave guide cross section for WGA.

By image theory, it is possible to deduce that the these walls can be replaced by an infinite periodic array fed by a incident plane wave. In this case, the elements reflection phase curves are obtained by the reflection coefficient of the TEM wave in the equivalent wave guide [60].

2.6.2 Floquet Modes Approach

Another approach broadly used to obtain the reflected response of the unit cell is the Floquet-based method. The formulation of Floquet-type port/ excitations is based on the spatial Fourier series, with minimal modifications [61]. For the unidimensional case, on the x-axis, the following surface current distribution is considered, which is evaluated on the port surface, at $z = 0$. [62]

$$\mathbf{I} = \hat{y} \sum_{n=-\infty}^{\infty} f(x - na)\, e^{(-jn\varphi)}, \tag{2.50}$$

where f is a complex function. It is possible to observe that Eq. (2.50) consists of a periodic complex function with period a, since:

$$\mathbf{I}(x + a) = \mathbf{I}(x) \tag{2.51}$$

from which is possible to conclude that the fields match with each other at the boundaries of the cell, except for the phase delay. The solution of the electromagnetic fields associated with the

current distribution described above, which is directly related to TM_y modes, can be obtained by choosing a potential vector that satisfies the following Helmholtz scalar equation:

$$\nabla^2 A_y + k_0^2 A_y = -J_y, \tag{2.52}$$

where J_y is the volume current density, which can be expressed in terms of the surface current by the relationship $J_y\,\hat{\mathbf{y}} = \delta\mathbf{I}$. Solving Eq. (2.52) using Floquet Series, which is detailed by [61], it is possible to achieve the electric fields written in terms of an infinite sequence:

$$E_y = -\frac{\pi\omega\mu_0}{a}\sum_{n=-\infty}^{\infty}\frac{\tilde{f}\,(k_{xn})}{k_{zn}}\,e^{(j\omega t - jk_{xn}x - jk_{zn}z)}, \tag{2.53}$$

In this equation, the exponential term represents the Floquet modes in the $k_x \times k_z$ plane, where $\tilde{f}(K_{xn})$ is the spatial transform of $f(x)$ and the terms k_{xn} and k_{zn} defines the direction of propagation of the nth Floquet mode, which can be interpreted as the superposition of plane waves. Typically, only a finite number of modes beyond the fundamental tone propagates. The number of Floquet modes to be modeled using the computational tools will depend mainly on the scanning angles ϕ and θ, and the height of the unit cell analyzed. A rule of thumb is to add all modes whose attenuation is below 50 dB [63].

2.6.3 Method of Moments (MoM)

Until now, the previous methods described different ways to model the unit cell to obtain its reflection response. In order to implement these techniques, it is necessary to use some numerical techniques to solve complex integrals or differential equations, which in most cases do not have an explicit analytic solution. One of the most used technique so solve integral equations for planar structures is the Method-of-Moments (MoM), which is consists on the process of taking moments by multiplying with weighing functions and integrating them [64]. This method is used mainly to solve complex integral or differential equations and it can be implemented by four steps:

1. derivation of the appropriate integral equation (IE);
2. discretization of the IE into a matrix equation using basis functions and weighting functions,
3. evaluation of the matrix elements, and
4. solving the matrix equation and obtaining the parameters of interest.

The first step is achieved by integrating differential equations and considering the boundary and initial conditions, so that the integral form is obtained. This process is generally carried out by means of the Green's function, which forms a link between the differential and integral equations for boundary-valued problems.

The second step consists of approximating the solution of the problem with a series of expan-

sion functions. To explain it, one can consider the generic inhomonegeous equation

$$L(\Phi) = g, \tag{2.54}$$

where L is a linear operator, g is known and denotes the source function, and Φ is the solution of the problem. The approximation consists of

$$\tilde{\Phi} = \sum_{n=1}^{N} a_n f_n, \tag{2.55}$$

where a_n are the expansions coefficients and f_n are the expansions functions. By substituting Eq. (2.54) into Eq. (2.55), and taking the inner product with the weighting functions $w_1, w_2, ..., w_n$, the last two steps are covered, which results in:

$$\sum_{n=1}^{N} a_n \langle w_m, L f_n \rangle = \langle w_m, g \rangle , \quad m = 1, 2, \ldots, N, \tag{2.56}$$

or it can be alternatively written in the matrix form as

$$[A_{mn}][X_n] = [B_m], \tag{2.57}$$

where $A_{mn} = \langle w_m, L f_n \rangle$, $B_m = \langle w_m, g \rangle$ and $X_n = a_n$. The solution is found by solving Eq. (2.57) for X. At this point, it is worth mentioning that the weighting functions can be chosen with different types, such as

- collocation,
- subdomain method,
- Galerkin method,
- least squares method.

2.6.4 Finite Elements Method (FEM)

Another numerical technique extensively used to solve EM problems is the FEM. If compared with MoM, its a more powerful and versatile technique used to solve problems with complex geometries inserted in inhomogeneous media. It consists of dividing the solution region into a finite number of elements, and to approximate the solution, by deriving the governing equations for each element and assembling the final result. The implementation of this method takes place by following four essential steps:

1. discretizing the solution region into a finite number of elements;
2. deriving governing equations for a typical element,

3. assembling of all elements in the solution region, and

4. solving the system of equations obtained.

Fig. 2.24 exemplifies the discretization process of a simple cross-section of a transmission line with two conductors over a substrate by using tri-node triangular mesh.

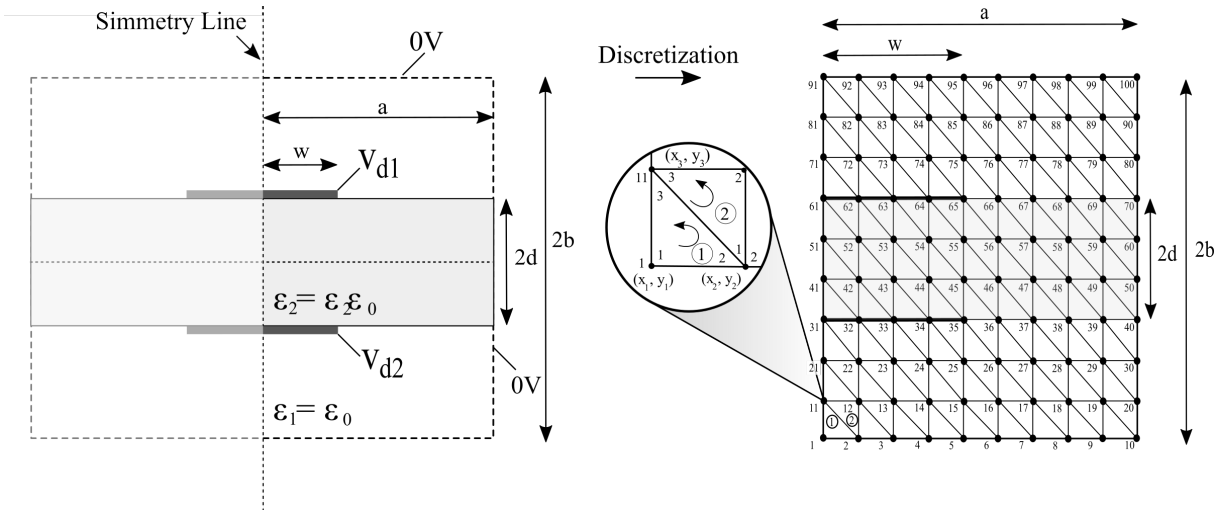

Figure 2.24: Cross section of a double-strip line, illustrating an example of FEM application.

The next step of FEM, after discretization, is to derivate the governing equations related with the problem, which in this case is given by the Laplace's equation, namely:

$$\nabla^2 V = 0. \tag{2.58}$$

To do so, the energy is used as functional corresponding to Laplace's Equation. The problem is solved by minimizing the functional,

$$W_e = \frac{1}{2}\int \epsilon \left|\mathbf{E}_e\right|^2 dS = \frac{1}{2}\int \epsilon \left|\nabla V_e\right|^2 dS. \tag{2.59}$$

In this equation, V_e is the approximation of the solution V, which generally assumes polynomial form. For the tri-node mesh, this polynomial is defined as $V_e(x, y) = a + bx + cy$, and E_e is the Electric field within the element, which is defined by the relationship

$$\mathbf{E_e} = -\nabla V_e = -(b\mathbf{a}_x + c\mathbf{a}_y). \tag{2.60}$$

The element governing equations can be obtained by applying the $V_e(x, y)$ definition to the element highlinghted in Fig. 2.24, which results in

$$V_e = \sum_{i=1}^{3} \alpha_i(x, y) V_{ei}. \tag{2.61}$$

where

$$\begin{aligned}\alpha_1 &= \frac{1}{2A}\left[(x_2y_3 - x_3y_2) + (y_2 - y_3)\,x + (x_3 - x_2)\,y\right],\\ \alpha_2 &= \frac{1}{2A}\left[(x_3y_1 - x_1y_3) + (y_3 - y_1)\,x + (x_1 - x_3)\,y\right],\\ \alpha_3 &= \frac{1}{2A}\left[(x_1y_2 - x_2y_1) + (y_1 - y_2)\,x + (x_2 - x_1)\,y\right],\end{aligned} \tag{2.62}$$

and A is the area of the element, defined as

$$A = \frac{1}{2}\left[(x_2 - x_1)\,(y_3 - y_1) - (x_3 - x_1)\,(y_2 - y_1)\right]. \tag{2.63}$$

By using Eq. (2.61), it is possible to rewrite Laplace's Equation into the following form:

$$\nabla V_e = \sum_{i=1}^{3} V_{ei}\nabla\alpha_i, \tag{2.64}$$

where 'i' refers to the nodes of the triangles. By inserting Eq. (2.64) into Eq. (2.59), after some algebraic manipulation, it is possible to get into the matrix form:

$$W_e = \frac{1}{2}\epsilon\left[V_e\right]^t\left[C^{(e)}\right]\left[V_e\right], \tag{2.65}$$

where $C^{(e)}$ is defined as:

$$C_{ij}^{(e)} = \int \nabla\alpha_i \cdot \nabla\alpha_j dS. \tag{2.66}$$

After assembling the equations related with the problem, the solution can be finally found by deriving Eq. (2.65) and equating to zero.

2.6.5 Hybrid Finite Element Boundary Integral (FEBI) Method

The methods described previously are useful for solving many complex EM problems, but each one will perform better under specific conditions. MoM is often indicated to be better suited for planar transmission-line problems, while FEM is generally recommended for 3D radiation problems [65], [66].

The hybrid method proposed by [67] consists of applying the equivalence principle to transform the original problem into interior and exterior problems coupled on the exterior dielectric body surface through the continuities of the tangential electric field and magnetic field. The interior problem is solved by the finite element method, and the exterior problem is solved by the moment method. The equivalence principle is illustrated by Fig. 2.25. In this figure, E^i and H^i refers to any illumination of an field incident on the surface S, which could represent fields generated by the horn antenna for the case of RA. J_a and F_b are the equivalent electric current, and the tangential magnetic field, respectively, which generates the same fields (E^i, H^i) by the Equivalent principle. The two problems on the leftside of Fig. 2.25 are coupled by the boundary

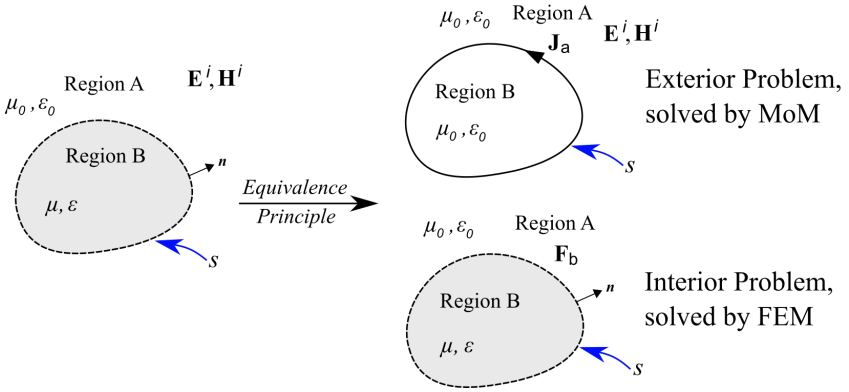

Figure 2.25: Illustration of the Equivalence Principle applied to a general problem.

continuity conditions

$$\begin{aligned} \mathbf{n} \times \mathbf{E}_a &= \mathbf{n} \times \mathbf{E}_b, \quad \text{on } S \\ \mathbf{n} \times \mathbf{H}_a &= \mathbf{n} \times \mathbf{H}_b = \mathbf{F}_b, \quad \text{on } S. \end{aligned} \tag{2.67}$$

For the external problem, the electromagnetic fields in "region a" is composed by the scattered field generated by the equivalent surface electric current density $\mathbf{J}_a$ on S, and the incident field,

$$\begin{aligned} \mathbf{E}^a &= \mathbf{E}^i + \mathbf{E}^s\left(\mathbf{J}^a\right) \\ \mathbf{H}^a &= \mathbf{H}^i + \mathbf{H}^s\left(\mathbf{J}^a\right). \end{aligned} \tag{2.68}$$

On the other hand, the electromagnetic fields in "region b"can be described fully by the tangential magnetic field on S, which gives

$$\begin{aligned} \mathbf{E}^b &= \mathbf{E}^b\left(\mathbf{F}^b\right) \\ \mathbf{H}^b &= \mathbf{H}^b\left(\mathbf{F}^b\right) \end{aligned} \tag{2.69}$$

By using these equivalent fields the problem described by Eq. (2.68) is solved by a similar procedure described previously for the MoM, while Eq. (2.69) is used for solving the FEM problem, also described in previous sections.

The FEBI Method was used in this work for simulation of the full reflectarray design in HFSS®, since it consists of a relatively large structure and because it can accurately and efficiently simulate very complex, large open problems [65]. FEM was used for simulating the unit cell design, since its the best suited for low complexity inhomogeneous problems, while MoM was used for filters/diplexer and for bias-tee designs.

3 DESIGN OF THE REFLECTARRAY ANTENNA

3.1 LINK BUDGET AND SYSTEM CONSTRAINTS

The proposed satellite communication datalink is described in Fig. 3.1. It is composed of three LoRa devices. The first device consists of an end device tied to a RA, followed by the LEO satellite, which is also composed of a LoRa-like transceiver, translating the data sent by the sensor (end device) and transmitting it to the Gateway. At this point, it is worth mentioning that the satellite transceiver works as an end device itself, containing a CPU and sufficient memory working as a buffer, which size is dictated by the specific application. The idea is to up-convert

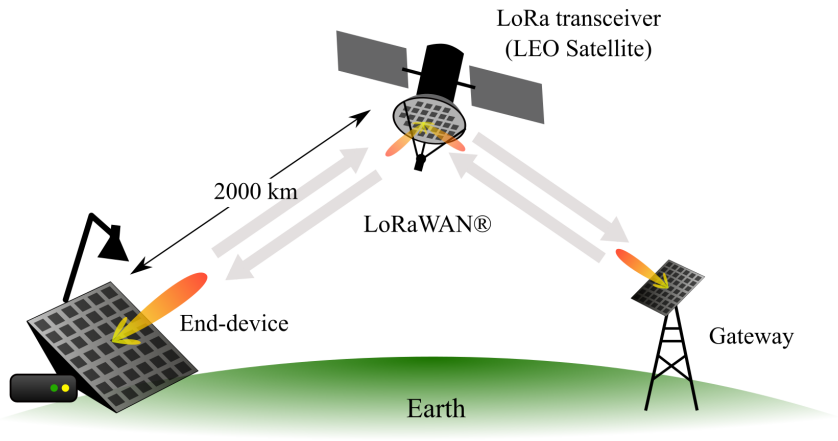

Figure 3.1: Illustration of the LoRa-based satellite communication datalink.

LoRa signals from 915MHz to transmit in the Ku-band (11.95 GHz). In order to calculate the link budget for this project, the data rate must be known, as per Shannon's theorem on channel capacity,

$$R_b \leq \log_2(1 + \text{SNR}). \tag{3.1}$$

Due to the spread spectrum characteristic of the LoRa protocol, it is possible to correctly recover the data signal even when the SNR of the channel hits a negative value, which "elevates" the noise floor by the so-called processing gain, which is given by

$$G_p = 10 \log_{10}(R_c/R_b) = 26.3\,\text{dB} \tag{3.2}$$

In this equation, $R_c = BW$ and

$$R_b = SF \frac{\left(\frac{4}{4+CR}\right)}{\left(\frac{2^{SF}}{BW}\right)}, \tag{3.3}$$

where SF refers to the spread factor while CR refers to to the so-called code rate. For the slowest possible configuration for LoRa transmission, in which $CR = 1$, $SF = 12$, and $BW = 125\,kHz$, it is possible to achieve $R_b \approx 293\,b/s$, $R_c = 125\,kHz$. Under these assumptions, and considering

a typical 5 dB receiver noise figure, the sensitivity can be calculated as follows:

$$P_{\text{sensitivity}} = -174\,\text{dBm} + 10\log_{10} BW + NF - G_p = -144.3\,\text{dBm}, \tag{3.4}$$

where $-174dBm$ stands for thermal noise floor at room temperature in a 50Ω system and NF refers to the receiver noise figure. If one considers an altitude of $2000\,\text{km}$ for the satellite, which is the maximum for LEO [68], the free-space loss is given by

$$\text{FSL} = 10\log_{10}\left(\frac{4\pi r}{\lambda}\right)^2 = 180\,\text{dB}. \tag{3.5}$$

At this point, it is worth mentioning that the same RA is considered for satellite, gateway and end devices. If one considers the maximum LoRa transmission power (P_T) $14\,\text{dBm}$ ($25\,\text{mW}$), and a $15\,\text{dB}$ upconverter loss (L_{CV}), it is possible to estimate the required RA gain from the Friis formula, from which is possible to obtain

$$G_{RA} \geq \frac{P_{\text{sensitivity}} - P_{T(\text{dBm})} + \text{FSL} + L_{CV(\text{dB})}}{2} \approx 18.35\,\text{dB}. \tag{3.6}$$

3.2 UNIT CELL DESIGN

3.2.1 Geometry description

The first step in the RA design consists of choosing the unit cell geometry and extracting the unit cell's reflection response. The geometry chosen for this work is depicted in Fig. 3.2. It is based on the traditional printed square patch antennas, with two parallel PIN diodes in the middle of two closely spaced patches. Similar topologies were investigated previously in [41] and [28], but the proposed configuration with two diodes placed in parallel proved to be successful in reducing the reflection loss and improving performance for high-frequency Ku-band applications.

The principle of operation is as follows: when the diodes are directly polarized, the two patches are electrically connected by a low impedance path, which makes them to operate at a lower resonant frequency. When the diode is in reverse polarization (or at 0V bias), it creates a high impedance path, "isolating" these two patches, which forces them to operate independently, now at a higher frequency.

3.2.2 Obtaining the Reflection Phase Response

Floquet-based excitations/boundaries described in section 3.2 were used for the process of obtaining the reflection response, with was implemented with FEM simulation in Ansys HFSS® environment. Only two fundamental modes were used in this case, with m,n = 0. The distance between the unit cell and the Floquet Port was set to approximately $\lambda_0/2$. This distance was chosen based on the attenuation level of higher-order modes. In order to improve calculation time,

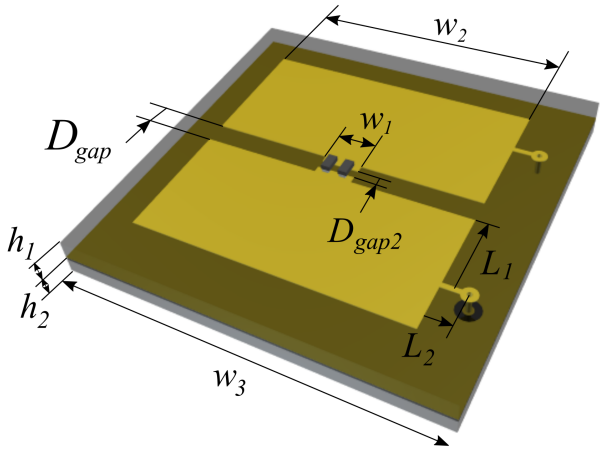

Figure 3.2: Illustration of the proposed unit cell, isolated from the array. This structure was used in order to obtain the reflection phase.

all metals of the unit cell were considered to be Perfect Electric Conductor (PEC) materials. After parametric simulations using Floquet Ports, the optimal reflected phase and reflection coefficients were obtained from the reflection coefficient of the fundamental modes. The optimized result is shown in Fig. 3.3, where black traces refer to the ON-state and the blue traces refer to the OFF-state of the diode. Dash traces define the reflected magnitude response, while solid traces refers to the reflected phase. The optimal values for the unit cell geometry are listed in Tab.3.1.

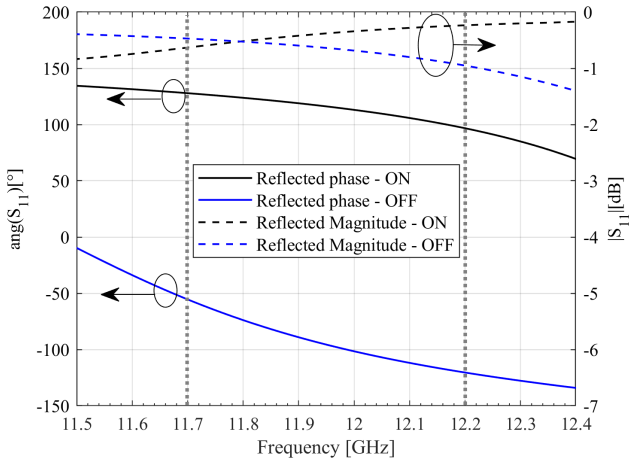

Figure 3.3: Reflected phase and magnitude responses of the Unit cell over frequency for the two possible states of the pin-diode (ON and OFF). The right y-axis displays the S11 magnitude while the left y-axis shows the reflected phase.

3.2.3 Bias-Tee Design

Bias Tee are commonly used for feeding dc into active RF components, such as diodes, and it operates in such a way that the RF performance is not affected by the dc connection point and it avoids the RF signals from damaging the control/bias circuits [69]. A typical circuit is composed

Table 3.1: Dimensions of the Unit Cell Optimized for Low Reflection Loss.

Dimension	**Value**
D_{gap}	0.9 mm
D_{gap2}	0.35 mm
W_1	1.5 mm
W_2	11.05 mm
W_3	15 mm
h_1	30 mil
h_2	20 mil
L_1	0.975 mm
L_1	3.15 mm

of a radial stub attached with a high-impedance quarter-wavelength transmission line, as shown in Fig. 3.4, where W represents the width of the DC bias line, L_{qw} refers to a transmission line with a $\lambda/4$ length. The radial stub defined by the parameters r_L and α, which refers to its

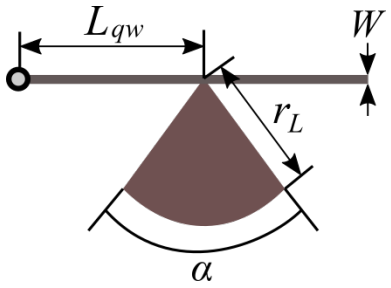

Figure 3.4: RF-Choke/Bias Tee circuit topology formed by the combination of a quarter wavelength transmission line and a radial stub.

external radius and the vertex angle, respectively, is responsible for generating a low impedance at the junction point. This impedance can be derived by considering a radial transmission-line excitation in a ring-shpaped resonator [70], which results in

$$Z_T = j\frac{hZ_0\left(kr_i\right)\cos\left[\theta\left(kr_i\right)-\psi\left(kr_L\right)\right]}{\alpha r_i \sin\left[\psi\left(kr_i\right)-\psi\left(kr_L\right)\right]}, \tag{3.7}$$

where r_i is the width of the joint point, k is the wavenumber, and Z_0 is the characteristic impedance of the transmission line placed over a substrate with height defined by h. In this equation, $\psi(kr)$ and $\theta(kr)$ are defined as

$$\begin{aligned}\theta(kr) &= \arctan\left[N_0(kr)/J_0(kr)\right], \\ \psi(kr) &= \arctan\left[-J_1(kr)/N_1(kr)\right],\end{aligned} \tag{3.8}$$

where N_0 is the Bessel function of second type and order 0, and J_1 refers to the first-order Bessel function of first type.

The quarter-wave transmission line denoted by L_{qw} works as an impedance transformer, in

which its equivalent impedance is defined as

$$Z_{eq} = \frac{Z_0^2}{Z_T}, \tag{3.9}$$

which converts the low-impedance point of the radial stub (ideally $0\,\Omega$) into open-circuit ($\infty\,\Omega$).

The design procedure of the Bias-Tee circuit was carried out as follows: the initial dimensions were obtained by using analytic tools, accounting for Eq. (3.7), (3.8), 3.9. The dimensions were validated using ADS circuit simulation, in which the bias tee was placed in the middle of a 10 mm transmission line, from which the layout was generated and simulated using EM simulation (MoM) with mesh density of 50 cells/λ. Then, the layout of the radial stub and the line parameters were optimized in order to achieve good RF isolation on the bias port, and good RF transmission. The obtained results are shown in Fig. 3.5

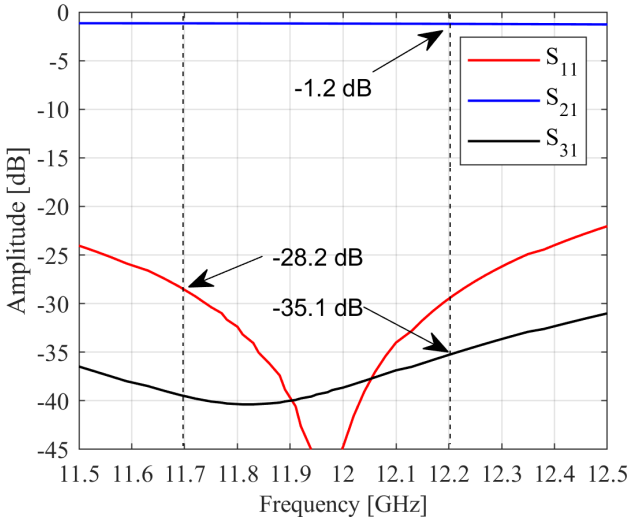

Figure 3.5: S-parameters obtained by the optimized Bias-tee geometry applied to a $50\,\Omega$ TL. Ports 1 and 2 are connected to both ends of a $50\,\Omega$ TL and Port 3 is the port associated with the DC bias point. The optimal dimensions are: $r_i = 6$ mils, $r_L = 2.72$ mm, $\alpha = 70°$, $L_{qw} = 4.25$ mm)

3.3 HORN FEED ANTENNA

3.3.1 Design Constraints

The horn design took into account the compromise between gain, size and HPBW, determined by the RA geometry, which in this case is square shape. In order to estimate the required HPBW, the theoretical RA gain was estimated by using Eq. (2.25), by setting $M = N = n^2$, and $a = b = d$. The required gain value can be obtained from Eq. (3.6), which results into the following relationship:

$$G = \eta_{ap}\frac{4\pi}{\lambda_0^2}n^2d^2 \geq 18.3\,\text{dB}, \tag{3.10}$$

where $d = 0.5975\,\lambda_0$ (from Tab.3.1). The only unknown left is the aperture efficiency η_{ap}, which assume ranging from $15\,\%$ up to $25\,\%$ for small RA antennas operating in the Ku-band [28], [27], [36]. By replacing the lowest value found in literature, that is, $\eta_{ap} = 0.15$ in Eq. (3.10),

$$n \geq \sqrt{\frac{10^{\frac{18.3\,\mathrm{dB}}{10}}}{4\pi.0.5975^2\eta_{ap}}} = 10, \tag{3.11}$$

reulting in a reflector surface of $150\,\mathrm{mm} \times 150\,\mathrm{mm}$. By fixing f/D = 1, and using Eq. (2.27) and Eq. (2.28), and by considering a simplified aperture efficiency defined by $\eta'_{ap} = \eta_{ill}\eta_s$, the optimal q-factor is found to be $q = 10.7$, which is illustrated in Fig. 3.6. From Eq. (2.22) and

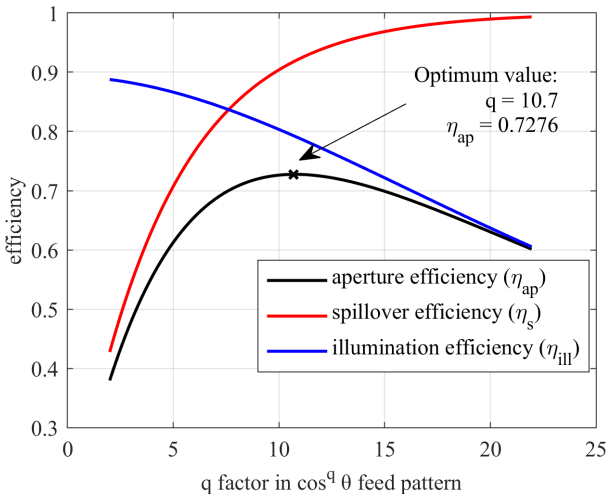

Figure 3.6: Efficiency analysis by considering a circular array of diameter D = 150 mm and fixed f/D ratio of 1.0. The optimal aperture efficiency is achieved when $q = 10.7$.

Fig. 2.5, the required horn antenna gain is $G_h = 16.4\,\mathrm{dB}$. The Horn geometry will be described in the following section, which was designed based on this gain requirement.

3.3.2 Geometry Description

Since the proposed RA is linear polarized, the conventional pyramidal fed with a coaxial $50\,\Omega$ connector was chosen for this project. This antenna was designed with Antenna Toolkit® , in HFSS® . The standard dimension WR-90 was chosen for its design, which has lower and higher cut-off frequencies of 6.557 GHz and 13.114 GHz, respectively, suitable for the frequency range.

For the horn design, the conventional optimal constants were used, $\sigma_a = 1.2593$ and $\sigma_b = 1.0246$. From Eq. (3.10), the required gain is used in order to define the dimensions A and B, which can be obtained by using the equations below [15]:

$$G_h = 0.49\frac{4\pi}{\lambda^2}A.B, \qquad \frac{\sigma_b^2}{\sigma_a^2} = \frac{B(B-b)}{A(A-a)}; \tag{3.12}$$

where a and b are defined by WR-90 standard sizes. The complete geometry is depicted in Fig.

3.7 and its radiation pattern, plotted in E-plane and H-plane, is shown in Fig. 3.8.

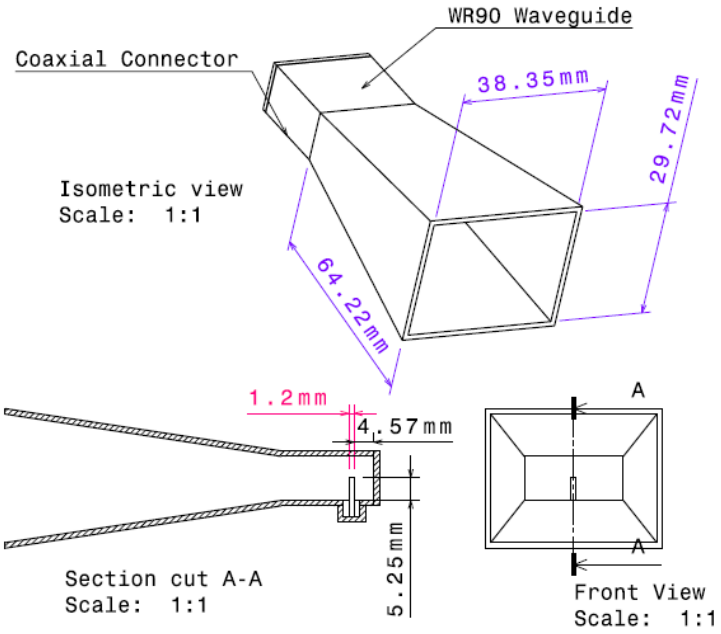

Figure 3.7: Dimensions and geometry of the horn.

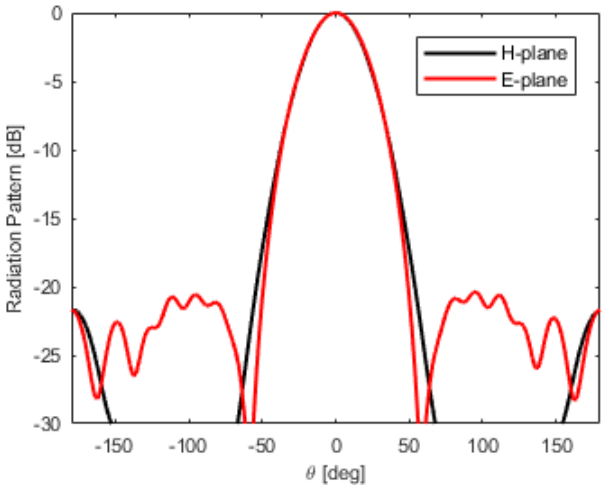

Figure 3.8: Simulated normalized gain plot as function of the elevation angle θ, in both E-plane and H-plane.

After optimizing the conector position and dimensions, it was possible to obtain low reflection loss, as shows Fig. 3.9, probed with a wave-port at the coaxial connector location.

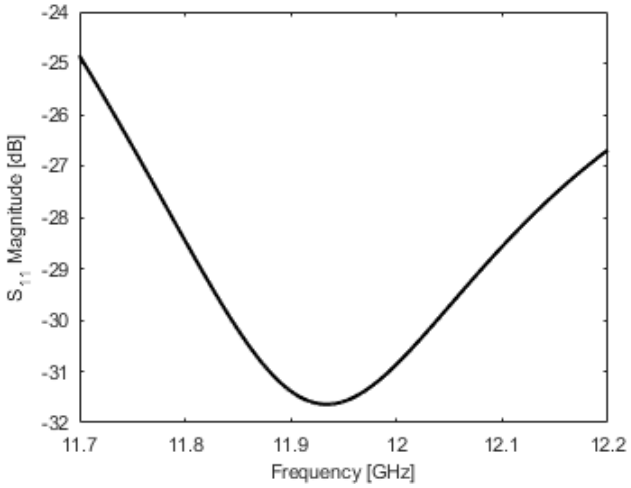

Figure 3.9: Reflection coefficient simulated with a wave port placed in the coaxial connector.

3.4 ARRAY DESIGN

3.4.1 Geometry Description

The first step of the array design is to define the location and height of the feed. In order to further analyze the blockage effects of the feed, the horn antenna was placed centered broadside of the RA. For this design, the f/D ratio is close to 0.8, which was defined previously based on the optimized horn parameters for a high-efficiency design, this results in a distance of $f = 120\,\text{mm}$ from the phase center of the horn antenna and the array. The total array size was defined in order to match the gain requirements set on the link-budget calculations, resulting in a 10×10 square-shaped array. The structure supporting the Horn antenna is constructed with ABS material, which was chosen for its resistance against adverse environmental conditions and due to its lightweight and low-cost characteristics. The antenna assembly is illustrated in Fig. 3.10 and the layout can be found in Appendix VI.

3.4.2 Phase Distribution Matrix Generation

In order to synthesize a single pencil-beam shape radiation pattern to point the radiation power from the LoRa receiver a satellite, located at the position $u_b(\theta_b, \varphi_b)$ in Skyview, Eq. (2.32) can be used. The required phase distribution matrix is illustrated in Fig. 3.12(a), which is applied for the case where $\theta_b = 30°, \varphi_b = 0°$. To implement this phase distribution for the proposed 1-bit unit cell configuration, it is necessary to discretize it into two states. Initially, it can be carried out by

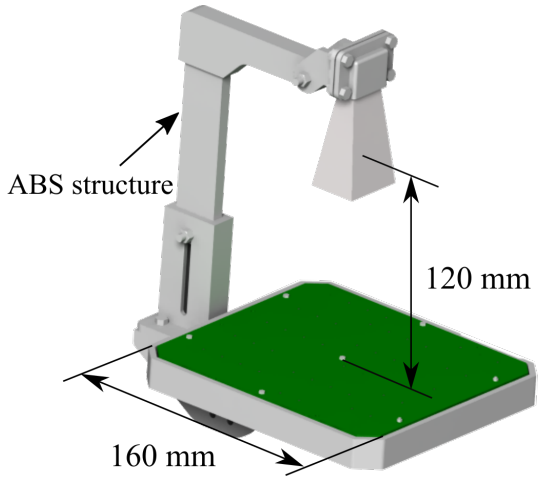

Figure 3.10: Illustration of the proposed RA assembly.

considering a threshold in the middle of the continuous range,

$$\begin{aligned} \Phi_{R(\text{bin})} &= 0^\circ + \Phi_{\text{ref}} \\ \text{if } \Phi_R &\leq 180^\circ, \\ \Phi_{R(\text{bin})} &= 180^\circ + \Phi_{\text{ref}} \\ \text{if } \Phi_R &\geq 180^\circ. \end{aligned} \tag{3.13}$$

It is worth mentioning that the reference phase Φ_{ref} used in Eq. (3.13) can assume any values ranging from -180 to 180°. For that reason, Fig. 3.12(b) illustrates the diodes' states instead of the reflected phase. In fact, different threshold levels were investigated previously by [71] and [43], but for this specific case, similar results were achieved for different reference phases.

By using Eqs. 2.30 and 2.31, the radiation fields generated from the phase distribution matrices shown in Fig. 3.12 were computed. The reference phase used in this case was $\Phi_{\text{ref}} = 0^\circ$. From this figure, it is possible to observe that a high side-lobe as high as -9.3 dB appears at $+13^\circ$ for the discrete phase distribution, which indicates that the discrete phase distribution introduced phase errors causing gain reduction and, consequently, leading to higher side-lobe levels.

3.4.3 Modeling and FEBI Simulation

Although the radiation pattern shown in Fig. 3.12 gives a good prediction for the main-lobe, it cannot predict accuretelly the side-lobe characteristics since it does not include side effects such as specular reflection, edge diffraction, coupling between adjacent elements, among others, which can only be accomplished by using full-wave electromagnetic simulation [2]. With the purpose of verifying the radiation pattern characteristics using a full-wave solver, the FEBI method was used, since the computational resources were limited. Fig. 3.13 describes the model used for this

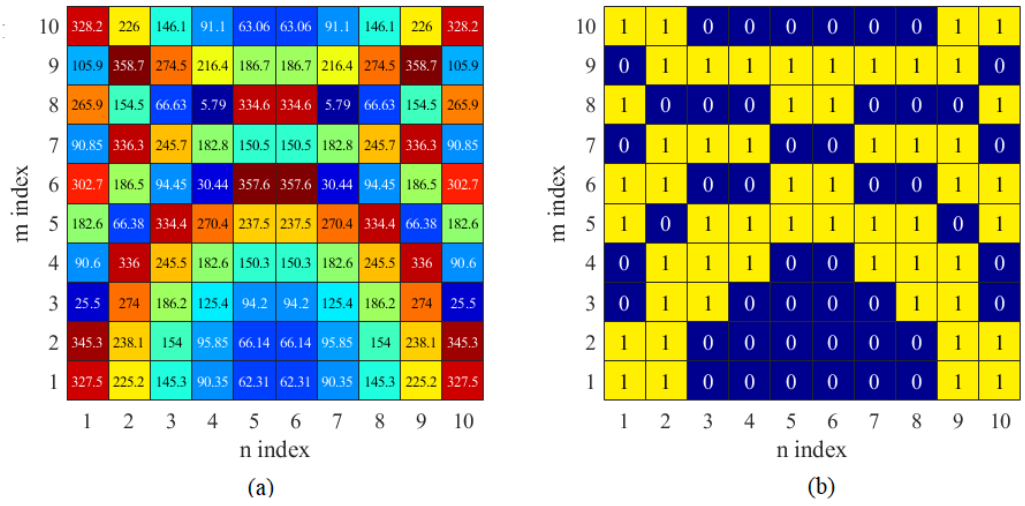

Figure 3.11: Required continuous phase distribution matrix to generate a pencil-beam pointed towards $\theta_b = 30°$, $\varphi_b = 0°$ (a). Discretization states of the diodes, where "1" denotes the forward bias state, and "0", refers to the reverse bias state (b).

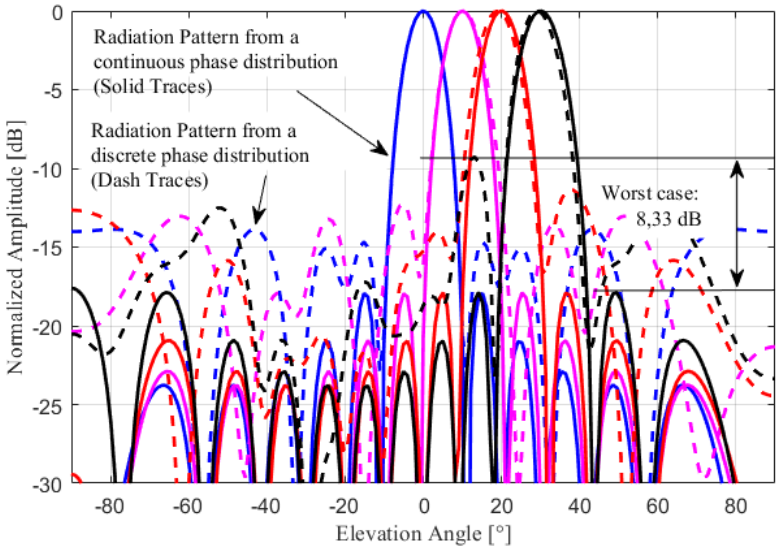

Figure 3.12: Comparison between the ideal radiation pattern due to a binary phase distribution (solid traces) and of a continuous phase distribution (dash traces) from 0° to 30°.

simulation. Note that feed support was not modeled here to optimize simulation time.

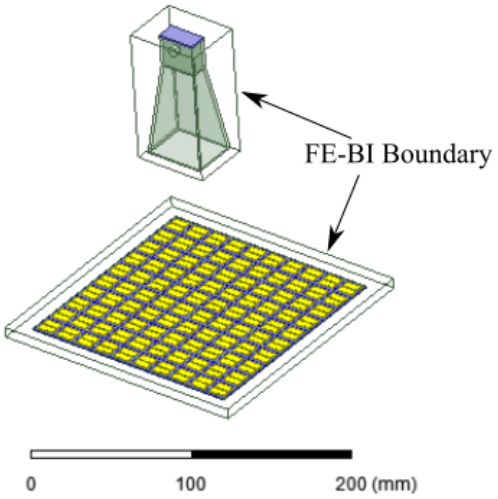

Figure 3.13: Setup used in Ansys HFSS® to validate the 10×10 antenna through hybrid FEM simulation.

For this simulation setup, a Driven Modal solution, with $1\,\%$ Gain error was configured. The maximum gain obtained was $19.2\,\text{dB}$, at $11.95\,\text{GHz}$, which led to a $18.54\,\%$ efficiency, based on the definition

$$\eta_{RA} = \frac{G}{4\pi A/\lambda^2}, \tag{3.14}$$

where A refers to the area of the planar surface. The result was verified for the E-plane ($\phi = 0°$) for three scanning angles, as shown in Fig. 3.14.

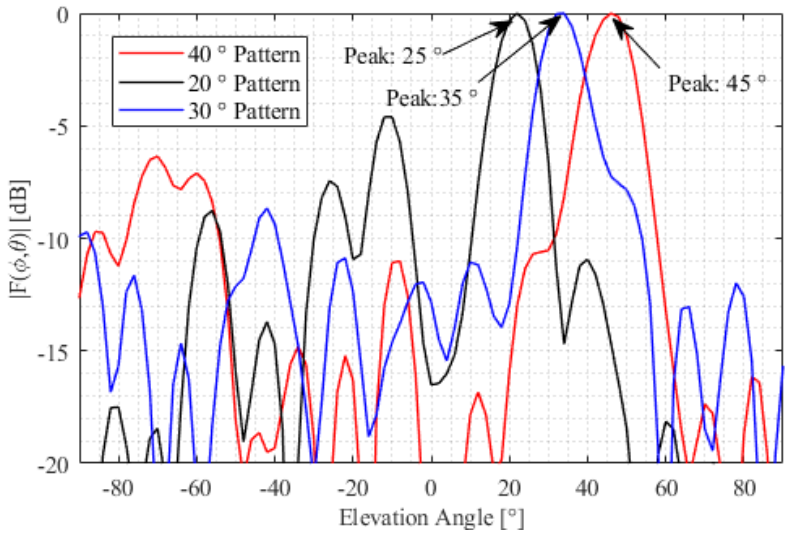

Figure 3.14: Gain of the antenna plotted as function of the elevation angle, observed from $-90\,°$to $90\,°$ for different directions ($\theta_b = 20°$ to $\theta_b = 40°$).

In this figure, it is possible to observe that a $40°$ beam scanning capability was obtained. It is also noticeable that the side-lobe level is even more pronounced when using full-wave analysis,

which occurs in the worst case for $\theta_b = 20°$, differently from the analytic solution, in which the worst case occurred at $\theta_b = 30°$.

3.4.4 Pattern Optimization

To solve the problem of high-level side-lobes observed by EM simulations or analytical calculations observed in the previous section, two optimization methods were studied for the worst case ($\theta_b = 30°$). The first method to be used is Convex optimization (CVO). This method was implemented in the CVX framework with the MOSEK solver in Matlab. The problem is described in section 2.5.1, which consists of an iterative solution based on the Taylor first-order series expansion. For this problem, several values of k and δ were tested, but $k = 10$ and $\delta \leq 0.16$ lead to better results. The script used for this optimization is described in Appendix II.

The second method studied is the PSO problem, which is described in section 2.5.2. In this case, the fitness/objective function is the maximum side-lobe level, which is achieved by computing the array factor over the secondary lobe region. The conventional PSO formulation was used in this case, with $S = 10$, $c_1 = c_2 = 1.5$, $w = 0.75$ (initial value) and 100 iterations. Fig. 3.15 illustrates the comparison between both methods for the E-plane ($\phi_b = 0°$).

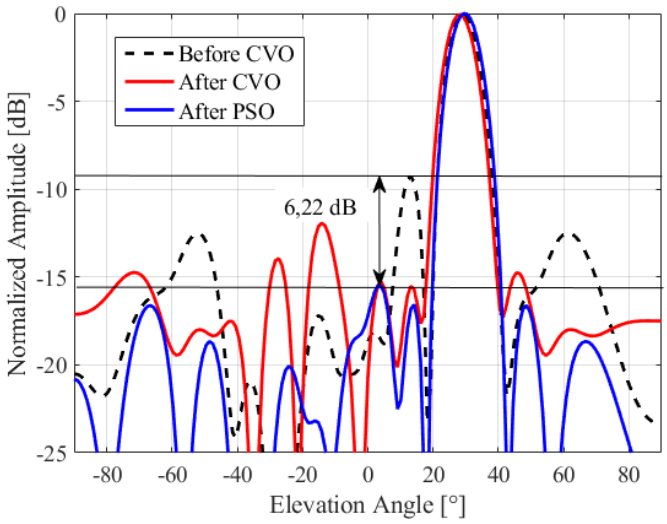

Figure 3.15: Comparison of the simulated radiation pattern ($\phi = 0°$) between PSO and CVO results with the initial radiation pattern obtained from the Ray tracing method. The beamwidth was fixed during sidelobe minimization.

From Fig. 3.15, it can be seen that PSO better in terms of side-lobe suppression if compared with CVO, reducing side-lobe levels up to 6.2 dB, but this is not true in terms of time-efficiency. For this problem, using a dual core Intel® CPU i5-5200U operating at 2.2GHz and with a 16GB RAM installed, it was possible to achieve 10:31 min convergence time for the PSO with 100 iterations, while for the CVO, it took 40 seconds for 10 iterations, which results in 36% better efficiency than PSO. It is worth mentioning that both methods were optimized using continuous variables, even though the cost function of the PSO method was calculated using discrete phase distribution, which was not the case for the CVO approach, where the optimization was carried

out using a continuous phase distribution, turning the problem to be more complex in terms of computational load. It is worth mentioning that computational performance can be improved if a full-discrete approach and formulation are utilized instead.

The full radiation pattern and its phase distribution diagram are also plotted in the sin space in Fig. 3.16, from where it is possible to observe that different reflection phase distributions can lead to the same radiation pattern. It is also noticeable that the CVO algorithm resulted in a non-symmetric phase distribution matrix and higher side-lobe levels if compared with the PSO result.

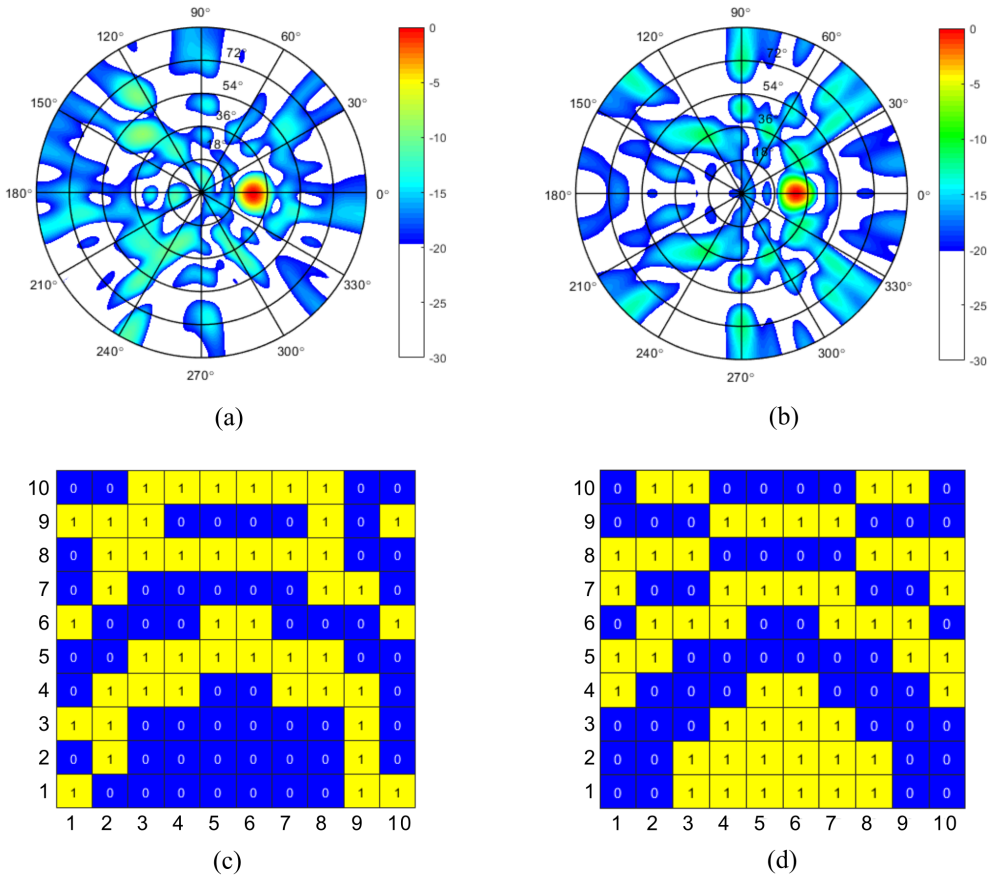

Figure 3.16: polar plot of the radiation pattern resulted from CVO (a). Radiation pattern generated from PSO (b). Phase-distribution matrix generated from CVO mapped in terms of diodes' states (c). Phase-distribution matrix generated from PSO also mapped in terms of diodes' states (d)

3.5 CONTROL CIRCUIT

In order to control the beamwidth, or use different beamforming techniques, as well as to change the scan angle, the logic levels of the diodes must be configurable, which needs individual logic drivers for each diode separately. It is also worth mentioning that accurate control of the current can optimize and ensure higher antenna performance even under different environmental

conditions since the biasing conditions could change the RF characteristics of the diode with temperature variation, or due to process variations, which may cause different behavior in each diode.

It is common to find RA driven by shift registers such as the IC 74HC164, which converts serial data into parallel data lines, thus allowing for individual control with reduced control lines [28]. It is also very common to use GPIOs from FPGA or micro-controllers associated with high precision resistors[36]. If accurate control is needed, these alternatives requires additional circuitry to guarantee the current levels, which can be achieved by using a constant current driver with BJT transistors, as shown in Fig. 3.17. In these designs, the current is trimmed by the $68\,\Omega$ resistor.

Even though this circuits adds protection for both PIN diodes, and logic ICs, it is not so effective for accurate current control, since it relies on the stable characteristics of the transistors, which have intrinsic tolerances due to fabrication process and even tough this solution meets one design requirement, it results into a bulky control circuit, due to the large number of discrete components.

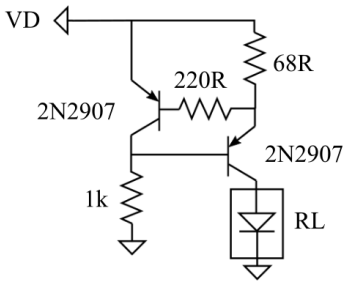

Figure 3.17: Current limiter circuit using PNP transistors.

This work proposes a current control circuit based on the RGB LED driver LP55231. This IC implements a constant current individual control for 12 outputs, in addition to other features such as, ON/OFF control, PWM, and high current capability ($25.5\,$mA), configurable with I^2C, which makes this IC suitable to many applications for its versatility. To program and control the phase distribution, an 8-bit microcontroller was used. The control circuit is shown in Fig. 3.18.

In order to supply enough power to the RA with high efficiency, a switching power supply followed by a linear regulator was also designed and included in the Control Circuit Board. The linear regulator works so as to provide a cleaner power supply to the board. The power supply needs to supply, in the worst case 2A, since each diode consumes approximately $10\,$mA. For that reason, the AP62250Z6-7 IC was chosen as the switching PSU, as it provides up to 2.5A current with 90% efficiency. The high switching frequency of this IC also contributes to a reduced-size solution. For the linear regulator, the AZ2185D IC was chosen for its current capability, low

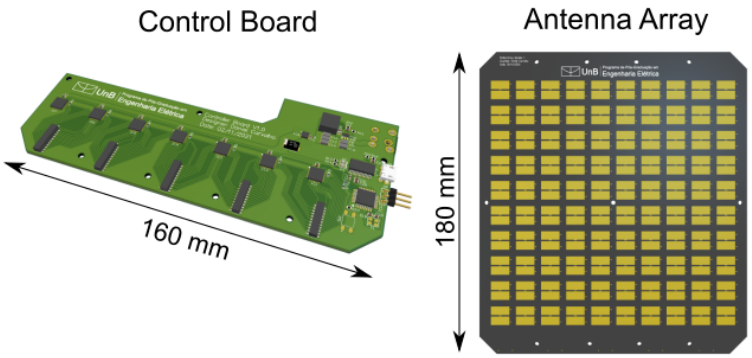

Figure 3.18: Control board integrated with the microcontroller and antenna array PCBs.

quiescent current, PSRR, and availability. The complete schematic is shown in Appendix IV, including the control circuit. The board Layout can also be found in Appendix VI.

For initial tests, a LED matrix was designed for debug purposes, with which was possible to identify the biasing logic level before connecting to the antenna. This board assembly is shown in Fig. 3.19. The first algorithm tested was using a conventional beam focused in an arbitrary direction, so all spatial coefficients were generated internally in the microcontroller using the array factor calculation in order to generate the coefficients.

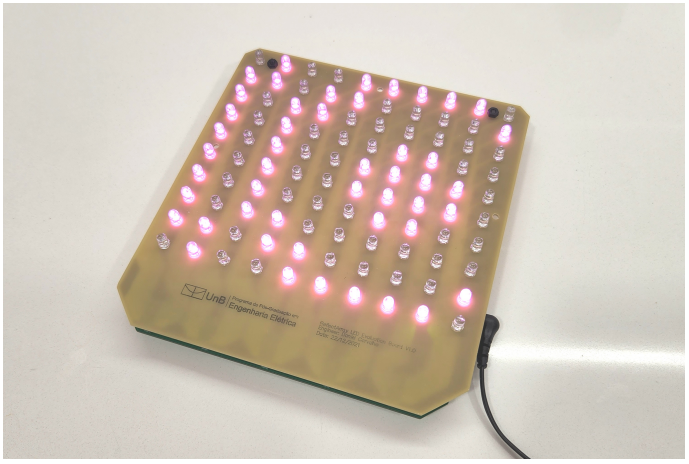

Figure 3.19: LED Board designed for the phase distribution matrix mapping.

4 DESIGN OF THE RF BOARD

A typical RF-Frontend of a transceiver operating at the Ku-band is often composed of a diplexer, followed by a two-stage LNA and a bandpass filter, which are placed before the mixer using the so-called Heterodyne receiver architecture [72], [73], [74]. The use of Heterodyne topology allows for a higher "Q-factor" band-pass filters, capable of filtering out interferers and adjacent channels, and, even though this configuration suffers from an image problem, a high-attenuation filter placed before the mixer minimizes this effect.[75].

Since LoRa® communication protocol is halfduplex [76], that is, the transmission and reception does not occur simultaneously, the diplexer was removed for the proposed topology, so that the the losses before the LNA is minimized, leading to a lower noise figure. For the transmitter path, a low-pass filter is also commonly used before mixer to filter out the harmonics inherent from non-linearity of power amplifiers (PA) [77], specially when dealing with LoRa transmitters, which generally employ High-efficiency switching amplifiers, generating undesired harmonics [78], [79]. The proposed Ku-band transceiver topology is shown in Fig. 4.1

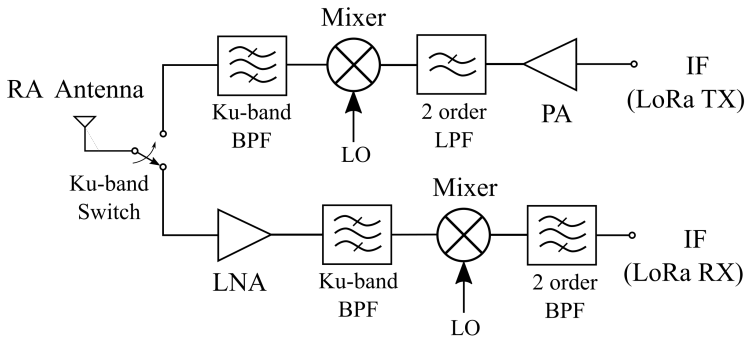

Figure 4.1: Simplified block diagram of the proposed Ku-band receiver architecture.

In Fig. 4.1, the LNA block consists of a single transistor-based LNA, in contrast with cascade topologies proposed by [72] and [73], given that the FSL is lower on this application, due to the low-orbit operation. A single frequency (LO) operating at 11.035GHz was preferred in this case, so the frequency hoping is made in the IF domain (902MHz - 928MHz) by means of the SX1262 LoRa® transceiver, which was chosen for its flexibility, package size and output power.

In order to simplify the transceiver design, the same mixer was used for both up-converter and down-converter paths. The mixer part number choice (MAMX-011021) based on linearity, maximum input power at IF port and availability. Tab.4.1 lists some alternate mixers that are suitable for this project.

Table 4.1: List of Ku-band Up/Down conversion mixers.

Part Number	Conversion Loss	LO/IF Isolation	Input P1dB
MDB-24H+	9 dB	36 dB	10 dBm
HMC412BMS8GE	8 dB	29 dB	10 dBm
MAMX-011021	**8** dB	30 dB	15 dBm
HMC220B	9 dB	38 dB	11 dBm

4.0.1 Ku-band Band Pass filter (BPF)

Ku-band Bandpass filters were included in this project in order to filter out the Image component before the down-converter mixer, which falls in the X-band ($9.87\,\text{GHz} - 10.37\,\text{GHz}$). In order to do so, the filter design must achieve a good out-band rejection. On the up-converter side, a similar BPF is chosen in order to filter-out mixing spurs and harmonics coming from IF signals. It happens that, in the worst-case scenario, the mixing spurs and IF harmonics fall at $650\,\text{MHz}$ apart from the desired frequency band ($11.7\,\text{GHz} - 12.2\,\text{GHz}$). With these constraints, and by considering a $30\,\text{dB}$ out-band attenuation, a band-pass Chebyshev prototype was implemented using an edge-coupled topology, since it fits with the bandwidth requirements and permits attenuation level control. A 0.1 dB ripple was considered in this case. [80], [69].

The design process was carried out as follows. At first, the Chebyshev low-pass prototype was calculated based on the requirements given above, from which was possible to define the order of the filter by the following relationship [69]:

$$n \geq \frac{\cosh^{-1}\sqrt{\frac{10^{0.1L_{as}}-1}{10^{0.1L_{ar}}-1}}}{\cosh\,{\Omega_s}^{-1}}, \tag{4.1}$$

where L_{as} indicates the stopband attenuation, while L_{ar} indicates the passband ripple. Ω_s refers to the normalized cutoff frequency, typically 2 for BPF. After defining the order of the filter and the low-pass prototype, the odd and even impedances were obtained after applying the J-inverters and finding the line's admittance, from which the line dimensions were obtained. The analytic calculation is described in detail by [69] and its implementation can be found in Appendix III. The results were first analyzed in terms of circuit simulation and later, the dimensions were optimized using MoM simulation with the software PathWave®ADS and later validated with FEM simulation in Ansys® HFSS.

The comparison between the ideal simulation and the FEM simulation result is shown in Fig. 4.2. In this figure, it is possible to observe a noticeable increase in the insertion loss and wider bandwidth. It is worth mentioning that a wider bandwidth was necessary in order to improve the in-band ripple, which is $\pm 1\,\text{dB}$ in this case. The higher insertion loss and ripple are mainly due to the substrate losses and conductor loss, included in the simulation.

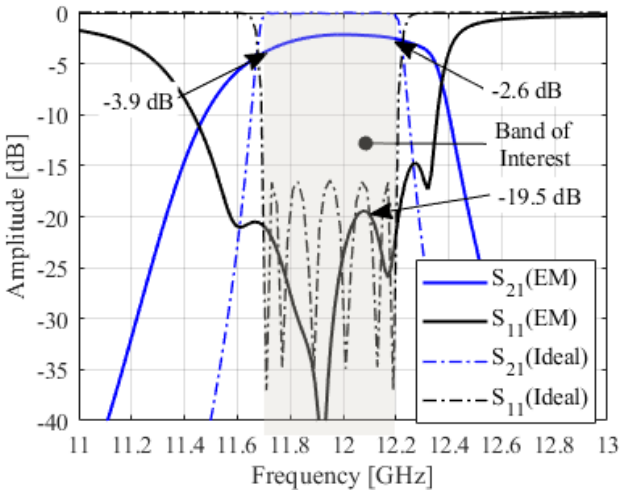

Figure 4.2: Comparison between the ideal filter response, obtained by analytic calculation with the optimum EM simulation results. Solid traces indicate EM simulation results while dash traces illustrate the ideal filter response.

4.0.2 Low Noise Amplifier (LNA)

The proposed LNA design is based on the FET transistor CE3512K2, which was chosen based on the compromise between cost, noise figure and gain. This part is suitable for first-stage amplification on VSAT and LNBs applications operating in the Ku-band [81]. The biasing operating conditions are described in Tab. 4.2, which were defined so that the transistor operates at the minimum noise figure. From the polarization defined by Tab. 4.2, the stability circles, noise

Table 4.2: LNA Bias Operating Condition

Parameter	Value
Gate Voltage (VG)	-0.5 V
Drain Voltage (VD)	2.0 V
Drain Current (ID)	10 mA

figure and gain were obtained using smith chart analysis. The desired requirements for the LNA is the minimum noise figure (< 1.0 dB) and 12 dB gain. The LNA was designed considering the best compromise between the noise figure and gain. Fig. 4.3 illustrates the circles obtained through the ADS tool, which was used to define the input and output impedances of the LNA. In this figure, it is observed that the LNA has conditional stability since the stability circle (stable region is the inner region) intersects the Smith chart at some point. It is also observed that it is not possible to perform the conjugate matching (For the Maximum Gain), since the optimal conjugated impedance is outside the Smith chart for the analyzed frequency (11.95 GHz). From these considerations, a few simulations were performed in order to observe the ideal parameters for the first stage, by considering the minimal noise figure. The optimal impedances (source and

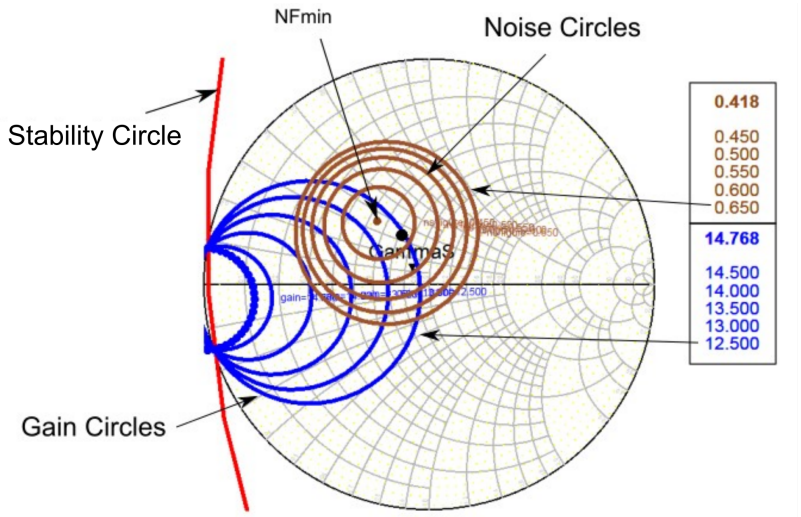

Figure 4.3: Stability circles (Zs), noise and gain (GA). Each circle has its associated value in the table on the right in ascending order, which are in given in dB. It is important to note that the NFmin for the 11.95 GHz frequency is 0.418 dB.

load) for the lowest noise figure were found to be:

$$\begin{aligned} Z_S &= 27.2 + j17.6\Omega, \\ Z_L &= 29.7 + j6.7\Omega. \end{aligned} \tag{4.2}$$

In order to these impedances to the transistor, microstrip circuits were used, such as stubs and 50 Ω Transmission-lines). The design process started by designing the bias-tee circuit. A circuit similar to the one used in the RA was designed, but with a cascade configuration, which provides higher isolation and higher bandwidth [69]. This topology is illustrated by Fig. 4.4. The results are highlighted by Fig. 4.5.

After designing the LNA bias network, the optimal impedances were obtained by first validating them with ideal components (stubs and transmission lines), followed by EM simulations, which were implemented using MoM in PathWave®ADS, from which it was possible to adjust a few dimensions in order to obtain an optimal LNA response. Fig. 4.6 shows the top and 3D views of the final LNA geometry (dimensions are listed in Tab.4.4). The EM simulation results are plotted in Fig. 4.7. It is worth mentioning that because the optimal impedance is not 50Ω, it is expected to observe an impedance mismatch at the LNA input, which is noticeable in Fig. 4.7. The final circuit is shown in Appendix V and layout prints are shown in Appendix VI.

4.0.3 LoRa transceiver Impedance Matching

In order to provide good harmonic filtering for the switching power amplifier, avoiding radiated emissions, a good suppression low pass filter must be used. Indeed, emission suppression can be also improved by either changing the duty cycle of the DAC or by using shielded RF traces [82]. Since the LoRa®frequency is lower (at around $915\,$MHz), it is more convenient to

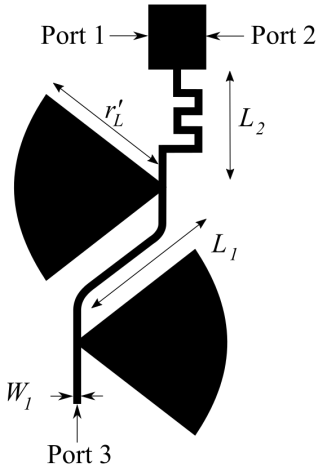

Figure 4.4: Bias-tee/RF Choke designed for the LNA polarization network. In this figure, $L_1 = 3,14\,\text{mm}$, $L_2 = 3,55\,\text{mm}$, $w_1 = 5\,\text{mil}$ and $r'_L = 2.45\,\text{mm}$.

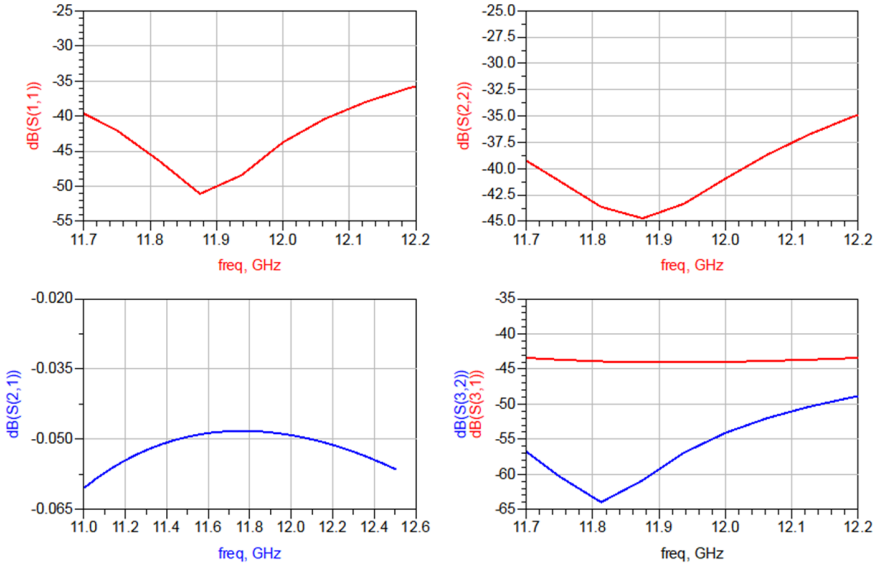

Figure 4.5: S-parameters obtained from the optimal RF Choke structure illustrated by Fig. 4.4.

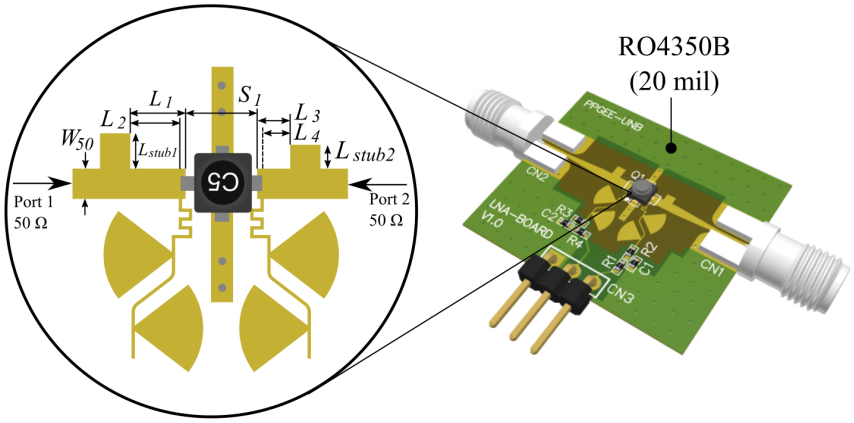

Figure 4.6: LNA Final geometry description and illustration of the test board designed for validation and for measurement purposes.

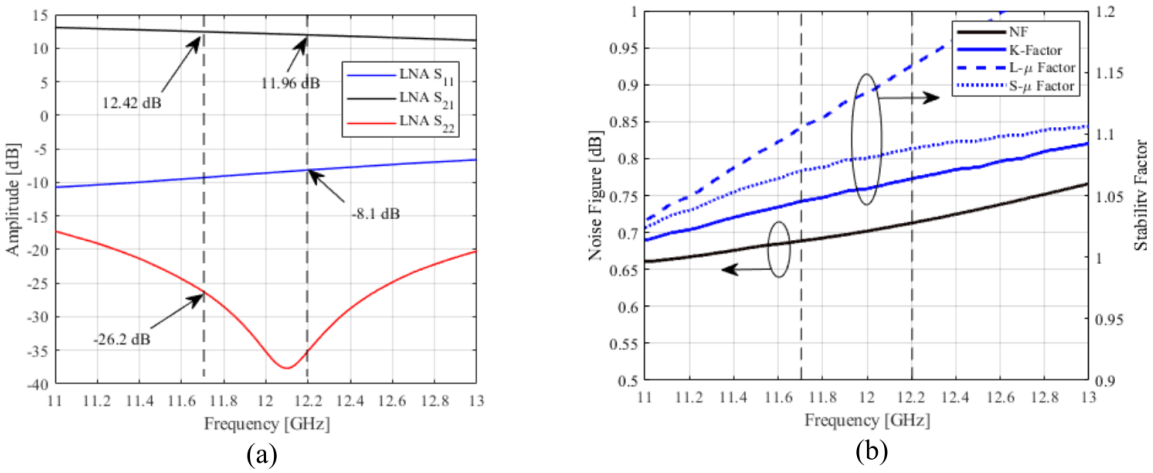

Figure 4.7: EM simulation results of the optimized LNA topology. S-parameters are shown in (a). Stability factors and noise figure are plotted in (b).

Table 4.3: LNA's Matching Circuit Final Dimensions

Parameter	Value
W_{50}	1.10 mm
L_1	2.01 mm
L_2	1.82 mm
L_3	1.20 mm
L_4	1.02 mm
L_{stub1}	1.28 mm
L_{stub2}	0.87 mm
S_1	2.60 mm

use discrete-type network circuits, instead of microstrip circuits, which not only reduces the solution size but also ensures good out band suppression for high-order modes of propagation, which is not the case for microstrip circuits [59]. The proposed topology is highlighted in Fig. 4.8. This circuit was previously proposed by [83] and it consists of a notch filter followed by a Pi-type low pass filter.

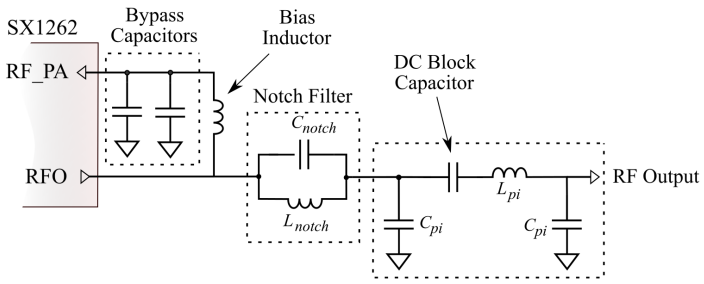

Figure 4.8: Matching network used for the TX output matching of the SX1262 transceiver.

The notch filter is used to attenuate as much as possible the second harmonic of the RF output, as it is the highest level component present at RFO, and to match the output impedance to the optimum value. The initial values of C_{notch} and L_{notch} were defined based on the cutoff frequency, considering a reasonable output power and a good power efficiency, leading to $Z_{out} = 13.5 + j7.6\Omega$ [84]. The low pass filter composed by C_{pi} and L_{pi} filter-out the remaining harmonics and its values are defined by

$$L_{pi} = \frac{50}{2\pi f} \text{ and } C_{pi} = \frac{0.95}{50 \times 2\pi f}. \tag{4.3}$$

In Fig. 4.8, L_{notch}, C_{notch}, C_{pi} and L_{pi} were first calculated analytically and later were optimized with both hybrid simulations (using SNP models), and by EM simulation (MoM) so that the optimal matching performance was achieved, which resulted in the following configuration: $L_{notch} = 400\,\text{pH}$, $C_{notch} = 6\,\text{pF}$, $C_{pi} = 3.3\,\text{pF}$ and $L_{pi} = 8.7\,\text{nH}$. Fig. VII.7 illustrates

the S-parameter response of the final configuration. The final circuit was implemented using an STM32L0 microcontroller, as shown in Fig. 4.10.

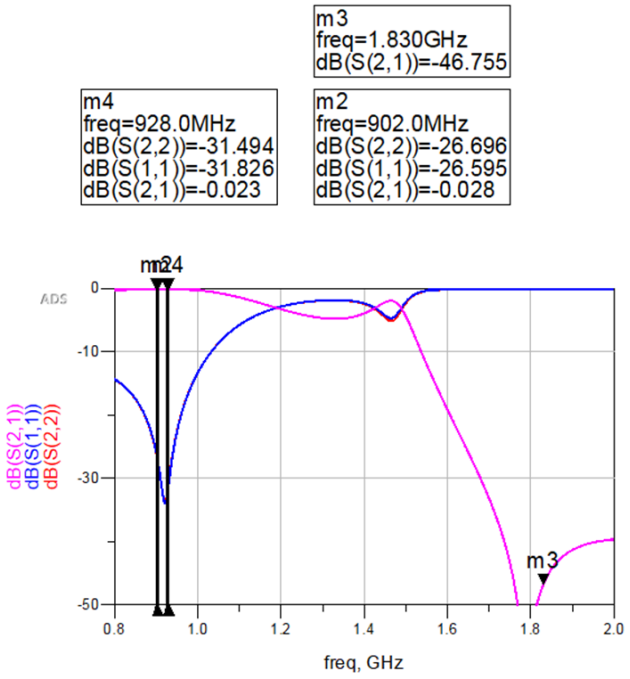

Figure 4.9: S-Parameters resulting from the simulation of the TX-path impedance network.

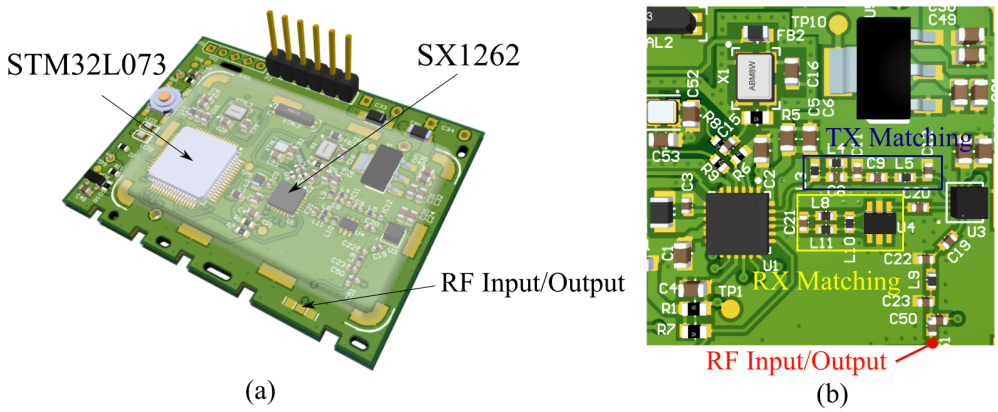

Figure 4.10: Board designed in order to validate SX1262 impedance matching and receiver performance.

Power measurements of the board shown in Fig. 4.10 were taken using the N9340b spectrum analyzer, where the bandwidth was set to 300kHz, with 50 dB attenuation. The measurement was made using CW mode at the center frequency (915 MHz), from which was possible to obtain 18.5 dBm, as highlighted in Fig. VII.7.

In order to match the RF inputs of the SX1262 transceiver, a different technique was used. Since it consists of a differential input, a differential to single-ended conversion is also needed. This process can be implemented by two options, the first alternative is based on the use of passive elements both for impedance matching and for common-to-differential mode conversion as shown

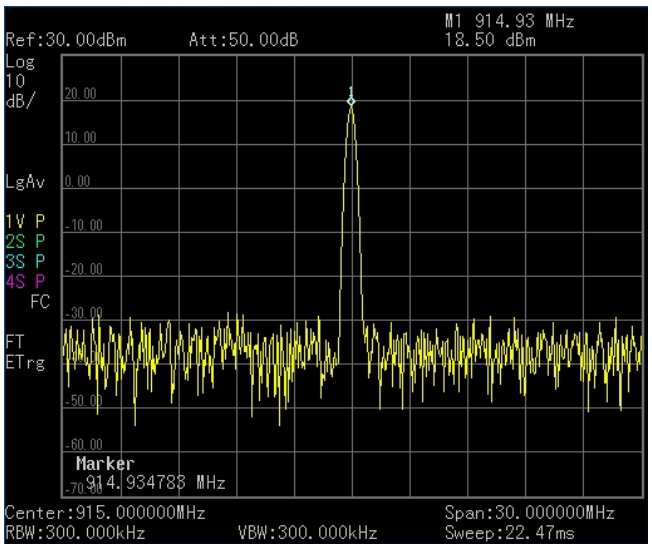

Figure 4.11: RF Power measured at the RF Input/Output connector at 915MHz (18.5 dBm).

in Fig. 4.12a, while the second alternative uses a discrete "balun" and a separate matching circuit (Fig. 4.12b).

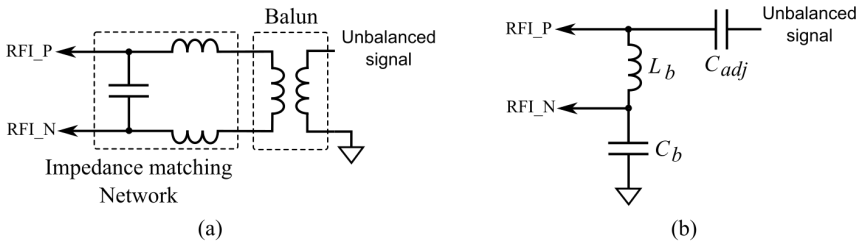

Figure 4.12: Comparison between two different common-to-differential mode conversion: by using balun (a), and by using discrete components (b).

The main drawback of the first approach lies in the fact that it introduces a small phase difference between the negative and positive signals, especially if a finite resistance is considered between the RF inputs [83], which could lead to signal degradation. For that reason, the second approach was preferred to be used in this case, which is based on the 0900BL15C050 balun. This design was carried out as follows: first, the optimal impedance was obtained by [84] and the single-ended matching network was determined. The conversion to differential was made according to [85], leading to the circuit described in Fig. 4.13.

The results are highlighted in Fig. 4.14, from which is possible to observe that both insertion loss (IL) and return loss (RL) achieved good values. The transient simulation in Fig. 4.14b illustrates the differences between the negative signal and positive signals, where a small phase difference of around 1° and an amplitude difference of 2 dB are observed, which is within the tolerances provided by the 0900BL15C050 data-sheet [86]. The receiver performance was evaluated with the board shown in Fig. 4.10, which was configured to receive LoRaWAN packages transmitted base station located as far as 5 km. The test message was QIYK1waAAQACy9UU2Pn20b8Sl+R808c=.

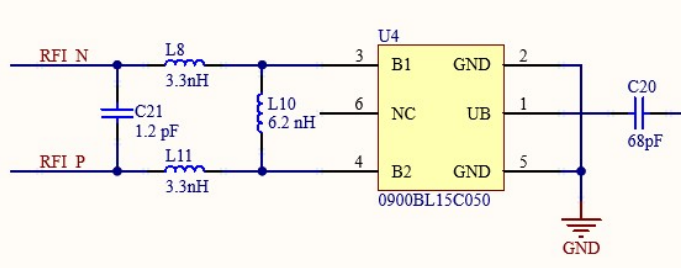

Figure 4.13: Optimum RX Matching network designed for the SX1262 inputs.

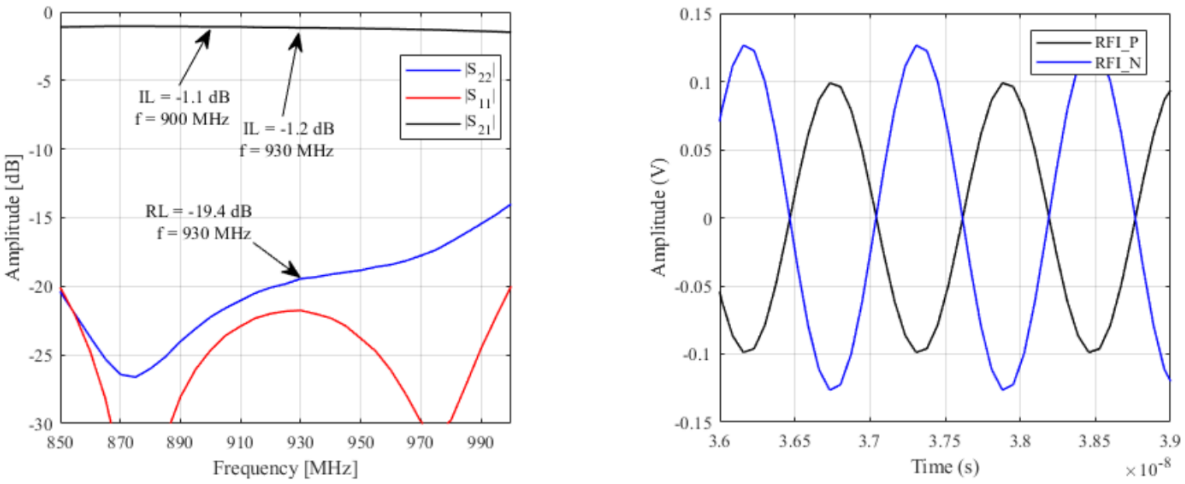

(a) (b)

Figure 4.14: SX1262 RF inputs S-parameters response (a), and steady-state transient response, illustrating the I/Q imbalance (b).

The modulation configuration is SF $= 10$, BW $= 125\,kHz$, CR $= 4/5$. The result is shown in Tab. 4.4. The layout of the complete board can be found in Appendix VI.

Table 4.4: LoRa Packages received by SX1262

Time	Received Message	RSSI	SNR
05:02:54	QIYK1waAAQACy9UU2Pn20b8Sl+R808c=	-111	-8
05:03:42	QIYK1waAAQACy9UU2Pn20b8Sl+R808c=	-114	-8
05:08:25	QIYK1waAAQACy9UU2Pn20b8Sl+R808c=	-113	-8
05:09:32	QIYK1waAAQACy9UU2Pn20b8Sl+R808c=	-112	-9
05:09:53	QIYK1waAAQACy9UU2Pn20b8Sl+R808c=	-109	-9

4.1 UHF PIFA ANTENNA DESIGN

In order to validate the receiver performance as well as to test and verify the communication with the base station, as part of the firmware development, but with a low-cost solution, a small Planar Interved-F Antenna (PIFA) UHF antenna was also designed. This topology was chosen due to its simplicity in construction and the reasonable gain in the used frequency range (UHF). It was designed in a separate board, which is connected vertically to the RF Input/Output connection of the SX1262 board, as shown in Fig. 4.15.

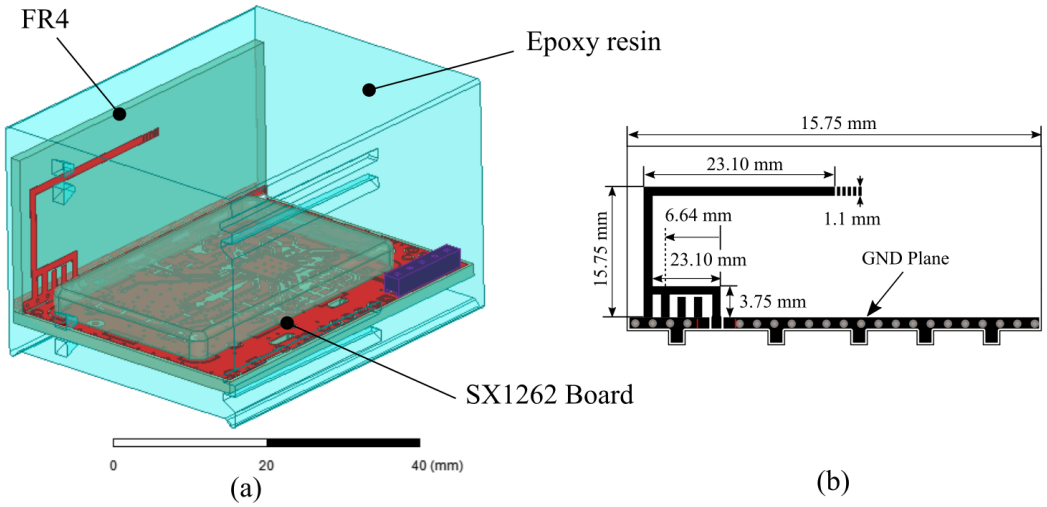

Figure 4.15: PIFA antenna geometry designed for checking LoRa communication.

This antenna was designed to have the size of $\lambda/4$, for the center of the Brazilian frequency band for LoRa, which is 921.5 MHz, but as it is immersed in a resin, as per project requisites, its size was shortened, as a cause of the λ reduction, leading to lower efficiency. This antenna was first designed in HFSS and optimized in a vacuum medium, without resin, and achieved 1.35 dB gain. After optimizing the antenna dimensions in order to adjust the resonant frequency, the final gain was -3.3 dB. The final results are shown in Figs. 4.16 and 4.17.

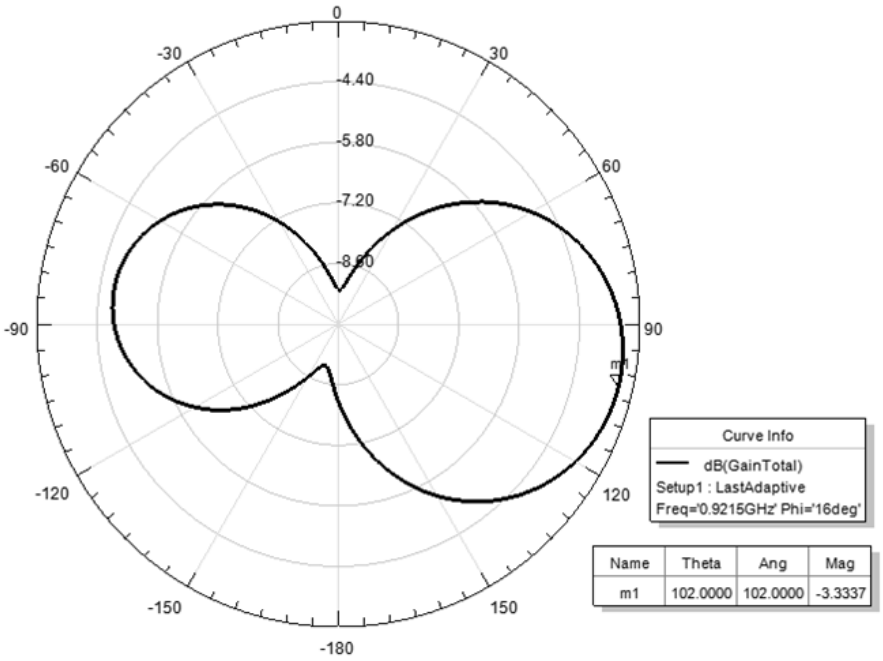

Figure 4.16: Gain plot of the maximum gain plane, that is $\theta = 102°$ and $\phi = 16°$

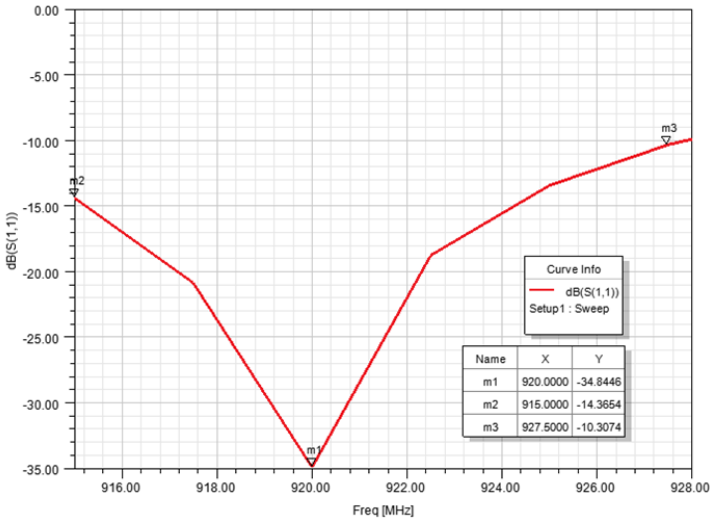

Figure 4.17: Reflection Coefficient of the PIFA Antenna illustrated in Fig. 4.15

5 CONCLUSION AND FUTURE WORKS

5.1 CONCLUSION

The proposed system composed of a RA, Downconverter, and LoRa transceiver opens new possibilities for data exchange applications using not only LoRa but any other IoT protocol operating at the UHF ISM band. The proposed system is suitable for high distances data transmission in medium-power consumption end devices.

A 10×10 RA was designed, validated through simulations, and fabricated. The electromagnetic simulation performance achieved 19.2 dB gain, and $18.54\,\%$ efficiency. The beam scanning capability was simulated and validated up to $30\,^{\circ}$ shift. The gain and efficiency obtained with the proposed unit cell indicate an improvement to the previous works by using two diodes in parallel. Among the array synthesis and radiation optimization, PSO algorithm obtained the best sidelobe suppression, resulting in a -15.4 dB sidelobe level, which can be considered a good value for the small antenna size.

The compact design of the control circuit allows for portable applications, as well as for lightweight satellite applications since its power consumption was lowered by using a switching power supply. The control circuit was validated with the LED board, from which was possible to observe the polarization states of each diode.

The proposed Ku-band receiver topology was validated through simulation and measurements. The BPF-RX filter achieved good agreement between ideal simulation and EM simulations, except for a little degradation in the insertion loss, which would affect the receiver noise figure, although it is placed after the LNA, which minimizes its effect. Performance-wise, the measured LNA gain and noise figures led to acceptable results, but it is possible to observe that degradation in the return loss is noticeable in measurements, which may be due to differences between the calibration planes and position of the LNA transistor since it was soldered manually.

The LoRa®receiver used for the IF stage (SX1262) was able to receive LoRa packets using a prototype integrated with an STM32-based microcontroller. The measured output power was in great agreement with the expected value, if tolerance of 2 dB is considered.

5.2 FUTURE WORK

For future works, it is desirable to include blockage effects on the RA optimization algorithm and integrate it with a full wave solver so that the measurement performance of the array matches accurately with the simulation results. Moreover, it is also suggested a dual-band design, for both RA and receiver chain, operating not only at $11.7 - 12.2$ GHz but also at $14.0 - 14.5$ GHz, so that

the RA can meet the regulatory requirements used for up-link Ku-band transmission.

BIBLIOGRAFIC REFERENCES

1 HUH, J.-H.; KIM, D.-H.; KIM, J.-D. Proposal of seamless communication method in shadow area using lorawan. *J. Commun.*, v. 12, n. 10, p. 585–589, 2017.

2 HUANG, J.; ENCINAR, J. A. *Reflectarray antennas*. [S.l.]: John Wiley & Sons, 2007.

3 MIRAZ, M. H.; ALI, M.; EXCELL, P. S.; PICKING, R. A review on internet of things (iot), internet of everything (ioe) and internet of nano things (iont). *2015 Internet Technologies and Applications (ITA)*, IEEE, p. 219–224, 2015.

4 EZECHINA, M.; OKWARA, K.; UGBOAJA, C. The internet of things (iot): a scalable approach to connecting everything. *The International Journal of Engineering and Science*, v. 4, n. 1, p. 09–12, 2015.

5 HUSSEIN, A. H. Internet of things (iot): Research challenges and future applications. *International Journal of Advanced Computer Science and Applications*, Science and Information (SAI) Organization Limited, v. 10, n. 6, 2019.

6 CHAOUCHI, H. *The internet of things: Connecting objects to the web*. [S.l.]: John Wiley & Sons, 2013.

7 SANTOS, B. P.; SILVA, L. A.; CELES, C. S.; NETO, J. B. B.; PERES, B. S.; VIEIRA, M. A. M.; VIEIRA, L. F. M.; GOUSSEVSKAIA, O. N.; LOUREIRO, A. A. Internet das coisas: da teoria à prática. 2016.

8 DEVALAL, A. K. S. Lora technology-an overview. In: IEEE. *2nd International conference on Electronics, Communication and Aerospace Technology (ICECA)*. [S.l.], 2018. p. 284–290.

9 BELTRAMELLI, L.; MAHMOOD, A.; ÖSTERBERG, P.; GIDLUND, M. Lora beyond aloha: An investigation of alternative random access protocols. *IEEE Transactions on Industrial Informatics*, IEEE, v. 17, n. 5, p. 3544–3554, 2020.

10 ALLIANCE, L. *What is LoRaWAN Specification*. 2022.

11 SEMTECH. An1200. 22, lora modulation basics. *Application Note*, Rev.2, 2015.

12 KNIGHT, M.; SEEBER, B. Decoding lora: Realizing a modern lpwan with sdr. In: *Proceedings of the GNU Radio Conference*. [S.l.: s.n.], 2016. v. 1, n. 1.

13 VOLAKIS, J. L. *Antenna engineering handbook*. [S.l.]: McGraw-Hill Education, 2007.

14 KRAUS, J. D. *Antennas*. [S.l.]: McGraw-Hill Inc., 1988.

15 ORFANIDIS, S. J. Electromagnetic waves and antennas. Rutgers University New Brunswick, NJ, 2002.

16 LEE, S.-W.; LO, Y. *Antenna Handbook: Fundamentals and mathematical techniques*. [S.l.]: Van Nostrand Reinhold, 1993.

17 BALANIS, C. A. *Antenna theory: analysis and design*. [S.l.]: John wiley & sons, 2005.

18 POZAR, D. M. Microstrip antennas. *Proceedings of the IEEE*, IEEE, v. 80, n. 1, p. 79–91, 1992.

19 CARVER, K.; MINK, J. Microstrip antenna technology. *IEEE transactions on antennas and propagation*, IEEE, v. 29, n. 1, p. 2–24, 1981.

20 NAYERI, P.; ELSHERBENI, A. Z.; YANG, F. Radiation analysis approaches for reflectarray antennas [antenna designer's notebook]. *IEEE Antennas and Propagation Magazine*, IEEE, v. 55, n. 1, p. 127–134, 2013.

21 LEE, S.; LO, Y. *Antenna Handbook: theory, applications, and design*. [S.l.]: Van Nostrand Reinhold, 1988.

22 POLENGA, S. V.; STANKOVSKY, A. V.; KRYLOV, R. M.; NEMSHON, A. D.; LITINSKAYA, Y. A.; SALOMATOV, Y. P. Millimeter-wave waveguide reflectarray. In: *2015 International Siberian Conference on Control and Communications (SIBCON)*. [S.l.: s.n.], 2015. p. 1–4.

23 HASANI, H.; PERRUISSEAU-CARRIER, J.; PEIXEIRO, C.; MOSIG, J. R. Dual-band dual-polarized reconfigurable unit-cell for reflectarray antenna in ku-band. In: *2013 7th European Conference on Antennas and Propagation (EuCAP)*. [S.l.: s.n.], 2013. p. 861–862.

24 RAMLI, M.; MISRAN, N.; MANSOR, M. F.; ISLAM, M. T. Analysis of reflectarray unit cell with capacitive effect. In: IEEE. *2014 2nd International Conference on Information and Communication Technology (ICoICT)*. [S.l.], 2014. p. 95–99.

25 HUM, S. V.; OKONIEWSKI, M.; DAVIES, R. J. Modeling and design of electronically tunable reflectarrays. *IEEE transactions on Antennas and Propagation*, IEEE, v. 55, n. 8, p. 2200–2210, 2007.

26 ZAWAWI, M. N. B.; LANTERI, J.; MIGLIACCIO, C.; PICHOT, C. 20 ghz active reflectarray using 1-bit phase shifter. In: IEEE. *2013 IEEE Antennas and Propagation Society International Symposium (APSURSI)*. [S.l.], 2013. p. 1668–1669.

27 YANG, H.; YANG, F.; XU, S.; MAO, Y.; LI, M.; CAO, X.; GAO, J. A 1-bit 10×10 reconfigurable reflectarray antenna: design, optimization, and experiment. *IEEE Transactions on Antennas and Propagation*, IEEE, v. 64, n. 6, p. 2246–2254, 2016.

28 HAN, J.; LI, L.; LIU, G.; WU, Z.; SHI, Y. A wideband 1 bit $12\times$ 12 reconfigurable beam-scanning reflectarray: Design, fabrication, and measurement. *IEEE Antennas and Wireless Propagation Letters*, IEEE, v. 18, n. 6, p. 1268–1272, 2019.

29 HUM, S. V.; OKONIEWSKI, M.; DAVIES, R. J. Modeling and design of electronically tunable reflectarrays. *IEEE transactions on Antennas and Propagation*, IEEE, v. 55, n. 8, p. 2200–2210, 2007.

30 LIU, T.; LI, M.; YANG, F.; XU, S. Phase error analysis for reflectarray antennas based on study of quasi-periodic effect. In: IEEE. *2017 11th European Conference on Antennas and Propagation (EUCAP)*. [S.l.], 2017. p. 3278–3281.

31 YOON, J. H.; YOON, Y. J.; KIM, H.; LEE, W.-s.; SO, J.-h. Reflection phase error analysis of microstrip reflectarrays. In: IEEE. *2015 International Workshop on Antenna Technology (iWAT)*. [S.l.], 2015. p. 126–129.

32 NOURINIA, J.; GHOBADI, C.; MOHAMMADI, B.; ALIZADEH, F. et al. Aperture efficiency study of square reflect array antennas. *Wireless Engineering and Technology*, Scientific Research Publishing, v. 9, n. 03, p. 66, 2018.

33 POZAR, D. M.; TARGONSKI, S. D.; SYRIGOS, H. Design of millimeter wave microstrip reflectarrays. *IEEE transactions on antennas and propagation*, IEEE, v. 45, n. 2, p. 287–296, 1997.

34 POZAR, D.; METZLER, T. Analysis of a reflectarray antenna using microstrip patches of variable size. *Electronics Letters*, IET, v. 29, n. 8, p. 657–658, 1993.

35 BALANIS, C. Antenna theory: a review. *Proceedings of the IEEE*, v. 80, n. 1, p. 7–23, 1992.

36 ZHANG, H.; CHEN, X.; WANG, Z.; GE, Y.; PU, J. A 1-bit electronically reconfigurable reflectarray antenna in x band. *IEEE Access*, IEEE, v. 7, p. 66567–66575, 2019.

37 COSTANZO, S.; VENNERI, F.; RAFFO, A.; MASSA, G. D. Dual-layer single-varactor driven reflectarray cell for broad-band beam-steering and frequency tunable applications. *IEEE Access*, IEEE, v. 6, p. 71793–71800, 2018.

38 GOU, Y.; FU, J.; FANG, X.; WU, Q. Two-dimensions beam scanning reflectarray antenna. In: IEEE. *2013 IEEE Antennas and Propagation Society International Symposium (APSURSI)*. [S.l.], 2013. p. 1674–1675.

39 BAYRAKTAR, O.; TOPALLI, K.; UNLU, M.; CIVI, O. A.; DEMIR, S.; AKIN, T. Beam switching reflectarray using rf mems technology. IET, 2007.

40 In: . [S.l.: s.n.].

41 ZHONG, Y.; LUYEN, H.; BEHDAD, N. A 1-bit, low-complexity, 20× 20-element electronically reconfigurable reflectarray antenna. In: IEEE. *2019 13th European Conference on Antennas and Propagation (EuCAP)*. [S.l.], 2019. p. 1–3.

42 HUANG, J. *Microstrip reflectarray antenna for the SCANSCAT radar application*. [S.l.], 1990.

43 MAO, Y.; XU, S.; YANG, F.; ELSHERBENI, A. Z. A novel phase synthesis approach for wideband reflectarray design. *IEEE transactions on antennas and propagation*, IEEE, v. 63, n. 9, p. 4189–4193, 2015.

44 AN, W.; XU, S.; YANG, F.; GAO, J. A ka-band reflectarray antenna integrated with solar cells. *IEEE Transactions on Antennas and Propagation*, IEEE, v. 62, n. 11, p. 5539–5546, 2014.

45 LIU, G.; KODNOEIH, M. R. D.; PHAM, K. T.; CRUZ, E. M.; GONZÁLEZ-OVEJERO, D.; SAULEAU, R. A millimeter-wave multibeam transparent transmitarray antenna at ka-band. *IEEE Antennas and Wireless Propagation Letters*, IEEE, v. 18, n. 4, p. 631–635, 2019.

46 PAN, Y.; ZHANG, Y. Analysis of blockage effects in a center-fed reflectarray. *Microwave and Optical Technology Letters*, Wiley Online Library, v. 55, n. 8, p. 1921–1926, 2013.

47 SILVER, S. *Microwave antenna theory and design*. [S.l.]: Iet, 1984.

48 BAHADORI, K.; RAHMAT-SAMII, Y. Estimation of blockage effects of complex structures on the performance of the spacecraft reflector antennas by a hybrid po/nf-ff method. *The Applied Computational Electromagnetics Society Journal (ACES)*, p. 31–38, 2007.

49 TURNER, R. P. *Diode Circuits Handbook*. [S.l.]: Foulsham, 1964.

50 SKYWORKS. Varactor diodes. *Application Note*, Rev. A, 2008.

51 PENFIELD, P.; RAFUSE, R. P. *Varactor applications*. [S.l.]: MIT Press (MA), 1962. v. 6.

52 WATERTOWN, M. The pin diode circuit designers' handbook. *Microsemi corporation, Santa-Ana: California*, 1992.

53 TANTWAI, K. K. Microwave-frequency non-linear universal model for pin diode. In: IEEE. *2007 International Workshop on Physics of Semiconductor Devices*. [S.l.], 2007. p. 119–122.

54 MACOM. Design with pin diodes. *Application Note*, Rev.V3.

55 YIGIT, M. E.; GUNEL, T. Pattern synthesis of linear antenna array via a new hybrid taguchi-genetic-particle swarm optimization algorithm. In: IEEE. *2018 18th Mediterranean Microwave Symposium (MMS)*. [S.l.], 2018. p. 17–21.

56 BOYD, S.; BOYD, S. P.; VANDENBERGHE, L. *Convex optimization*. [S.l.]: Cambridge university press, 2004.

57 FUCHS, B.; SKRIVERVIK, A.; MOSIG, J. R. Synthesis of uniform amplitude focused beam arrays. *IEEE Antennas and Wireless Propagation Letters*, IEEE, v. 11, p. 1178–1181, 2012.

58 FUCHS, B. Application of convex relaxation to array synthesis problems. *IEEE Transactions on Antennas and Propagation*, IEEE, v. 62, n. 2, p. 634–640, 2013.

59 POZAR, D. M. *Microwave engineering*. [S.l.]: John wiley & sons, 2011.

60 TSAI, F.-C.; BIALKOWSKI, M. E. Designing a 161-element ku-band microstrip reflectarray of variable size patches using an equivalent unit cell waveguide approach. *IEEE transactions on antennas and propagation*, IEEE, v. 51, n. 10, p. 2953–2962, 2003.

61 BHATTACHARYYA, A. K. *Phased array antennas: Floquet analysis, synthesis, BFNs and active array systems*. [S.l.]: John Wiley & Sons, 2006.

62 ANSYS, H. Workshop 9-1: Unit cell analysis (infinite array). *Accessed: Feb*, v. 24, p. 2018, 1970.

63 ANSYS, H. Workshop 9-1: Unit cell analysis (infinite array). *Accessed: 9th Oct 2022*, v. 2015.0, p. 1–44, 2015.

64 SADIKU, M. N. *Numerical techniques in electromagnetics*. [S.l.]: CRC press, 2000.

65 SILVESTRO, J. Hybrid finite element boundary integral method. *Ansys, Inc.[online]. Available: https://support. ansys. com*, 2010.

66 MORRIS, D. Which electromagnetic simulator should i use? *Agilent Technologies, Stockport*, 2012.

67 YUAN, X.; LYNCH, D. R.; STROHBEHN, J. W. Coupling of finite element and moment methods for electromagnetic scattering from inhomogeneous objects. *IEEE Transactions on Antennas and Propagation*, IEEE, v. 38, n. 3, p. 386–393, 1990.

68 IADC, I. Space debris mitigation guidelines. *Steering Group and Working Group*, v. 4, 2007.

69 HONG, J.-S. G.; LANCASTER, M. J. *Microstrip filters for RF/microwave applications*. [S.l.]: John Wiley & Sons, 2004.

70 SYRETT, B. A broad-band element for microstrip bias or tuning circuits (short papers). *IEEE Transactions on Microwave theory and techniques*, IEEE, v. 28, n. 8, p. 925–927, 1980.

71 SANTANA, M. P. *Reconfigurable Metasurface Antenna Array Using Holographic Beamforming*. 2021.

72 ANDRADE, G. F. D.; BARBOSA, E. V. S.; RONDINEAU, S. R. Rf front-end receiver for vehicular satellite communications and lna gaas fet design in ku-band. In: IEEE. *2020 Workshop on Communication Networks and Power Systems (WCNPS)*. [S.l.], 2020. p. 1–6.

73 WANG, P.-Y.; CHOU, M.-C.; SU, P.-C.; CHANG, Y.-C.; CHUANG, K.-H.; HSU, S. S. A fully integrated ku-band down-converter front-end for dbs receivers. In: IEEE. *2014 IEEE MTT-S International Microwave Symposium (IMS2014)*. [S.l.], 2014. p. 1–3.

74 CHENG, D.; LI, L.; XIE, M.; SHENG, B.; YOU, X. A ku-band receiver with 12-to-20-db gain,-14-dbm ipldb in 65-nm cmos technology. In: IEEE. *2018 Asia-Pacific Microwave Conference (APMC)*. [S.l.], 2018. p. 765–767.

75 BEHZAD, R. *RF microelectronics*. [S.l.]: Prentice hall, 2012.

76 ALLIANCE, L. *LoRaWAN Link Layer Specification*. 2020.

77 SMITH, J. R. *Modern communication circuits*. [S.l.]: McGraw-Hill, 1935.

78 SEMTECH. Sx1276/77/78/79 - 137 mhz to 1020 mhz low power long range transceiver. *Datasheet*, Rev.7, 2020.

79 SEMTECH. An1200.32, designing for high efficiency and low-harmonic emissions. *Application Note*, Rev.1, 2017.

80 MATTHAEI, G.; YOUNG, L.; JONES, E. *Design of Microwave Filters, Impedance-Matching Networks, and Coupling Structures. Volume 2*. [S.l.: s.n.], 1963.

81 CEL. *New Low Noise pHEMTs by CEL*. 2017.

82 SEMMTECH. Designing for high efficiency and low-harmonic emissions. *Application Note*, Rev.1.0, 2017.

83 STMICROELECTRONICS. An5457, rf matching network design guide for stm32wl series. *Application Note*, Rev.2, 2020.

84 SEMMTECH. An1200.40, application note: Reference design explanation. *Application Note*, Rev.1.1, 2018.

85 SKYWORKS. *Matching Differential Port Devices*. 2012.

86 TECHNOLOGIES, J. 0900bl15c050, sub-ghz balun, 800mhz - 1ghz, 1:1 impedance ratio, eia 0805. *Datasheet*, Rev.2.1, 2021.

APPENDIX

I FEED BLOCKAGE CALCULATION

```
SCAN.theta = 0:t_res:pi/2;
SCAN.phi = 0:p_res:2*pi;

[D.x, D.y, D.z] = sph2cart(phi_b,pi/2 - theta_b, r); % Detector coordinates;

% Extract the coordinates relative to the limits of the equivalent surface
% of the detector/fee of every corner odf the rectangle. Note that each
% column represents one corner of the rectangle. the rotation in z axis was
% not considered.

% W: feed antenna width;
% L: feed antenna lenght;
% theta_1: angle between -y and z related with detector position
% theta_2: angle between -x and z related with detector position
% phi_b: detector azimutal angle (only working for 90°)
% x: array elements coordinates in x
% y: array elements coordinates in y
% z: array elements coordinates in z
% r: detector height position in spherical coordinates, in FS

D.surf.z(1) = D.z + (W/2)*sin(theta_1) + (L/2)*sin(theta_2);
D.surf.z(2) = D.z - (W/2)*sin(theta_1) + (L/2)*sin(theta_2);
D.surf.z(3) = D.z - (W/2)*sin(theta_1) - (L/2)*sin(theta_2);
D.surf.z(4) = D.z + (W/2)*sin(theta_1) - (L/2)*sin(theta_2);

D.surf.y(1) = D.y - (W/2)*cos(theta_1)*sin(phi_b) - (L/2)*cos(theta_2)*cos(phi_b);
D.surf.y(4) = D.y - (W/2)*cos(theta_1)*sin(phi_b) + (L/2)*cos(theta_2)*cos(phi_b);
D.surf.y(2) = D.y + (W/2)*cos(theta_1)*sin(phi_b) - (L/2)*cos(theta_2)*cos(phi_b);
D.surf.y(3) = D.y + (W/2)*cos(theta_1)*sin(phi_b) + (L/2)*cos(theta_2)*cos(phi_b);

D.surf.x(1) = D.x + (L/2)*cos(theta_2)*sin(phi_b) - (W/2)*cos(theta_1)*cos(phi_b);
D.surf.x(2) = D.x + (L/2)*cos(theta_2)*sin(phi_b) + (W/2)*cos(theta_1)*cos(phi_b);
D.surf.x(3) = D.x - (L/2)*cos(theta_2)*sin(phi_b) + (W/2)*cos(theta_1)*cos(phi_b);
D.surf.x(4) = D.x - (L/2)*cos(theta_2)*sin(phi_b) - (W/2)*cos(theta_1)*cos(phi_b);

NFS.mask.x = ones(length(x),4); % Initializing mask variables
NFS.mask.y = zeros(length(y),4);
NFS.mask.z = NFS.mask.y;

% Calculates the translated vectors, for computing each NFS element mask.
for a = 1:4
    NFS.mask.x(:,a) = D.surf.x(a) - x;
    NFS.mask.y(:,a) = D.surf.y(a) - y;
    NFS.mask.z(:,a) = D.surf.z(a) - z;

    [NFS.mask.phi(:,a),NFS.mask.theta(:,a), NFS.mask.r(:,a)] = cart2sph(NFS.mask.x↙
(:,a), ...
         NFS.mask.y(:,a),NFS.mask.z(:,a));

end
NFS.mask.theta = pi/2 - NFS.mask.theta; % Corrects to matlab coordinate system.

% converts negative angles to positive
  for rs = 1: length(x)
      for s = 1:4
          if (NFS.mask.phi(rs,s) < 0)
                NFS.mask.phi(rs,s) = NFS.mask.phi(rs,s) + 2*pi;
          end
      end
  end
```

```
theta_c = asin((W/(cos(atan((L/2)/W))))/r);
k.x = zeros(length(SCAN.theta),length(SCAN.phi));
k.y = k.x;
N = length(x);
zera = zeros(1,N);

% Initializing array factor variables
AF_shadowed.lin = zeros(length(SCAN.phi),length(SCAN.theta));

for t = 1:length(SCAN.theta)
    for p = 1:length(SCAN.phi)
        k.x(p,t) = sin(SCAN.theta(t)).*cos(SCAN.phi(p));
        k.y(p,t) = sin(SCAN.theta(t)).*sin(SCAN.phi(p));
        for m = 1:N
             if max(NFS.mask.theta(m,:)) < theta_c
                 temp_var3 = 0;
                 phi_max = 2*pi;
                 phi_min = 0;
             else
                 temp_var3 = min(NFS.mask.theta(m,:));
                 phi_min = min(NFS.mask.phi(m,:));
                 phi_max = max(NFS.mask.phi(m,:));
             end
              if (max(NFS.mask.phi(m,:)) > 3*pi/2) && (min(NFS.mask.phi(m,:)) <
pi/2)
                  temp_var1 = find(NFS.mask.phi > 3*pi/2);
                  temp_var2 = find(NFS.mask.phi < pi/2);

                  temp_var1 = min(NFS.mask.phi(temp_var1));
                  temp_var2 = max(NFS.mask.phi(temp_var2));
                  if max(NFS.mask.theta(m,:)) < theta_c
                    temp_var1 = 0;
                    temp_var2 = 2*pi;
                  end
                  if (SCAN.theta(t) <= max(NFS.mask.theta(m,:)))&&(SCAN.theta(t)
>= temp_var3)&& ...
                      (SCAN.phi(p) <= temp_var2||(SCAN.phi(p) >= temp_var1))
                      zera(m)= 0;
                  else
                     zera(m) = 1;
                  end
               else
                  if (SCAN.theta(t) <= max(NFS.mask.theta(m,:)))&&(SCAN.theta(t) >=
temp_var3)&& ...
                     (SCAN.phi(p) <= phi_max)&&(SCAN.phi(p) >= phi_min)
                     zera(m)= 0;
                  else
                     zera(m) = 1;
                  end
             end
                AF_shadowed.lin(p,t) = AF_shadowed.lin(p,t) + zera(m).*excitation
(m).*exp(1i*2*pi*(k.x(p,t)*x(m) + k.y(p,t)*y(m)));
                AF.lin(p,t) = AF.lin(p,t) + 1*exp(1i*2*pi*(k.x(p,t)*x(m) + k.y(p,
t)*y(m)));
        end
    end
end
```

II CONVEX OPTIMIZATION ALGORITHM

```
%% 1. Fixed Constants:
N = 10;
lambda0 = 0.0251; % @ 11.95GHz
theta_feed = 0; % feed position
phi_feed = 0; % feed position
theta_b = 30; % beam direction elevation (degrees)
phi_b = 0; % beam direction azimuth (degrees)
theta_b = deg2rad(theta_b); % beam direction (rad)
phi_b = deg2rad(phi_b); % Beam azimuth direction

t_res = (pi/2)/89; %Resolution of the plots (theta)
p_res = (2*pi)/359; %Resolution of the plots (phi)
r = 4.7790; % Normalized Height position of the feed antenna;
d = 0.6; % normalized distance between elements

%% 2. Array Elements positions (normalized with lambda0)
x = reshape(meshgrid(-(d/2)*(N-1):d:+(d/2)*(N-1)),1,N^2);
y = reshape(meshgrid(-(d/2)*(N-1):d:+(d/2)*(N-1))',1,N^2);
z = zeros(1,N^2);
% plot(x_n,y_n,'x'); % uncomment to plot the array shape

%% 3. Feed position (spherical coordinates)
Feed.position.theta = deg2rad(theta_feed); % Elevation angle of the feed antenna
in global coordinates
Feed.position.phi = deg2rad(phi_feed); % position of the feed antenna in global
coordinates
Feed.position.r = r;

% OBS: locCS refers to the local system of coordinates of each unit cell
% The following code is to define the Feed positions in terms of each cell

[Feed.position.x, Feed.position.y, Feed.position.z] = sph2cart(Feed.position.phi,
pi/2-Feed.position.theta,Feed.position.r);
Feed.vect_locCS = [Feed.position.x - x;  Feed.position.y - y; Feed.position.z -
z];
[phi_feed_locCS, theta_feed_locCS, r_feed_locCS] = cart2sph(Feed.vect_locCS(1,:),
Feed.vect_locCS(2,:), Feed.vect_locCS(3,:));  % 3 x (1 x N)
theta_feed_locCS = pi/2 - theta_feed_locCS;

%% 4. System Coordinate transformation (global CS to feed´s CS)

%The following code refers to a matrix transformation, which i am not sure
%how it works. But just copied from Lens code.

[TEMP.phi,TEMP.theta,TEMP.r] = cart2sph(Feed.position.y, Feed.position.z,Feed.
position.x);  % 1 x 3
TEMP.theta = pi/2 - TEMP.theta;
Feed.base.locCS(:,3) = -[Feed.position.x; Feed.position.y; Feed.position.z]/norm
([Feed.position.x; Feed.position.y; Feed.position.z],2);  % 1 x 3
Feed.base.locCS(:,1) = [sin(TEMP.theta); -cos(TEMP.theta).*cos(TEMP.phi); -cos
(TEMP.theta).*sin(TEMP.phi)];
Feed.base.locCS(:,2) = cross(Feed.base.locCS(:,3),Feed.base.locCS(:,1));

%% 5. Unit Cell (Array) E-Fields analytic calculation

% Parameters of the unit cell patch antennas
UC.patch.lambda0 = lambda0;
UC.patch.L = 0.4382*lambda0;
UC.patch.W = 0.4382*lambda0;

```

```
 54 % Calculates each unit cell field pointed towards the feed. (In Local UC
coordinates).
 55 Array.Efield_t = an_patch(UC.patch,theta_feed_locCS,phi_feed_locCS);
 56 Array.Efield = [Array.Efield_t.x; Array.Efield_t.y; Array.Efield_t.z];  % 3 x N
 57
 58 %% 6. Feed E-Fields analytic calculation
 59
 60 % The following code computes all FS lens element position vectors to the Feed in
feed
 61 % coordinate system in order to calculate the field contribution of the
 62 % feed to each element in the array
 63 Array.vect_feedCS = (Feed.base.locCS.')*Feed.vect_locCS;
 64 [phi_Array_feedCS,theta_Array_feedCS,r_Array_feedCS] = cart2sph(Array.vect_feedCS
(1,:),Array.vect_feedCS(2,:),Array.vect_feedCS(3,:));  % 3 x (1 x N)
 65 theta_Array_feedCS = pi/2 - theta_Array_feedCS;
 66
 67
 68 % Feed pattern modeling
 69 Feed.patch.lambda0 = lambda0;
 70 Feed.patch.L = 0.4382*lambda0;
 71 Feed.patch.W = 0.4382*lambda0;
 72
 73 Feed.feedCS.Efield_t = an_patch(Feed.patch,theta_Array_feedCS,phi_Array_feedCS);
 74 Feed.feedCS.Efield = [Feed.feedCS.Efield_t.x; Feed.feedCS.Efield_t.y; Feed.feedCS.
Efield_t.z];   % 3 x N
 75 Feed.Efield = Feed.base.locCS*Feed.feedCS.Efield;        % 3 x N
 76
 77 %% 7. Calculate the resulting field
 78
 79 % 7.1. Field recieved at each unit cell element from the feeding antenna
 80 FreeSpaceLoss = (r_Array_feedCS/(4*pi));
 81 Excit = dot(Feed.Efield,Array.Efield,1)./FreeSpaceLoss;
 82
 83 % 7.2. Calculate the geometric phase distribution/compensation
 84 ReqPhase = 2*pi*(r_Array_feedCS - (x*cos(phi_b) + y*sin(phi_b))*sin(theta_b));
 85
 86 %% 8.1 Calculate/plot the Initial Array Factor (Continuous and Discrete)
 87
 88  x3d = reshape(x,[sqrt(length(x)),sqrt(length(x))]);
 89  y3d = reshape(y,[sqrt(length(x)),sqrt(length(x))]);
 90
 91  [theta_grid,phi_grid] = meshgrid(-pi/2:t_res:pi/2, 0:p_res:2*pi);
 92
 93  sinU = sin(theta_grid).*cos(phi_grid); % U-sine space.
 94  sinV = sin(theta_grid).*sin(phi_grid); % V-sine space.
 95
 96  Ux = reshape(kron(x3d(:),sinU)',length(0:t_res:pi),length(0:p_res:2*pi),length
(x3d(:))); % Calcula X*sinU e dá reshape em um array 3d.
 97  Vy = reshape(kron(y3d(:),sinV)',length(0:t_res:pi),length(0:p_res:2*pi),length
(y3d(:))); % Calcula Y*sinV e dá reshape em um array 3d.
 98
 99  ReqPhaseBin = ReqPhase;
100  aux_index = find(ReqPhase > 2*pi);
101  aux(aux_index)= floor(ReqPhase(aux_index)/(2*pi));
102  ReqPhaseBin(aux_index) = ReqPhase(aux_index) - (aux(aux_index)*2*pi); %
Transformar angulos maiores que 360 no seu correspondente.
103  ReqPhaseBin(find(ReqPhaseBin < pi))= 0;
104  ReqPhaseBin(find(ReqPhaseBin > pi))= pi;
105
106  Excit0(1,1,:) = Excit.*exp(1i*(ReqPhase - 2*pi*r_feed_locCS)); % Array Contínuo
```

```
107  Excit1(1,1,:) = Excit.*exp(1i*(ReqPhaseBin - 2*pi*r_feed_locCS)); % Array Binário
108
109  AF = sum(Excit0.*exp(1i*2*pi*(Ux+Vy)),3)';
110  AF_abs = abs(AF);
111  AF_norm = AF_abs/max(max(abs(AF)));
112  AF_norm_db = 20*log10(AF_norm);
113  seb_plot3(rad2deg(theta_grid),phi_grid,AF_norm_db,'Diagrama de Radiação ideal')
114
115  AF_d = sum(Excit1.*exp(1i*2*pi*(Ux+Vy)),3)';
116  AF_d_abs = abs(AF_d);
117  AF_d_norm = AF_d_abs/max(max(abs(AF_d)));
118  AF_d_norm_db = 20*log10(AF_d_norm);
119  seb_plot3(rad2deg(theta_grid),phi_grid,AF_d_norm_db,'Diagrama de Radiação↙
Discreto')
120
121  figure(2);
122  plot(linspace(-90,90,180-1), AF_norm_db(1,:),'LineWidth',↙
1.0,'Color','blue','DisplayName','Diagrama de Radiação ideal');
123  hold on
124  plot(linspace(-90,90,180-1), AF_d_norm_db(1,:),'LineWidth',↙
1.0,'Color','black','DisplayName','Diagrama de Radiação prático \n (Before opt)');
125  axis([-90 90 -40 0])
126  legend;
127
128 %% 8.2. Find the secondary lobes region for plotting only
129
130  gamma_t = 11; % theta scan for the primary lobe region
131  gamma_p = 20; % theta scan for the secondary lobe region
132
133 %% 9. Find the secondary region for the optimization/coarse region
134
135 t_res_opt = (pi/2)/25;
136 p_res_opt = (pi/2)/25;
137
138 theta_0 = -pi/2:t_res_opt:pi/2;
139 phi_0 = 0:p_res_opt:2*pi;
140
141 [theta_grid_0,phi_grid_0] = meshgrid(theta_0,phi_0);
142
143 theta_grid_0 = reshape(theta_grid_0',1,size(theta_grid_0,2)*size(theta_grid_0,1));
144 phi_grid_0 = reshape(phi_grid_0',1,size(phi_grid_0,2)*size(phi_grid_0,1));
145
146 sinU_0 = sin(theta_grid_0).*cos(phi_grid_0);
147 sinV_0 = sin(theta_grid_0).*sin(phi_grid_0);
148
149 U_0= x'*sinU_0;
150 V_0 = y'*sinV_0;
151
152 w_0 = Excit.*exp(1i*(ReqPhase - 2*pi*r_feed_locCS));
153 AF_0 = w_0*exp((1i*2*pi).*(U_0+V_0));
154
155 region_1 = find(theta_grid_0 > (-theta_b - deg2rad(gamma_t)) & ...
156              theta_grid_0 < (-theta_b + deg2rad(gamma_t)) & ...
157              phi_grid_0 > (pi-deg2rad(gamma_p)) & ...
158              phi_grid_0 < (pi+deg2rad(gamma_p)));
159
160 region_2 = find(theta_grid_0 > (theta_b - deg2rad(gamma_t)) & ...
161             theta_grid_0 < (theta_b + deg2rad(gamma_t)) & ...
162             phi_grid_0 > -deg2rad(gamma_p) & ...
163             phi_grid_0 < deg2rad(gamma_p));
```

```
z0 = 50;    % Line characteristic impedance
fs = 2;     % Normalized band pass frequency
lar = 0.1;  % Desired ripple
las = 30;   % Rejection band attenuation
f0 = 11.95e+9; % Center frequency
f1 = 11.7e+9;  % Lower band pass frequency
f2 = 12.2e+9;  % High band pass frequency
omega0 = 2*pi*f0;

FBW = (f2 - f1)/f0 % Fractional bandwith
y0 = 1/z0;  % Characteristic admittance
%%%%%%%% Calculating the order (butterworth) %%%%%%%%%%
n_butter = log10((10^(0.1*las))-1)/(2*log10(fs));
%%%%%%%% Calculating the order (Chebyshev) %%%%%%%%%
n_cheby = acosh(sqrt((10^(0.1*las)-1)/(10^(0.1*lar)-1)))/(acosh(fs));

%Butterworth coefficients
n_butter = round(n_butter)+1;
g_butter(n_butter + 2) = 0;
g_butter(1) = 1;
g_butter(n_butter + 2) = 1;

for(i = 1:1:(n_butter))
    g_butter(i+1) = 2*sin(((2*i-1)*pi)/(2*(n_butter)));
end

%Chebychev coefficients

n_cheby = round(n_cheby)+1;

ak(n_cheby) = 0;
bk(n_cheby) = 0;

g_cheby(n_cheby +2) = 0;
g_cheby(1) = 1;
beta = log(coth(lar/17.37));
gama = sinh(beta/(2*n_cheby));

g_cheby(2) = (2/gama)*sin(pi/(2*n_cheby));
for(i = 2:1:(n_cheby + 1))

    g_cheby(i+1) =(1/g_cheby(i))*((4*sin(((2*i-1)*pi)/(2*n_cheby))*sin(((2*i-3)*pi)↙
/(2*n_cheby)))/(gama^2 + (sin(((i-1)*pi)/n_cheby))^2));

end

if(mod(n_cheby,2) == 0)
    g_cheby(n_cheby+2) = coth(beta/4)^2;
else
    g_cheby(n_cheby+2) = 1;
end

%This is only applicable to the parallel coupled topology.
J_inv(n_butter+1) = 0;
J_inv(1) = sqrt((pi/2)*FBW/(g_cheby(1)*g_cheby(2)));
for(i = 2:1:(n_cheby))
    J_inv(i) = pi*FBW/(2*sqrt(g_cheby(i)*g_cheby(i+1)));
end
J_inv(n_butter+1) = sqrt((pi/2)*FBW/(g_cheby(n_butter+1)*g_cheby(n_butter+2)));

```

```
60 Z_odd(n_butter +1) = 0;
61 Z_even(n_butter +1) = 0;
62 for(i = 1:1:(n_butter+1))
63     Z_even(i) = (1/y0)*(1 + J_inv(i)+(J_inv(i)^2));
64     Z_odd(i) = (1/y0)*(1 - J_inv(i)+(J_inv(i)^2));
65 end
```

IV CONTROLLER BOARD SCHEMATICS

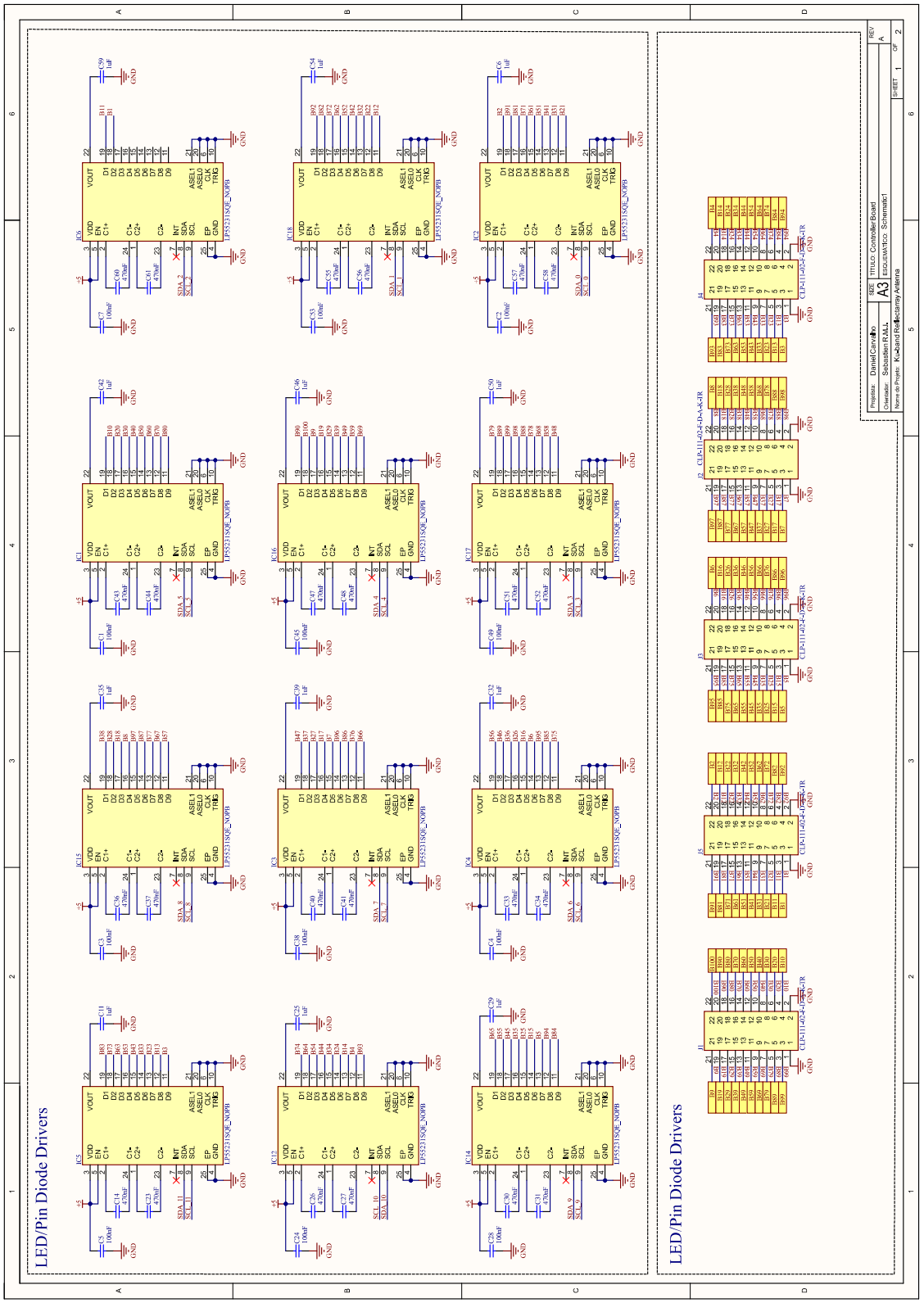

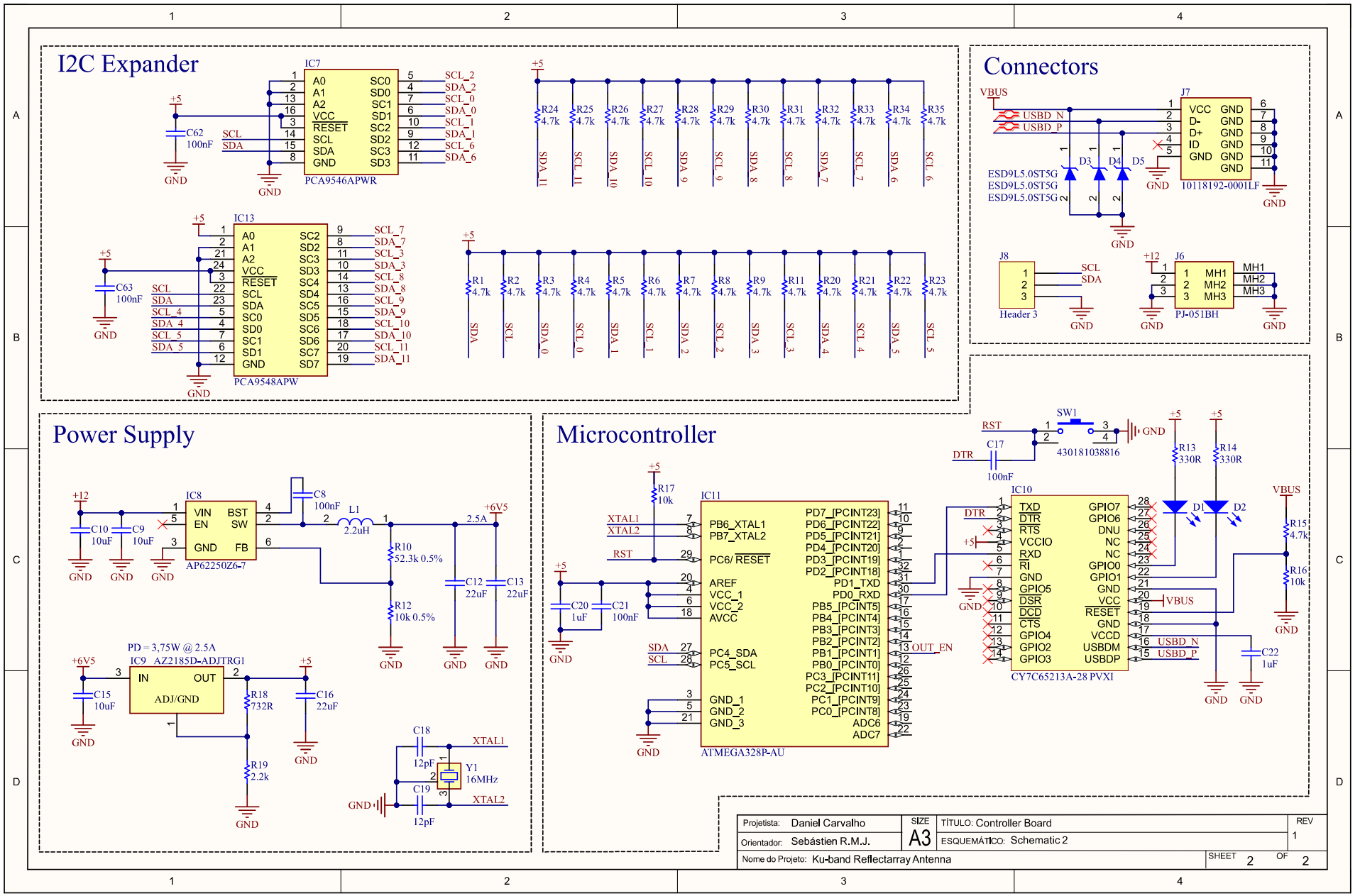
I2C Expander
IC7
PCA9546APWR
IC13
PCA9548APW
Connectors
J7
10118192-0001LF
J8
Header 3
J6
PJ-051BH
Power Supply
IC8
AP62250Z6-7
PD = 3,75W @ 2.5A
IC9 AZ2185D-ADJTRG1
Microcontroller
IC11
ATMEGA328P-AU
IC10
CY7C65213A-28 PVXI
SW1
430181038816
Projetista: Daniel Carvalho
Orientador: Sebástien R.M.J.
Nome do Projeto: Ku-band Reflectarray Antenna
SIZE A3
TÍTULO: Controller Board
ESQUEMÁTICO: Schematic 2
REV 1
SHEET 2 OF 2

V LNA SCHEMATIC

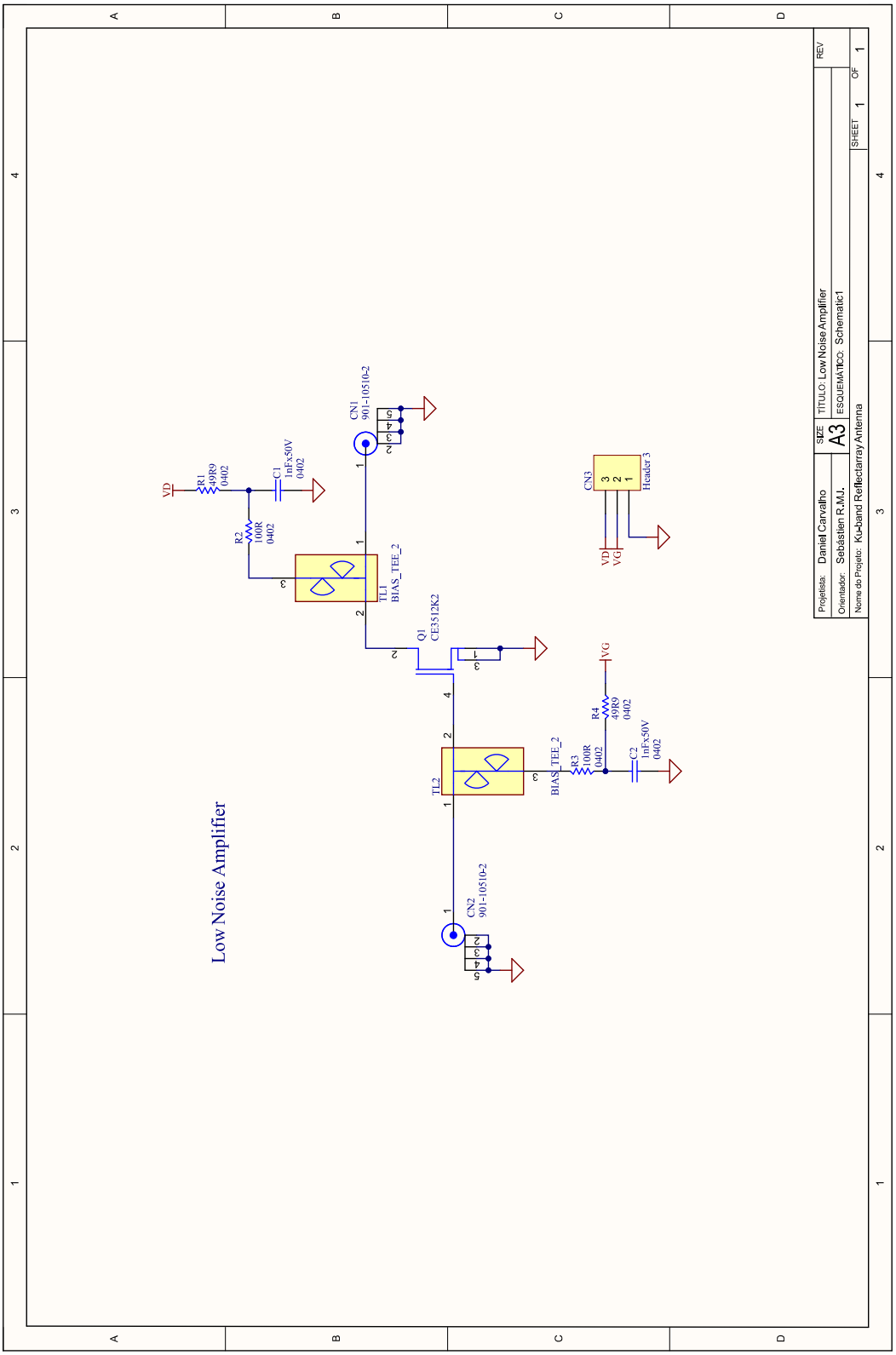

VI LAYOUT PRINTS

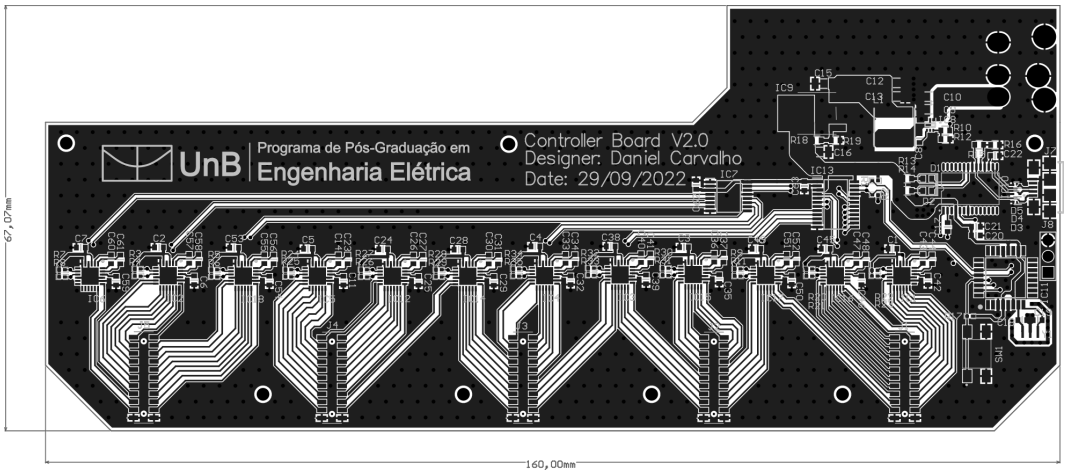

Figure VII.1: Top Layer of the Controller Board.

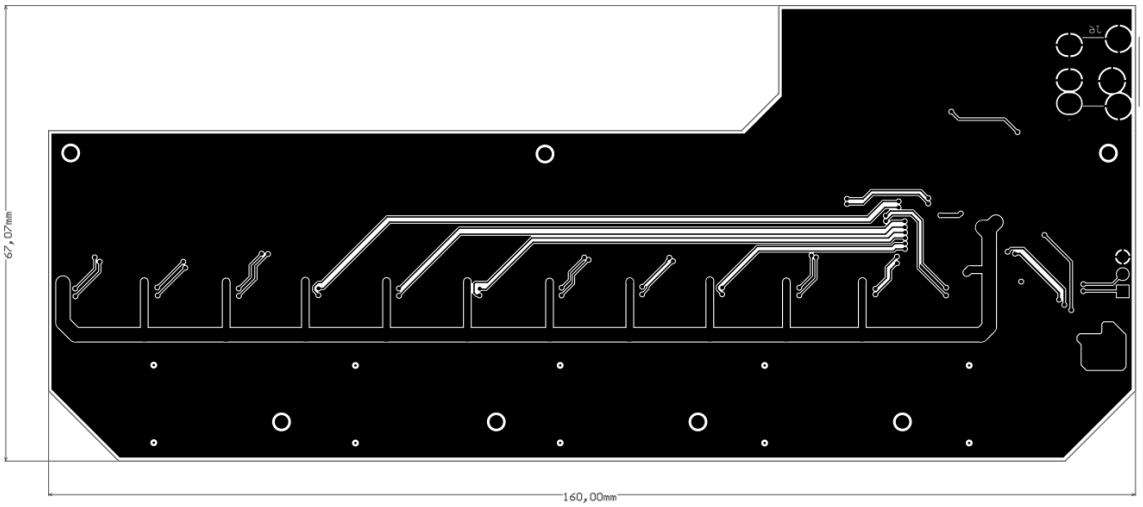

Figure VII.2: Bottom Layer of the Controller Board.

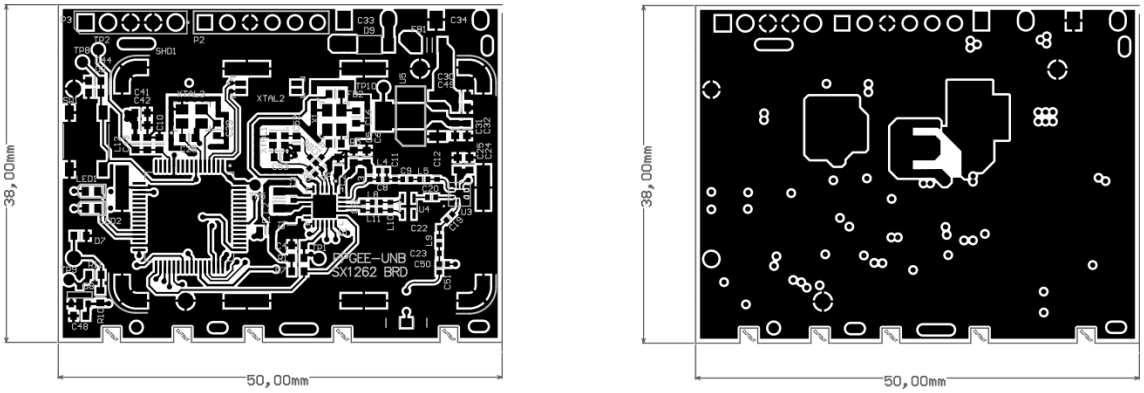

Figure VII.3: Top Layer and Layer 1 of the SX1262 Board

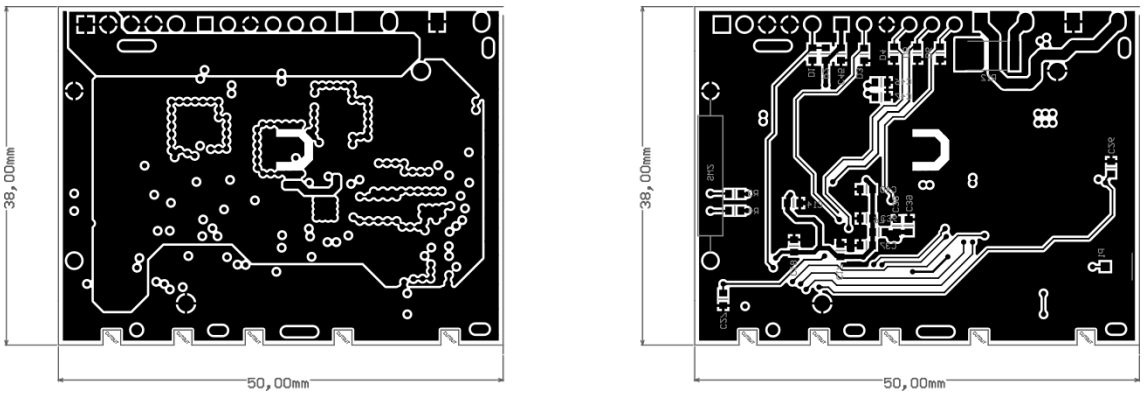

Figure VII.4: Layer 2 and Bottom layers of the SX1262 Board.

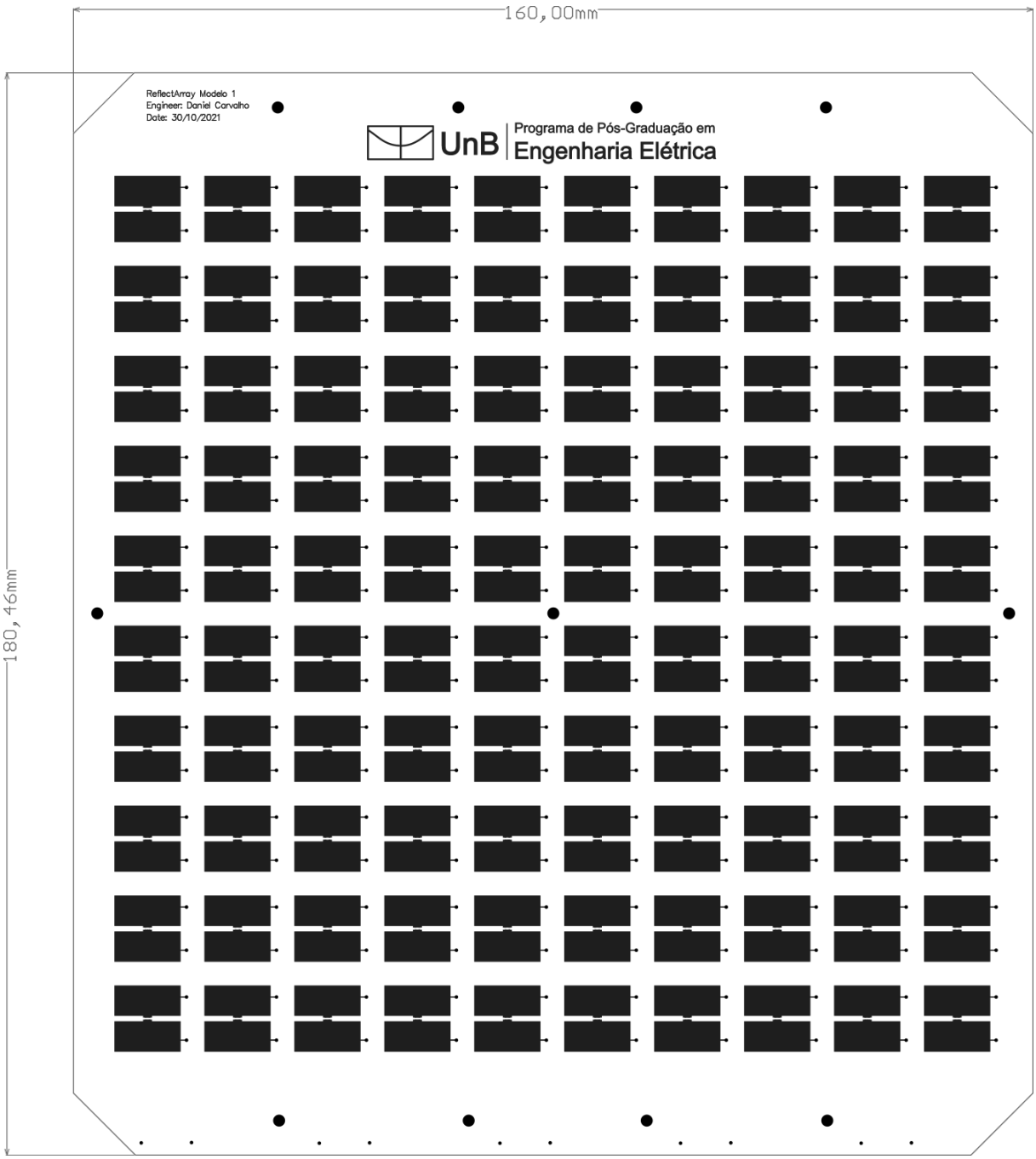

Figure VII.5: Top Layer of the Reflectarray Board.

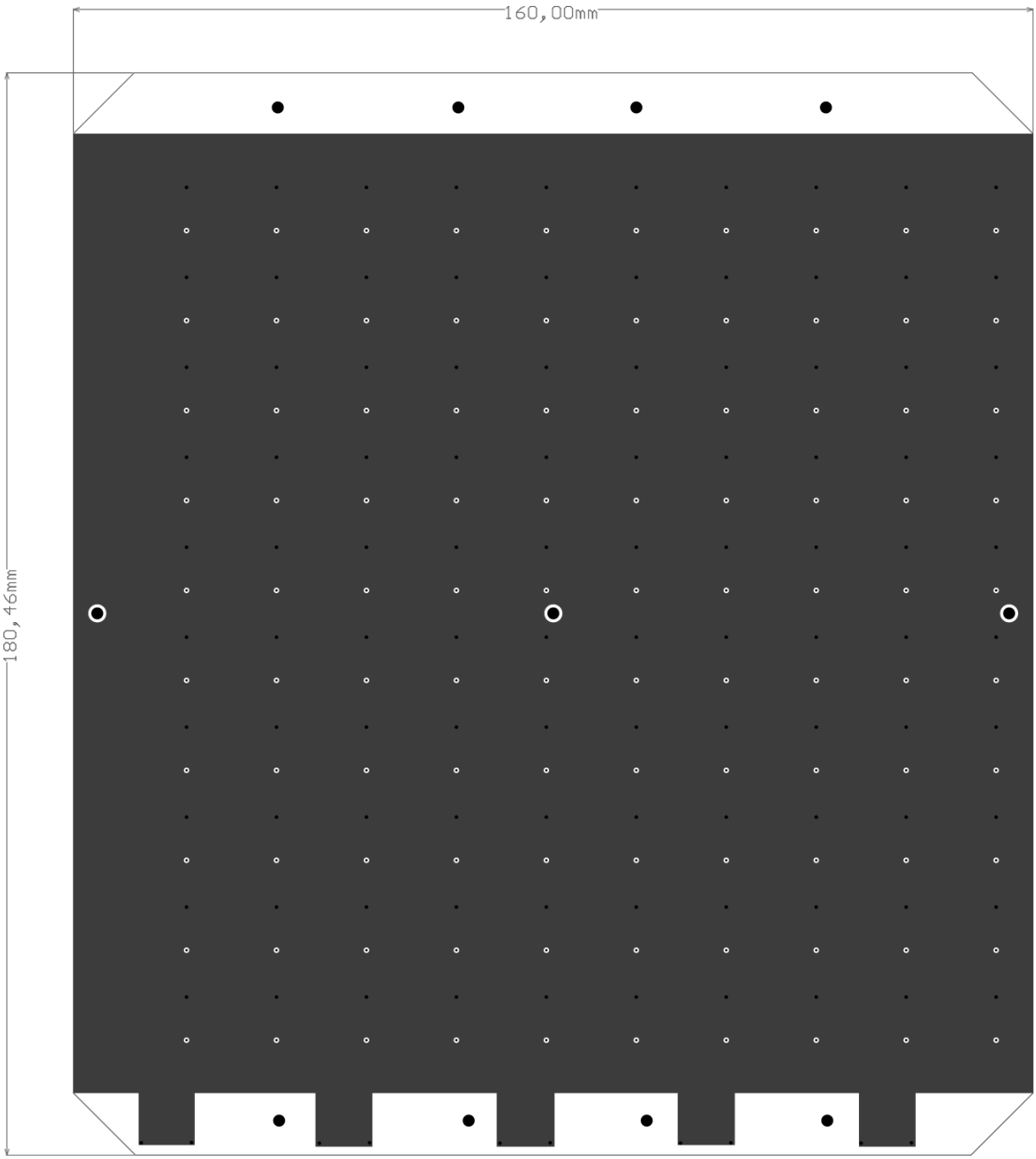

Figure VII.6: Mid-layer of the Reflectarray Board.

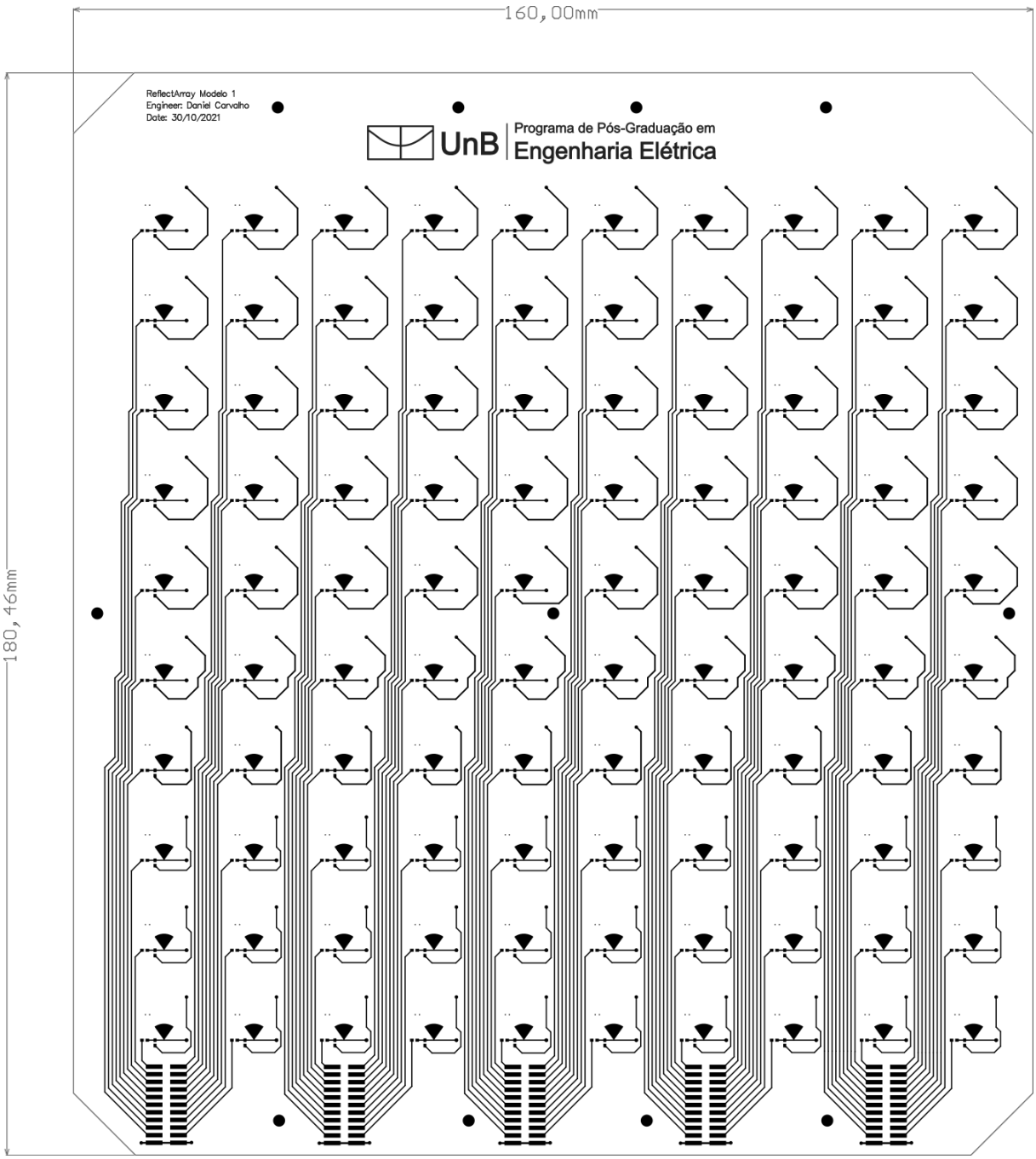

Figure VII.7: Bottom Layer of the Reflectarray Board.